Dynamics of stratified regions in Saturn

Joshua Robert Kirk

Submitted in accordance with the requirements for
the degree of
Doctor of Philosophy

University of Leeds
School of Mathematics
August 2018

The candidate confirms that the work submitted is his own, except where work has formed part of jointly authored publications has been included. The contribution of the candidate and the other authors to this work has been explicitly indicated below. The candidate confirms that appropriate credit has been given within the thesis where reference has been made to the work of others.

This copy has been supplied on the understanding that it is copyright material and that no quotation from the thesis may be published without proper acknowledgement.

©2018 The University of Leeds and Joshua Robert Kirk

The right of Joshua Robert Kirk to be identified as Author of this work has been associated by him in accordance with the Copyright, Designs and Patents Act 1988.

Abstract

Saturn has a rather peculiar magnetic field in that it is highly spin axisymmetric. Evidence for the decay time of a magnetic field on the scale of Saturn would suggest that a dynamo operates deep within its interior. As a consequence, the observed field would be in violation of Cowling's theorem. It is believed that a stably stratified layer under the influence of a thermal shear is the reason for the observed axisymmetric field. This stable layer is believed to be formed from helium sedimentation deep within Saturn, with the thermal shear driven by pole-equator temperature differences. The combined effects of shearing and the stable layer attenuate the non-axisymmetric field components leaving only the axisymmetric field at the surface.

Motivated by the influence of this stable stratification, we follow on from initial work by Stevenson (1982b) by first considering the linear problem with variable conductivity and looking at the consequences of increasing the parameter that controls the strength of the thermal wind as mentioned in his paper.

In subsequent chapters the analysis concentrates on the nonlinear contributions by including the momentum equation into our calculations. We present asymptotic analysis of such a system and show that the geostrophic flow, found by satisfying Taylor's constraint, is singular for an inviscid interior solution in the limit of small Rm, where Rm, the magnetic Reynolds number, controls the strength of the shearing effect within the layer.

Numerical treatment of the system of equations for a viscous system are also considered. The results of exploring the parameter space for Rm and Ha, the Hartmann number, lead to further asymptotic analysis in which viscosity is considered. A boundary layer solution is found, which is validated by the numerical solution.

The latter part of the thesis looks at the numerical solution with the inclusion of a horizontal field, the motivation for which will become apparent in the analysis of the inviscid regime.

To Alice.

Acknowledgements

I would like to thank my supervisors David and Chris for their insight and extensive knowledge of the subject field and for allowing me the opportunity to study for a PhD under their guidance. The comments and corrections provided during the past several months have made this thesis a reality.

I am grateful for my good friends, Gary, Paul and Kyle who have always been a source of regular support and laughter throughout my time during school, undergraduate and postgraduate life. My group of friends would not be complete without Neil and Joe, thank you for the European adventures — long may they continue.

I would also like to thank my family, especially my parents, for supporting and encouraging me throughout my life. I also wish to take this opportunity to mention my sister and my brother-in-law, Laura-Jane and David, and my brother Alfie, I love them all dearly.

During my time at Leeds LUUKBKM has become a big factor in my life; it helped me stay focused on the PhD and allowed me to develop as a person. So thank you to all those I have met, those who have come and gone, and to those that I have become friends with.

The department in which I have been a part of for the past four years has seen many faces come and go. I feel a special mention must go to Stephen, Joe, Steven, Mouloud and Wieland who have made it that extra bit memorable.

Finally, it goes without saying, the most important person throughout my PhD has been Alice. I cannot thank you enough for listening to me every day, for all my concerns, worries and lengthy discussions about the PhD; I could not have gone beyond day one without you.

This research has been funded by a studentship from STFC.

Contents

List of Figures

Chapter 1

Introduction

1.1 Motivation and background

Magnetic fields are ubiquitous throughout the universe and exist on a wide range of scales, from the macroscale, such as a fridge magnet, to the galactic scale, such as the magnetic field of the Milky Way. Our work focuses on the dynamics of planetary magnetic fields.

The existence of Earth's magnetic field has been known for some time; the invention of the compass has been a valuable tool for many explorers over the years and the historical evolution of the geomagnetic field can be observed from chemical isotopes in rocks and ice cores. However, only in recent history has our discovery of magnetic fields in other astrophysical objects come to fruition. In 1908 the magnetic field of the Sun was discovered by Hale (1908) and later the magnetic field of the outer planets were reported by Burke & Franklin (1955). The understanding of how such fields work is a complex process and a very active part of research to this day.

One of the main topics of interest is the self-excitement of magnetic fields due to complex motions of electrically conducting fluids within stars and planets. This is known as the dynamo process (Moffatt, 1978). The dynamo process stems from earlier discussion on how the Sun could have became a magnet (Larmor, 1919) and its theory is still relatively young compared to other topics in mathematics. In its infancy (during the 20th century), analytical focus on the dynamo problem revealed difficulties in sustaining the magnetic field from simple fluid motions; as a consequence several anti-dynamo theorems were derived (see Cowling 1933, Zeldovich 1957 and Childress 1969). The invention of the computer has allowed numerical treatment of the equations that describe the dynamo, thereby finding solutions where analytical techniques would become intractable. As processing power has increased with time, so has the complexity of the dynamics considered, with numerical solutions to the self-consistent geodynamo in a convecting spherical shell first calculated by Zhang & Busse (1988) (and see also Zhang & Busse (1989)). Since then the latest computer codes have the ability to simulate many physical aspects of astrophysical objects in order to study the dynamo that operates. Although these simulations are still not at the correct physical parameter regimes (Jones, 2003) they do provide deep insight into the dynamics of the problem.

1.2 Saturn's magnetic field

This thesis is motivated by observations of Saturn's magnetic field. Along with Mercury, it is unique compared to other observed planetary magnetic fields as it is almost perfectly axisymmetric (Stevenson, 2003). In figure 1.1 the radial surface field of Saturn is plotted to highlight this axisymmetry. The magnetic field of Saturn was not detected until the Pioneer 11 flyby owing to its weak radio emissions and its distance from Earth (Connerney, 1993), whilst the subsequent Voyager 1 and Voyager 2 flybys provided a more detailed mapping of the magnetic field.

An estimate of the decay time (τ) for Saturn's magnetic field, if primordial, can be calculated as $\tau \sim L^2\lambda^{-1}$ where $L = 5.83 \times 10^7$m is the radius of Saturn and $\lambda \sim 2\text{m}^2\text{s}^{-1}$ is the magnetic diffusivity estimate within Saturn (from laboratory experiments). This gives an approximate decay time of 22 million years. It is understood that the magnetic fields of the planets formed at the same time as the solar system, which would put the age of a primordial field at 4.5 billion years. This mismatch in time scales strongly suggests that a dynamo operates within Saturn in order for there to be a magnetic field.

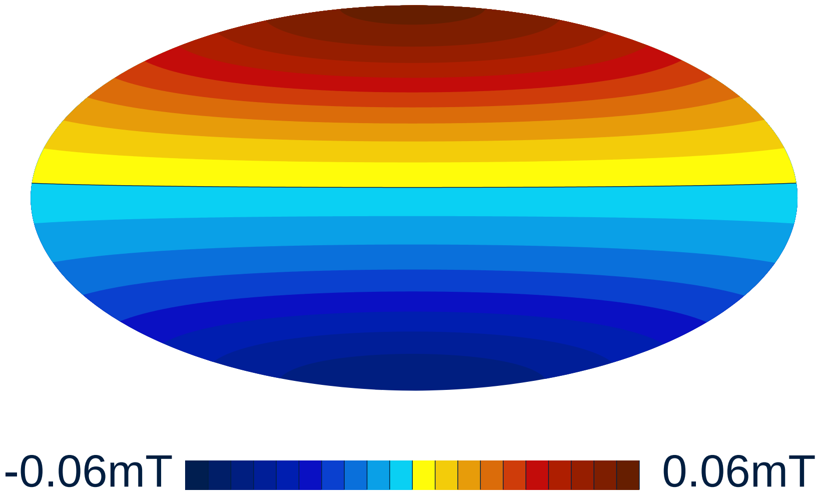

Figure 1.1: Surface field of Saturn reconstructed from its Gauss coefficients, kindly reproduced from Jones (2011).

The observational evidence does not bode well for a dynamo operating in Saturn as this violates Cowling's theorem (Cowling, 1933), which states that axisymmetric fields cannot be maintained by dynamo action. This therefore suggests that the field generated deep inside is inherently different to that observed at the surface.

Stevenson (1980) put forward the idea that this axisymmetry is due to the presence of a stably stratified layer. He suggested that flows in this layer might reduce the non-axisymmetric components of the magnetic field in and above this region. The dynamo could then be generating a non-axisymmetric field in the deep interior, this being consistent with Cowling's theorem, but we are observing at the surface where the non-axisymmetric components have been eliminated. There is a variety of evidence that supports this theory, which shall be discussed, as well as evidence for a dynamo source.

1.3 Evidence of a stratified layer

1.3.1 Solar abundances and depletion of helium

It is reasonable to assume that the gas giants have chemical abundances similar to that of the protosolar nebula abundance at the time of planetary formation (Guillot, 1999), which would put the helium mass mixing ratio at 0.280 ± 0.005. Whilst for Saturn this ratio has been calculated as 0.226 ± 0.03 (Ben-Jaffel & Abbes, 2015) near the surface, no *in situ* measurements have yet been made, which may lead to possible inaccuracies with the result. This discrepancy in ratios would suggest that the helium in the upper layers of Saturn's atmosphere has sunk to the greater depths via some mechanism, thereby resulting in a helium rich deep interior and a helium depleted envelope.

The internal structure of Saturn suggested by Stevenson (1980) (schematic provided in figure 1.2) is motivated by this apparent depletion of helium in the upper atmosphere. One possibility for the lack of helium is that the helium has slowly "rained" down to the lower atmosphere owing to gravitational differentiation. This differentiation is due to helium becoming immiscible in molecular hydrogen at high pressure. During this process a stratified layer forms between the upper atmosphere (He depleted) and lower atmosphere (He rich). The concept of gravitational differentiation would also explain the excess luminosity observed (see §1.3.2). The size of the layer from figure 1.2 would be approximately 2900 km. The thickness of the layer is very thin compared to the radius of Saturn ($\sim 58,000$km).

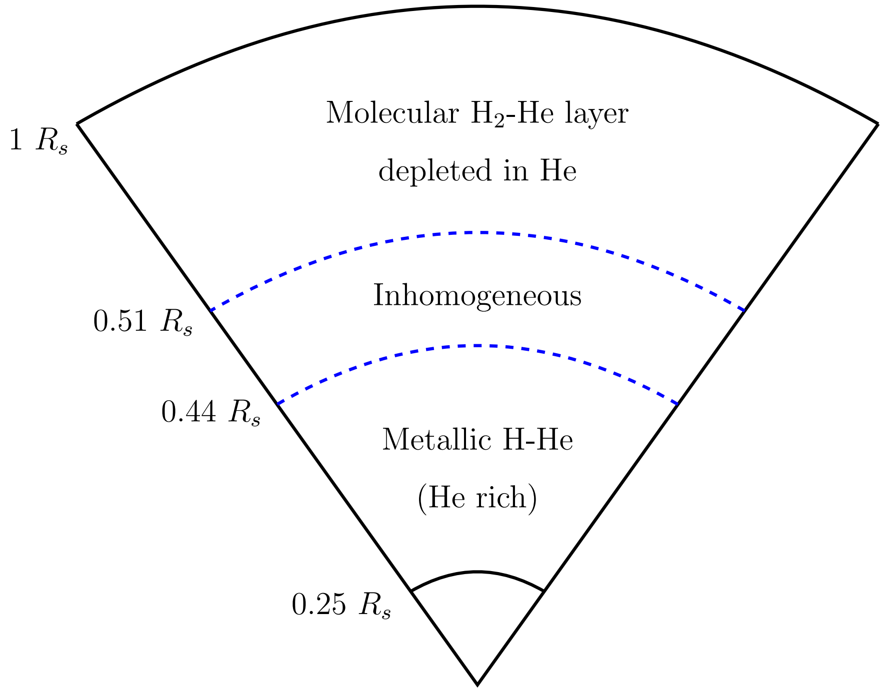

Figure 1.2: Internal structure of Saturn originally proposed by Stevenson. The core is believed to be made of ice and rock. The dashed line represents approximately the stratified layer, with corresponding radii (Stevenson, 1982a) – these are yet to be determined precisely.

This model also supports a dynamo region to sustain the magnetic field which would operate at depth. Under high pressures, hydrogen transitions to a metallic phase (Stixrude & Jeanloz, 2008); the pressures required for this process would be found in the deep interior of Saturn. This metallization is due to the pressure decreasing the energy valence gap, enabling the electrons to escape from the atomic structure, thus allowing for electrical conduction. As a result, there is an electrically conducting fluid region below the stratified layer that could generate the magnetic field. The depth at which it operates would also explain the relative weakness of the observed magnetic field (Jones, 2011).

Spherical shell models have been produced that replicate the magnetic field of Saturn reasonably well and although dipolar dominated fields can be produced without a stable layer, the suppression of non-axisymmetric components by the stable layer highlights the importance of having one (Christensen & Wicht, 2008). Variable conductivity within stratified layers has been tested for Jupiter-like models (Duarte *et al.*, 2013), whilst variable conductivity for Saturn-like models has only recently been considered (Dietrich & Jones, 2018). The results of Dietrich & Jones (2018) suggest that although fields with a small degree of non-axisymmetry can be generated in models without a stable layer, no model without a stable layer can generate surface fields that are as remarkably axisymmetric as Saturn's.

1.3.2 Excessive surface heat fluxes and planetary evolution

Measuring the surface temperature of the gas giants, Saturn and Jupiter, can give insight into whether internal power sources exist. The first surface temperature calculations go back to the 1920's (Jeffreys, 1923). The result of Jeffreys (1923) was inconclusive to whether an internal power source existed for the gas giants. In hindsight, this inconclusive result was due to technological constraints in accurately measuring the surface temperature.

Later attempts to measure the surface temperature by Low (1966) suggested that in fact an internal heat source would be required in order to fit the observations of excess heat flux. The results of Low were further supported by the measurements of the Voyager 1 and Voyager 2 missions that explored the outer planets throughout the 1980s. An effective temperature of $T_{\text{eff}} = 95\text{K}$ has been measured, which exceeds the calculated black body temperature, or the equilibrium temperature, of $T_{\text{eq}} = 93\text{K}$, indicating that more heat is coming out of Saturn than expected (Hanel *et al.*, 1983).

This difference in temperature was suggested by Stevenson & Salpeter (1977) to be due to gravitational differentiation of helium releasing energy via viscous dissipation (Smoluchowski, 1967). This phase separation has also been discussed by Hubbard (1980) and earlier, in an application to Jupiter, by Salpeter (1973).

Running in parallel to the discussion of H-He sedimentation, equation of state (EOS) models investigating the homogeneous evolution of planetary cooling were developed to see how the gas giants would cool from an initial hot state as they age. Early models with a homogeneous interior predicted a much faster cooling rate and hence a lower temperature for Saturn than what has been observed. This supported the need for helium separation as an internal power source (Pollack *et al.*, 1977). Later models that had inhomogeneous evolution confirmed the requirement for stratification in the interior (Fortney & Hubbard, 2003). These models are also in agreement with the observed helium abundance for Jupiter from the Galileo mission, which measured a different mass mixing ratio to the Voyager missions, suggesting that the originally measured helium depletion is not as low as previously thought (Hubbard *et al.*, 1999). Although phase separation of helium and hydrogen does indeed provide enough energy to match with observations, Fortney & Hubbard (2003) also discuss the possibility of separation of heavier elements for an additional energy source.

1.3.3 Asteroseismology

As a relatively new piece of evidence for the existence of the stable layer, the development of seismic techniques in astrophysical objects, asteroseismology, has allowed us to probe the interior of Saturn through wave patterns in Saturn's C and D-rings.

Wave-like structures and patterns within the rings of Saturn have been observed from both Voyager and Cassini radio occultation data (Rosen *et al.*, 1991a). Initially, the presence of outwardly spiralling wave patterns was explained by the gravitational perturbations of the orbiting satellites, whilst Rosen *et al.* (1991b) noticed unexplained inwardly propagating spiral waves. Marley & Porco (1993) predicted that these inward spirals were due to Saturn's oscillation modes interacting with the C-ring but, due to insufficient data from the Voyager mission, their progress was limited.

Cassini radio occultation data provided much more detail into the ring oscillations. Hedman & Nicholson (2013) used this data to measure the properties of the waves in Saturn's C-ring and found that they supported the prediction made by Marley & Porco (1993) twenty years earlier. Given this, Fuller *et al.* (2014) applied models of Saturn to elucidate the internal structure via the observed wave frequencies and found that a solid inner core can be associated with f-mode propagation in the rings. However, a lack of degenerate mixing meant that the effect of stratification could be used to explain this phenomena.

A model that included stable stratification deep within the interior was developed to explain the degenerate mixing (Fuller, 2014). It was found that some of the frequencies observed in the C-ring could not be obtained without the presence of a stable region, which allows for gravity modes to propagate. The model also predicted further frequencies that may not be detectable within the rings due to their weakness. For a further description of the different oscillation modes see Fuller *et al.* (2014), and for details on the mathematics of waves within planetary rings see Shu (1984).

1.4 A plane layer model of the stratified layer

The first attempts to explain the axisymmetry of Saturn's magnetic field were performed by Stevenson (1982b), who considered a localized Cartesian plane layer model. In a kinematic model, in which the velocity field is prescribed *a priori* and the magnetic field evolves under the magnetic induction equation, the non-axisymmetric radial field was shown to be attenuated under the influence of a thermal shear. This suggested that, at least in the kinematic theory, the stable layer does indeed play a role in the observed surface magnetic field. Stevenson suggested that this thermal shear was driven by a pole-equator temperature difference. The strength of the thermal shear in this model was controlled by the magnetic Reynolds number, Rm, which is a nondimensional ratio of the magnetic induction and magnetic diffusivity.

Stevenson (1982b) considered an extension to tackle the dynamic regime model in which the momentum equation is also included in the calculation of the velocity field. Stevenson highlighted the consequences of Taylor's constraint; however, a full analysis was not considered in this paper.

1.4.1 Driving mechanism behind the zonal flow

Although the prescribed azimuthal shear flow in the Stevenson model is, in some respects, a mathematical convenience, the physical implications are justified by a pole-equator temperature difference driving a thermal wind. Solar insolation, whilst effective on Earth and is the major contributor to the driving of atmospheric currents, could be one possibility (Stanley, 2010). However, the latitudinal distribution of the surface temperature is uniform for Saturn suggesting that the deeper atmosphere redistributes the heat leading to the measured surface temperature profile. Rotating convection in spherical shells generating zonal flows have been studied previously (Aubert, 2005), whilst the effect of heat transfer has also been further considered by Jonathan *et al.* (2008) and provides a possible explanation for both the zonal flow in the interior and the surface temperature profile. This would allow for the attenuation of the non-axisymmetric magnetic field within the stable layer due to the convection in the molecular envelope above generating a pole-equator temperature gradient. Such conditions have been considered for spherical models imposing a cold pole and warm equator by Stanley (2010) with smaller dipole tilts occurring in the above case.

1.4.2 Thesis structure

This thesis has the following structure. In Chapter 2 we investigate the kinematic regime by prescribing the shear flow, akin to the Stevenson model, and solve for the magnetic field with variable electrical conductivity. Chapter 3 then sets up the extended model by including the momentum equation into our calculation; Taylor's constraint is then derived for the dynamic regime in a Cartesian geometry. Chapter 4 considers asymptotic solutions to the dynamic model for an inviscid fluid for $\mathrm{Rm} \to 0$. Although Rm is large in Saturn, the low Rm limit allows analytic solutions to be found, which greatly helps develop understanding of the complex nonlinear behaviour of the dynamical models. Chapter 5 introduces the numerical methodology and Chapter 6 contains the numerical solutions for finite values of Rm and the viscosity parameter Ha, the Hartmann number. Chapter 7 returns to the asymptotic theory, this time for viscous solutions, and Chapter 8 considers some recent results from the horizontal field case. We discuss our conclusions in Chapter 9.

Chapter 2

Extension of the kinematic plane layer model

This thesis is motivated by the plane layer model analysis of Stevenson (1982b). In this chapter we present the description of the ansatz and begin by extending the kinematic problem to include the effects of variable conductivity and different velocity profiles. Throughout this thesis we focus on a Cartesian geometry for analytical and numerical ease. Subsequent chapters will extend the analysis to the dynamic regime and will contain a separate derivation of the basic equations.

2.1 Mathematical set up

We consider a layer, height d, of conducting fluid above a dynamo-generating region and below an insulating layer. In a Cartesian geometry, z corresponds to extending radially outwards, with $z = 0$ at the bottom of the layer (near the dynamo region) and $z = d$ the top of the layer (near the insulating boundary). The layer is unbounded in both x, which represents the azimuthal direction, and y, the meridional direction. In the layer, there is an incompressible shear flow $\mathbf{u} = \omega_0 z \hat{\mathbf{x}}$. For simplification, we do not consider the field inside the dynamo region at any point throughout this thesis; we are primarily concerned with the dynamics within the stratified layer.

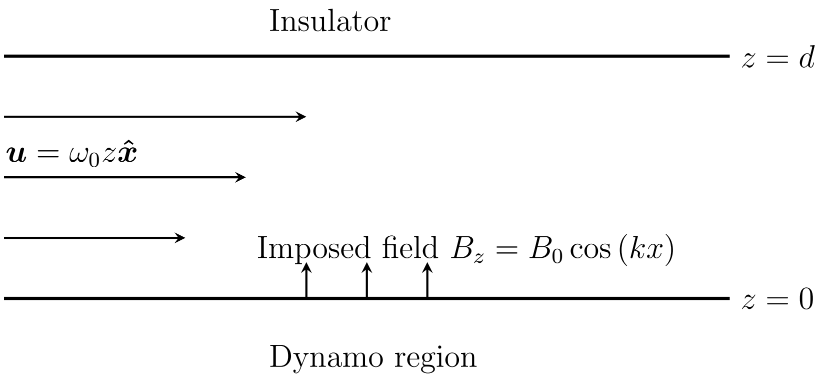

Figure 2.1: Plane layer setup

The magnetic field in the dynamo region beneath is modelled simply by imposing the field $B_0 \cos(kx) \hat{\boldsymbol{z}}$ at the lower boundary, $z = 0$. This corresponds to a non-axisymmetric magnetic field coming out of the dynamo region, this being appropriate as dynamo generated fields are non-axisymmetric (Cowling, 1933). Axisymmetric components in this model correspond to fields in the y and z directions which are independent of x. These components are not affected by the shear, so they are able to reach the surface. We concentrate here on the nonaxisymmetric component, which is attenuated by the shear. The field satisfies the solenoidal condition,

$$\nabla \cdot \boldsymbol{B} = 0, \tag{2.1}$$

and the induction equation,

$$\frac{\partial \boldsymbol{B}}{\partial t} = \nabla \times (\boldsymbol{u} \times \boldsymbol{B}) - \nabla \times (\eta \nabla \times \boldsymbol{B}), \tag{2.2}$$

where η is the magnetic diffusivity. We look for steady solutions, i.e. with $\partial/\partial t = 0$, and consider a 2D magnetic field in the x-z plane. The field is expressed in terms of a magnetic potential $A(x, z)$ as,

$$\boldsymbol{B} = \nabla \times A(x, z) \hat{\boldsymbol{y}}, \tag{2.3}$$

and the flow in terms of the stream function $\psi(x, z)$,

$$\boldsymbol{u} = \nabla \times \psi(x, z) \hat{\boldsymbol{y}}. \tag{2.4}$$

At this stage of the analysis there is no $\hat{\boldsymbol{y}}$ component of the flow; this will be included in subsequent chapters. The following the dimensionless quantities are introduced

$$z = dz^*, \tag{2.5a}$$

$$k = \frac{k^*}{d}, \tag{2.5b}$$

$$\eta = \eta_0 \eta^*, \tag{2.5c}$$

$$\mathrm{Rm} = \frac{\omega_0 d^2}{\eta_0}, \tag{2.5d}$$

where η_0 is the coefficient of diffusion. k represents the azimuthal wavenumber in a Cartesian geometry and is related to the spherical azimuthal wavenumber m. In Saturn the least non-axisymmetric wavenumber corresponds to a wavelength λ that is the circumference of the planet. This can be calculated as

$$k = \frac{2\pi}{\lambda}. \tag{2.6}$$

Given a radius of $r = 58,000$km and a stratified layer thickness of 3000km as suggested by Stevenson would result in $k^* \approx 0.05$. By substituting (2.3) and (2.4) into the steady form of (2.2), the z-component becomes,

$$\frac{\partial}{\partial x}\left(\eta \nabla^2 A + \frac{\partial (A, \psi)}{\partial (x, z)}\right) = 0. \tag{2.7}$$

Since the potential has x-dependence of the form e^{ikx},

$$A(x, z) = A(z)\, e^{ikx}, \tag{2.8}$$

substitution of (2.8) into equation (2.7) gives the following dimensionless ODE

$$\frac{\mathrm{d}^2 A}{\mathrm{d}z^2} - k^2 A = \frac{ik}{\eta} \mathrm{Rm} z A, \tag{2.9}$$

where Rm is the magnetic Reynolds number. Note that the asterisk notation has been dropped for ease so all quantities in (2.9) are dimensionless. Equation (2.9) describes the behaviour of the magnetic field in the layer under the influence of an azimuthal shear. The parameter Rm can be interpreted as the strength of the shear flow with respect to the conductivity within the layer. For a constant diffusivity throughout the layer, one can set $\eta = 1$. Equation (2.9) is a second order ODE and thus requires two boundary conditions for the particular solution $A(x, z)$. At the bottom of the layer, $z = 0$, we assume that a dynamo source is continuously producing a field of maximum strength B_0 in the radial direction, i.e.

$$B_z = B_0 \cos(kx). \tag{2.10}$$

In terms of the potential field $A(x, z)$, this is essentially

$$A = A_0 \sin(kx) \tag{2.11}$$

at $z = 0$. At the top of the layer, $z = d$, there is an insulating boundary at which there is no current, $\boldsymbol{J}$, in the insulating region so

$$\boldsymbol{J} = \frac{1}{\mu}\nabla \times \boldsymbol{B} = 0 \tag{2.12}$$

here, where μ is the magnetic permeability. The magnetic field acts as a potential field in this region and extends to infinity. Combining (2.1), (2.3) and (2.12) this gives

$$\nabla^2 A = \frac{\partial^2 A}{\partial z^2} + \frac{\partial^2 A}{\partial x^2} = 0; \tag{2.13}$$

since the x-dependence is of the form $\sin(kx)$ this would imply,

$$\frac{\partial^2 A}{\partial z^2} = k^2 A, \tag{2.14}$$

i.e. the z-dependence is of the form

$$A \sim e^{-kz}. \tag{2.15}$$

The radial and azimuthal magnetic field, B_x and B_z, must also be continuous across the boundary $z = 1$ leading to the boundary condition

$$\frac{\partial A}{\partial z} = -kA. \tag{2.16}$$

The magnetic potential is thus governed by (2.9) with boundary conditions (2.11) and (2.16).

2.1.1 Constant diffusivity

The simplest case we can consider is η constant. By considering finite Rm solutions with $k^2 \ll k\mathrm{Rm}$, (2.9) reduces to,

$$\frac{\mathrm{d}^2 A}{\mathrm{d}z^2} = ik\mathrm{Rm}zA. \tag{2.17}$$

Although this looks relatively simple – a second order, linear, homogeneous ODE – its solution is expressed in terms of special functions. By applying (2.11) and (2.16), the solution to (2.17) is

$$\begin{aligned} A\left(z\right) =&A_0 z^{1/2}\left\{\left[H^{(2)}_{1/3}\left(\frac{\sqrt{2}}{3}\left(1-i\right)\left(k\mathrm{Rm}\right)^{1/2}z^{3/2}\right)\right.\right.\\ &+\exp\left(\frac{-2\sqrt{2}}{3}\left(k\mathrm{Rm}\right)^{1/2}\left(1+i\right)+\frac{5i\pi}{6}\right)H^{(1)}_{1/3}\left(\frac{\sqrt{2}}{3}\left(1-i\right)\left(k\mathrm{Rm}\right)^{1/2}z^{3/2}\right)\Bigg]\\ &\left.\times\exp\left(ikx-\frac{7i\pi}{12}\right)\right\}+\mathrm{c.c.}, \end{aligned} \tag{2.18}$$

where $H^{(1)}_\nu$ and $H^{(2)}_\nu$ are Hankel functions of the first and second kind of order ν (Abramowitz & Stegun, 1964). We now compare the solution (2.18) with a BVP solver in MATLAB to see whether they match well. As expected, for $k \ll \mathrm{Rm}$ the analytical solution (2.18) matches very well with the `bvp4c` solution in figure 2.2. Figure 2.3 shows solutions for $k \sim \mathrm{Rm}$, where the analytic solution (2.18) is not valid. Larger values of k correspond to shorter wavelengths – physically these will be attenuated much more easily than the longer wavelengths (small k); this can be seen in figure 2.3.

With this in mind, we can now begin to expand on the 1D problem with confidence by including more physical assumptions. In figure 2.4 we have compared the solution to (2.9) for $k = 1$ at increasing values of Rm to see how the field attenuates in the layer. At lower values of Rm it is not necessarily the case that the non-axisymmetric radial component of the magnetic field is attenuated entirely. This is expected, as at low Rm the shear is not strong enough to attenuate the non-axisymmetric radial component completely.

It is apparent that removing some of the simplifications we have made will mean more physically realistic behaviour can be studied, whether this be by additional physical terms, or extending to consider more than one spatial dimension. However this comes at the cost of intractable analytical solutions; in order to proceed we must now consider numerical solutions throughout.

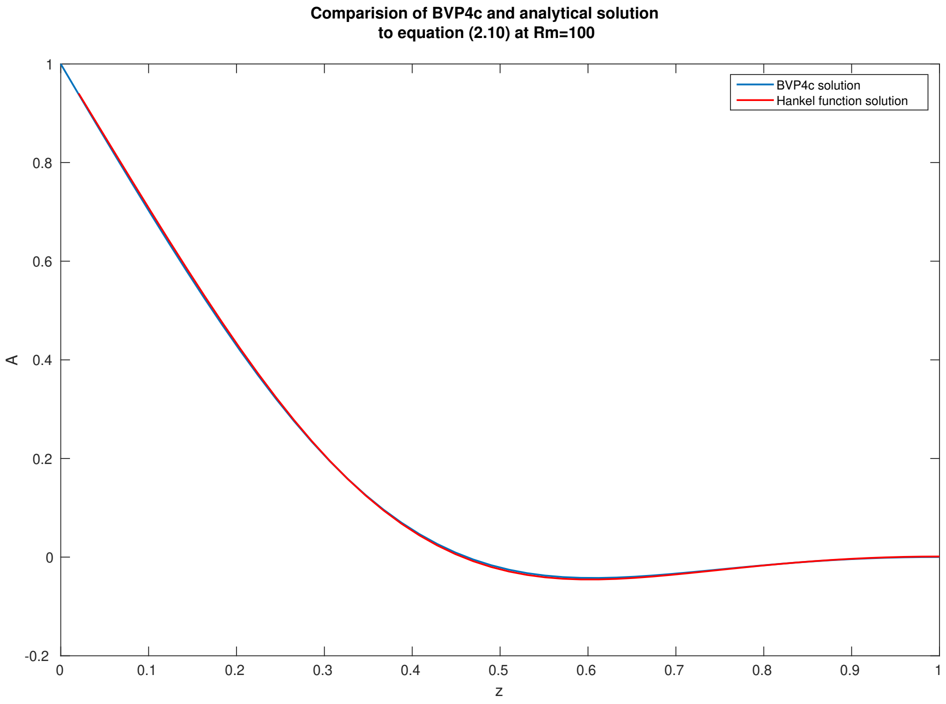

Figure 2.2: A comparison of the analytical solution (2.18) and the BVP solution to (2.17) with $k = 1$ and $\mathrm{Rm} = 100$.

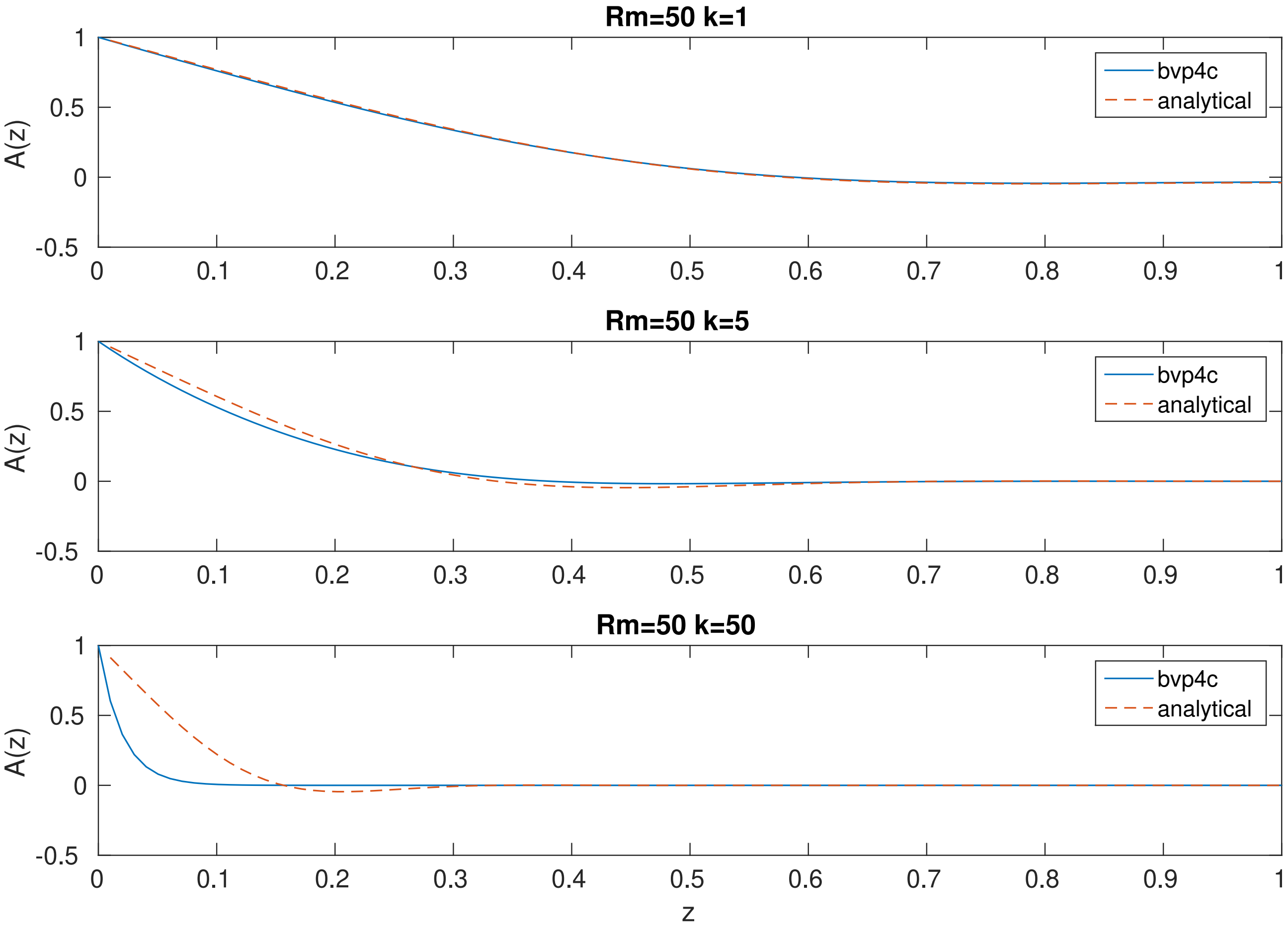

Figure 2.3: A comparison of the analytical solution (2.18) and the BVP solution to (2.9) for Rm = 50 and increasing k.

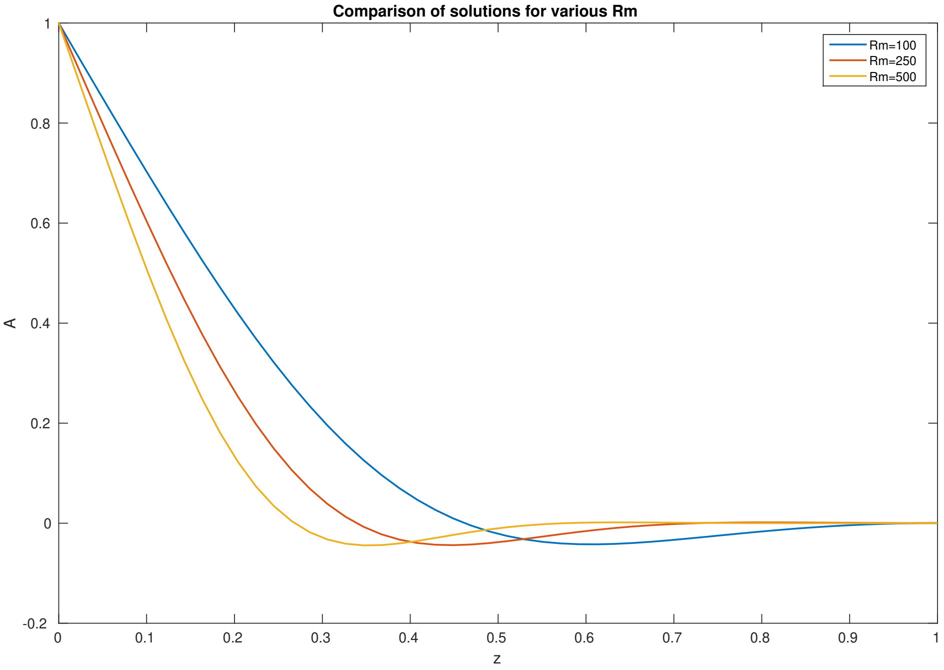

Figure 2.4: Comparison of the field for increasing values of Rm ($k = 1$ for all three cases).

2.1.2 Variable conductivity

In reality, a depth-dependent conductivity would exist in the interior (French *et al.*, 2012). We expect that the conductivity drops off gradually between the base of the dynamo region and the top of the stratified layer, as opposed to a constant conductivity throughout (Jones, 2011).

The z-component of the magnetic induction equation when $\eta = \eta(z)$ is spatially dependent is still given by equation (2.9). Expressing the magnetic diffusivity in terms of the electrical conductivity allows the insulating property to be properly attained at the top of the layer i.e. $\eta \to \infty$. The relationship between electrical conductivity and magnetic diffusivity is

$$\eta = \frac{1}{\mu\sigma}, \tag{2.19}$$

where μ is the electrical permeability and σ is the electrical conductivity. All conductivity profiles we will investigate in the 2D case have the property $\sigma(1) = 0$, i.e. an insulator at $z = 1$. We can compare the attenuation of the magnetic field for a range of conductivity profiles. The constant conductivity case is compared to three different profiles: $\sigma_1(z) = 1 - z$, $\sigma_2(z) = (1 - z)\, e^{z}$ and $\sigma_3(z) = (1 - z)\, e^{-z}$. The choice of these functions is simply to compare smoothly changing profiles with the more abrupt constant diffusivity drop off at the insulating boundary.

In figure 2.5 we can see that the decreasing conductivity profiles are less effective at removing the non-axisymmetric field. At $\mathrm{Rm} = 10$ the original constant conductivity profile (blue) attenuates the field entirely by the time it reaches the insulating region, whilst with the other three profiles are less effective at attenuating the magnetic field within the layer. We can see that conductivity plays a role in the attenuation of the non-axisymmetric field for the linear kinematic problem. The nature of the conductivity profile in the inhomogeneous layer will change the value of Rm at which we see an axisymmetric surface field.

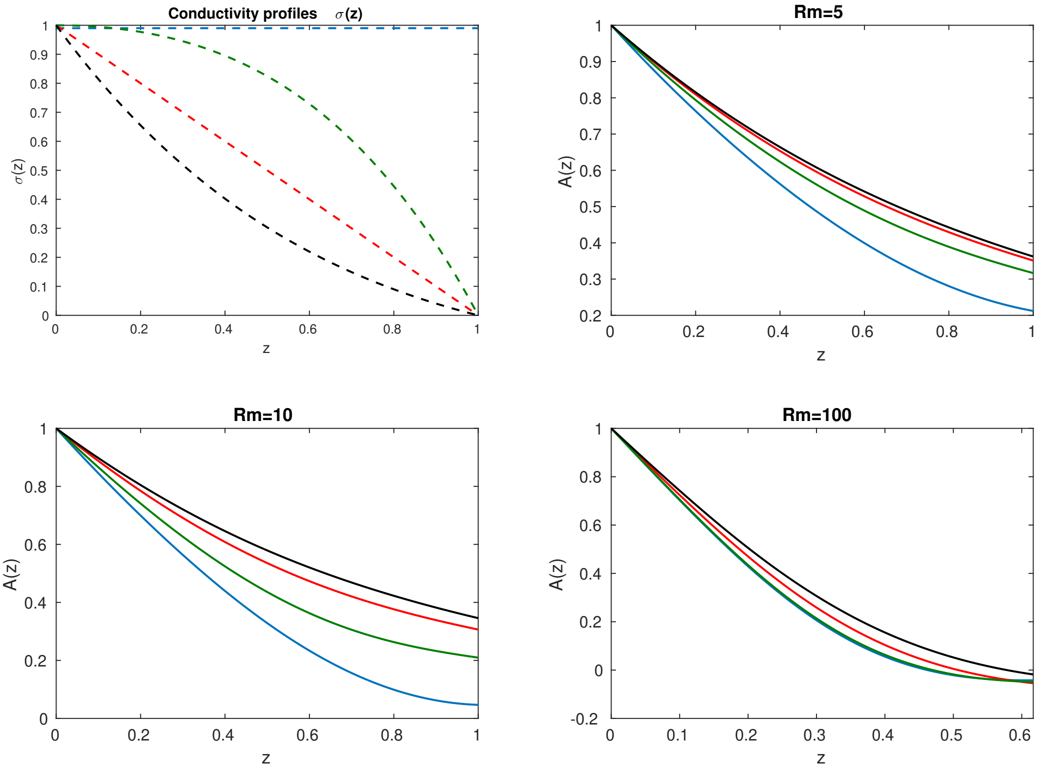

Figure 2.5: A comparison of the field at various Rm for the conductivity profiles: constant (blue), σ_1 (red), σ_2 (green) and σ_3 (black).

2.2 The 3D solution

The problem is now extended to three spatial coordinates. We express the magnetic field in a poloidal-toroidal decomposition (Jones, 2008) as

$$\boldsymbol{B}\left(x,y,z\right)=\nabla\times T\left(x,y,z\right)\hat{\boldsymbol{z}}+\nabla\times\nabla\times P\left(x,y,z\right)\hat{\boldsymbol{z}}+B_x\left(z\right)\hat{\boldsymbol{x}}+B_y\left(z\right)\hat{\boldsymbol{y}}. \quad (2.20)$$

$B_x\left(z\right)$ and $B_y\left(z\right)$ are the mean parts of the field; however both are zero because we are going to consider fields fluctuating in x and y. The flow is again a function only of z,

$$\boldsymbol{u}=u\left(z\right)\hat{\boldsymbol{x}}. \quad (2.21)$$

We seek plane wave solutions of the form,

$$T\left(x,y,z\right)=T\left(z\right)e^{i(kx+ly)}, \tag{2.22}$$

$$P\left(x,y,z\right)=P\left(z\right)e^{i(kx+ly)}, \tag{2.23}$$

where k and l are the wavenumbers associated with the azimuthal and meridional directions respectively. To solve for both T and P we require two equations. The expansion (2.20) is substituted into (2.2) and the curl of (2.2). The z-components are,

$$\frac{\mathrm{d}^2P}{\mathrm{d}z^2}=\left(k^2+l^2\right)P+\frac{iku}{\eta}P, \tag{2.24}$$

$$\frac{\mathrm{d}^2T}{\mathrm{d}z^2}=\frac{il}{\eta}\frac{\mathrm{d}u}{\mathrm{d}z}P+\frac{iku}{\eta}T-\frac{1}{\eta}\frac{\mathrm{d}\eta}{\mathrm{d}z}\frac{\mathrm{d}T}{\mathrm{d}z}+\left(k^2+l^2\right)T, \tag{2.25}$$

where $\eta=\eta\left(z\right)$. Additional terms appear through contributions from the y-spatial dependence these are,

$$\frac{il}{\eta}\frac{\mathrm{d}u}{\mathrm{d}z}P \tag{2.26}$$

and a term that involves the derivative of diffusivity,

$$-\frac{1}{\eta}\frac{\mathrm{d}\eta}{\mathrm{d}z}\frac{\mathrm{d}T}{\mathrm{d}z}. \tag{2.27}$$

Equations (2.24) and (2.25) can be made dimensionless through the scalings,

$$T=dT^*, \tag{2.28a}$$

$$P=d^2P^*, \tag{2.28b}$$

$$\eta=\eta_0\eta^*, \tag{2.28c}$$

$$\boldsymbol{x}=\frac{\boldsymbol{x}^*}{d}, \tag{2.28d}$$

where η_0 is the strength of the magnetic diffusivity. Then (after dropping the asterisk notation for ease) (2.24) and (2.25) become,

$$\frac{\mathrm{d}^2P}{\mathrm{d}z^2}=\left(k^2+l^2\right)P+ik\mathrm{Rm}\frac{u\left(z\right)}{\eta\left(z\right)}P, \tag{2.29}$$

$$\frac{\mathrm{d}^2T}{\mathrm{d}z^2}=il\mathrm{Rm}\frac{1}{\eta\left(z\right)}\frac{\mathrm{d}u}{\mathrm{d}z}P+ik\mathrm{Rm}\frac{u\left(z\right)}{\eta\left(z\right)}T-\frac{1}{\eta}\frac{\mathrm{d}\eta}{\mathrm{d}z}\frac{\mathrm{d}T}{\mathrm{d}z}+\left(k^2+l^2\right)T. \tag{2.30}$$

This coupled pair of ODE's can be solved in `bvp4c`. We first derive the boundary conditions before considering various cases. For the boundary condition at the bottom of the layer ($z = 0$) we impose a radial magnetic field that has both azimuthal and meridional dependence, $B_z = B_0 \cos(kx)\cos(ly)$, giving

$$P(z=0) = \frac{1}{k^2+l^2}\cos(kx)\cos(ly), \tag{2.31}$$

$$T(z=0) = 0. \tag{2.32}$$

The choice of $T = 0$ arises because T does not have a radial component throughout the layer. At the top of the layer ($z = 1$) the field is matched to a potential field satisfying

$$\nabla^2 P = \frac{\partial^2 P}{\partial x^2} + \frac{\partial^2 P}{\partial y^2} + \frac{\partial^2 P}{\partial z^2} = 0. \tag{2.33}$$

This results in

$$\frac{\partial^2 P}{\partial z^2} = \left(k^2+l^2\right)P, \tag{2.34}$$

suggesting that P takes the form of a decaying exponential function depending on k and l,

$$P \sim e^{-\left(k^2+l^2\right)z}. \tag{2.35}$$

Hence our top boundary condition for the poloidal and toroidal field is,

$$\left.\frac{\mathrm{d}P}{dz}\right|_{z=1} = -\sqrt{k^2+l^2}P, \tag{2.36}$$

$$T(z=1) = 0. \tag{2.37}$$

2.2.1 Variable conductivity in the 3D case

Let us now consider the case of a fixed velocity profile $\boldsymbol{u} = z\hat{\boldsymbol{x}}$ with variable conductivity, $\sigma(z)$. The governing equations are

$$\frac{\mathrm{d}^2P}{\mathrm{d}z^2} = \left(k^2+l^2\right)P + \frac{ik\mathrm{Rm}z}{\eta(z)}P, \tag{2.38}$$

$$\frac{\mathrm{d}^2T}{\mathrm{d}z^2} = il\mathrm{Rm}\frac{1}{\eta(z)}P + \frac{ik\mathrm{Rm}z}{\eta(z)}T - \frac{1}{\eta}\frac{\mathrm{d}\eta}{\mathrm{d}z}\frac{\mathrm{d}T}{\mathrm{d}z} + \left(k^2+l^2\right)T. \tag{2.39}$$

We consider two different profiles for the conductivity: one in which the conductivity is concentrated in the lower half of the domain and drops off at the midpoint, and the reverse case, where the conductivity is concentrated in the upper half of the domain. The functional forms of these two profiles are,

$$\sigma_1(z) = \frac{1}{2}\left(1 - \tanh\left(25\left(z - \frac{1}{2}\right)\right)\right), \tag{2.40}$$

$$\sigma_2(z) = \frac{1}{2}\left(1 + \tanh\left(25\left(z - \frac{1}{2}\right)\right)\right). \tag{2.41}$$

Below are the results of investigating the parameter space $0 < k, l < 1$.

In figure 2.6 we have plotted the toroidal and poloidal field for the two conductivity profiles with a flow $u(z) = z$ at $\mathrm{Rm} = 800$. The wavenumber in y is fixed at $l = 0.01$ and the x wavenumber is varied. There is a stark contrast between the toroidal fields for the two conductivity profiles; the toroidal field is strongly dependent on the location of the conducting region with the smaller values of k, corresponding to a longer wavelength in the azimuthal direction, having a larger amplitude. Physically we expect the less non-axisymmetric wavelengths to have a larger amplitude as the shearing effect is less effective here.

For the poloidal field, we see that the field diffuses more or less the same with wavenumber for the $\sigma_1(z)$ profile. For the other conductivity profile, $\sigma_2(z)$, the diffusion is much slower for the poloidal field when the conducting region is situated in the upper half of the domain. There is a greater difference in attenuation with wavenumber for this case too. Unlike the toroidal field, the location of the poloidal field in the layer is not as strongly linked with the location of the conducting region.

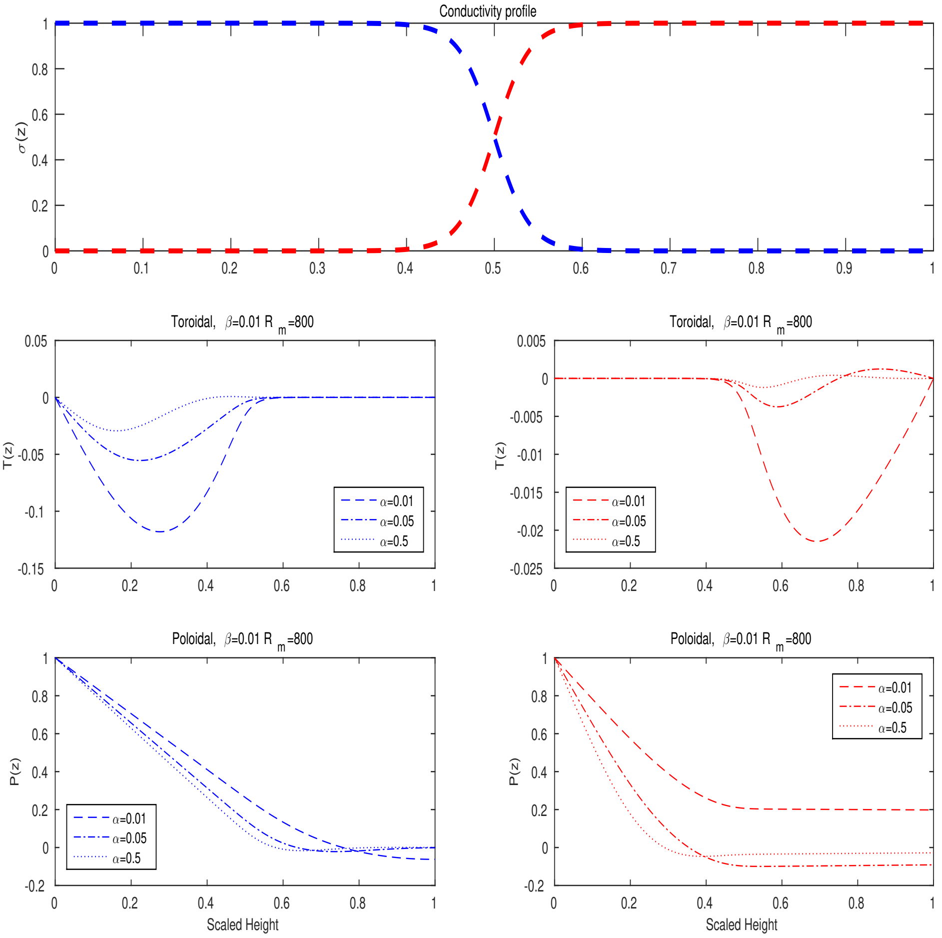

Figure 2.6: A comparison of the poloidal and toroidal field for two different conductivity profiles ($\sigma_1(z)$ in blue and $\sigma_2(z)$ in red) with flow $u = z$ at $\mathrm{Rm} = 800$ and $l = 0.01$ for wavenumbers $k = 0.01, 0.05, 0.5$.

2.2.2 The effect of shear

For the remainder of this chapter, we shall use the conductivity profile that would be similar to that of Saturn's inhomogeneous layer, i.e. equation (2.40). Essentially this would be a conductivity profile that drops off smoothly towards the insulating boundary; in this case we have picked a profile that drops off at $z = 0.5$. Figure 2.7 shows the magnetic field for different velocity profiles in the layer. We have considered two nonlinear profiles such that the $\frac{\mathrm{d}u}{\mathrm{d}z}$ term is no longer constant in (2.30); these are

$$u_1\left(z\right) = \operatorname{sech}^2\left(10z - 5\right), \tag{2.42}$$

$$u_2\left(z\right) = \frac{1}{2}\left(1 - \tanh\left(10z - 5\right)\right). \tag{2.43}$$

These flows are displayed by the red and blue profiles respectively. Physically these can be interpreted as convection within the layer and convection beneath the layer driving the flow, although the physical process of convection within a stratified layer would not make sense; physically this is primarily chosen as a mathematical convenience. The poloidal field for the red velocity profile is quite consistent with increasing wavenumber, there is no drastic change in structure. Comparing the two velocity profiles we see some difference in magnetic field attenuation; although they both attenuate all of the nonaxisymmetric components, the blue profile is much more effective at doing this in the bottom half of the layer. The maximum amplitude of the toroidal field differs greatly between u_1 and u_2 with $\max\left(T\right) = 1.3856, 0.3433, 0.1787$ for u_1 and $\max\left(T\right) = 0.0425, 0.0014, 7.86\times10^{-5}$ for u_2 for $\alpha = 1, 0.5, 0.1$ respectively. The amplitude of the field is connected to the strength and location of the shearing effect. In the u_2 profile the shear is concentrated in the lower half of the domain and, as a result, is immediately influencing the structure of the toroidal field at the base of the layer. Since there is no toroidal field being produced at $z = 0$ the strong shearing suppresses any toroidal field from being produced in the conducting region.

In the case of u_2, because the shearing effect does not begin until the mid-point of the layer, the toroidal field has time to grow in amplitude throughout the conducting region. In figure 2.7 we can see that the growth in toroidal field in the lower half is slower than the decay in the region of shear.

The linear solutions provide some insight into the behaviour of the non-axisymmetric components of the magnetic field. It now makes sense to follow on from this and look at the consequences of introducing nonlinearities by introducing the momentum equation. This poses a series of questions: under what conditions do we have the Stevenson ansatz? what physical mechanism could be driving the shear in the inhomogeneous layer? and what will happen to the flow when the back reaction of the Lorentz force take place?

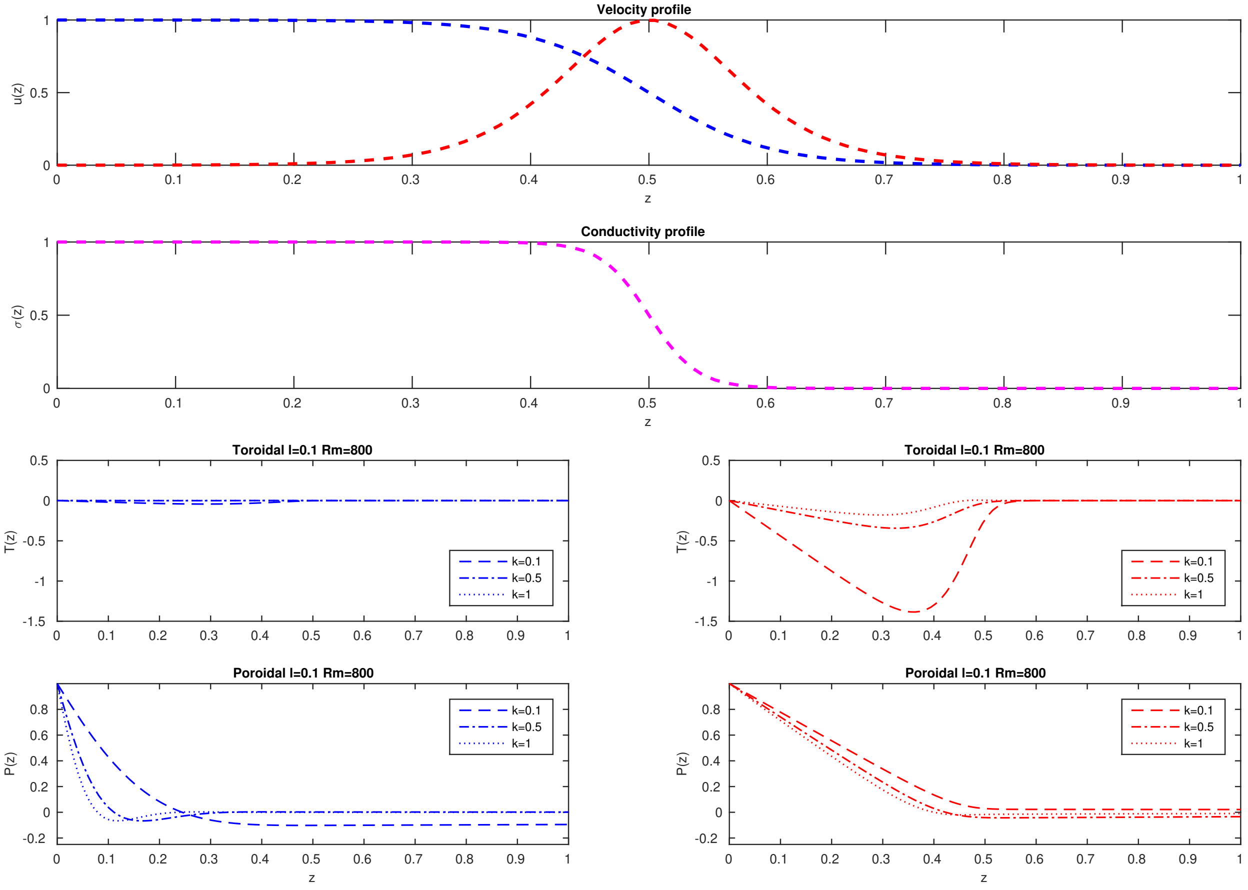

Velocity profile

Conductivity profile

Toroidal l=0.1 Rm=800

Toroidal l=0.1 Rm=800

Poroidal l=0.1 Rm=800

Poroidal l=0.1 Rm=800

Figure 2.7: Toroidal and poloidal field for different velocity profiles u_1 (red) and u_2 (blue) at $\mathrm{Rm} = 800$, $l = 0.1$ for wavenumbers $k = 0.1, 0.5, 1$.

Chapter 3

Model set up in the dynamical regime

3.1 Introduction

Here we wish to investigate the effects of the dynamic regime for a stratified plane layer model. This is more complicated than the kinematic study of Chapter 2 as we now need to consider the momentum equation,

$$\frac{\partial \boldsymbol{u}}{\partial t} + \boldsymbol{u} \cdot \nabla \boldsymbol{u} + 2\boldsymbol{\Omega} \times \boldsymbol{u} = -\frac{1}{\rho}\nabla \Pi + \frac{1}{\rho}\boldsymbol{J} \times \boldsymbol{B} + \nu \nabla^2 \boldsymbol{u} + \boldsymbol{F}_\theta. \tag{3.1}$$

The first two terms in (3.1) are related to the acceleration of the fluid; $\partial_t \boldsymbol{u}$ is the acceleration and $\boldsymbol{u} \cdot \nabla \boldsymbol{u}$ is the inertial acceleration. Π is the pressure, $\boldsymbol{J}$ is the current density, ν is the kinematic viscosity and $\nu \nabla^2 \boldsymbol{u}$ is the viscous diffusion term. The final term is the buoyancy force representing the effect of convection.

The various balances between terms in the momentum equation also introduce new dimensionless parameters. The magnetic Reynolds number, Rm, which is a balance between the imposed shear and the magnetic diffusivity in the layer, is considered. We will be considering the balance between the Coriolis force and the Lorentz force, this is represented by the Elsasser number,

$$\Lambda = \frac{|(\nabla \times \boldsymbol{B}) \times \boldsymbol{B}|}{|2\mu\rho\boldsymbol{\Omega} \times \boldsymbol{u}|}, \tag{3.2}$$

and the balance between the magnetic field strength and viscosity, this is represented by the Hartmann number,

$$\mathrm{Ha}^2 = \frac{\Lambda}{\mathrm{E_k}}. \tag{3.3}$$

The Hartmann number is defined in terms of Λ and the Ekman number $\mathrm{E_k}$, where the Ekman number is a dimensionless measure of the ratio between viscous diffusion and the Coriolis force,

$$\mathrm{E_k} = \frac{|\nu \nabla^2 \boldsymbol{u}|}{|2\boldsymbol{\Omega} \times \boldsymbol{u}|}. \tag{3.4}$$

In planetary cores, the common assumption is that $\Lambda \sim 1$, i.e. Coriolis and Lorentz forces balance. In this thesis we shall consider, for ease of analysis, small Elsasser solutions; although this is not physically accurate in a planetary application, it provides some insight into the behaviour of the equations.

3.2 System of equations

Our model follows from Chapter 2; a non-axisymmetric radial magnetic field of maximum strength B_0, generated from the dynamo region, is prescribed at $z = 0$ whilst a constant horizontal field of strength B_H exists throughout the layer. A pole-equator temperature gradient drives an azimuthal thermal shear profile within the layer, that acts on the magnetic field. An insulating region exists at the top of the layer ($z = 1$) and both top and bottom boundaries are considered to be impenetrable. The layer is under the influence of rotation with the Coriolis vector defined as,

$$\boldsymbol{\Omega} = \Omega_0 \left(0, \cos\vartheta, \sin\vartheta\right), \tag{3.5}$$

where ϑ is the angle measured from the equator to the plane (see fig. 3.1).

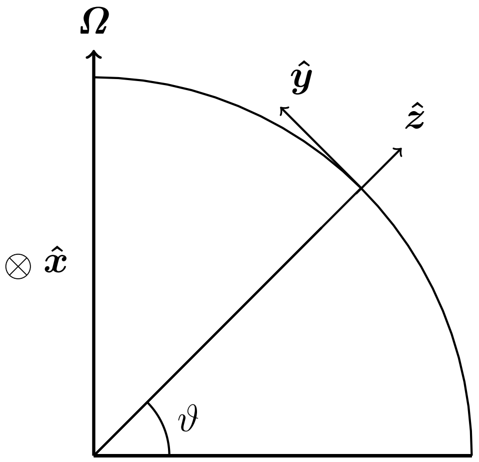

Figure 3.1: Schematic of the Coriolis vector on the sphere in relation to the plane layer.

The magnetic field, which we shall assume is independent of y, takes the form,

$$\boldsymbol{B} = \nabla \times A\left(x,z\right)\hat{\boldsymbol{y}} + H\left(x,z\right)\hat{\boldsymbol{y}} + B_H\hat{\boldsymbol{x}}, \tag{3.6}$$

and obeys the magnetic induction equation,

$$\frac{\partial \boldsymbol{B}}{\partial t} = \nabla \times \left(\boldsymbol{u} \times \boldsymbol{B}\right) - \nabla \times \left(\eta \nabla \times \boldsymbol{B}\right), \tag{3.7}$$

where η is the magnetic diffusivity. $A\left(x,z\right)$ is the magnetic potential and acts in both the radial (z) and azimuthal (x) direction, $H\left(x,z\right)$ is the meridional magnetic field and exists in the meridional (y) direction, and B_H is the constant azimuthal field. Since the layer is thin with respect to the radius (i.e. $L \ll R$), the lengthscale of B_H is long in the azimuthal direction and so it is reasonable to assume that it could appear constant with respect to the thin layer. The magnetic field also obeys the Maxwell equation,

$$\nabla \cdot \boldsymbol{B} = 0. \tag{3.8}$$

The current density is,

$$\boldsymbol{J} = \mu^{-1}\nabla \times \boldsymbol{B}, \tag{3.9}$$

where μ is the magnetic permeability. Equation (3.9) has y-component,

$$J_y = -\mu^{-1}\left(\frac{\partial^2 A}{\partial x^2} + \frac{\partial^2 A}{\partial z^2}\right). \tag{3.10}$$

We consider an incompressible and steady flow that is independent of y. The flow satisfies the equation of motion

$$2\left(\boldsymbol{\Omega}\times\boldsymbol{u}\right)\rho = -\nabla\Pi + \boldsymbol{J}\times\boldsymbol{B} + \rho\nu\nabla^2\boldsymbol{u} + \rho g\alpha T_0\left(y\right)\hat{\boldsymbol{z}}, \tag{3.11}$$

where α is the coefficient of thermal expansion. The final term in (3.11) is a buoyancy term that has a meridional temperature dependence i.e. we have a constant temperature gradient from pole to equator. We have assumed that the differences in y differ much more than in z and so $T_0\left(y\right)$ is a function of y only. Pole-equator temperature gradients lead to thermal winds, such as the jet stream in Earth's atmosphere. They may be responsible for the differential rotation that lies at the heart of the Stevenson model. The origin of this temperature gradient is due to the outer convection zone having convection that is dependent on rotation, affecting the heat transfer in this part of the atmosphere – this was discussed in the introduction in §1.4.1. We write the flow as

$$\boldsymbol{u} = U_0\left(z\right)\hat{\boldsymbol{x}} + \nabla\times\psi\left(x,z\right)\hat{\boldsymbol{y}} + v\left(x,z\right)\hat{\boldsymbol{y}},$$

where $\psi\left(x,z\right)$ is the stream function, $v\left(x,z\right)$ is the meridional velocity field and $U_0\left(z\right)$ is the shear profile driven by the buoyancy term. $\boldsymbol{u}_0 = U_0\left(z\right)\hat{\boldsymbol{x}}$ is the solution of taking the curl of (3.11),

$$-2\left(\boldsymbol{\Omega}\cdot\nabla\right)\boldsymbol{u}_0 = \nabla\times g\alpha T_0\hat{\boldsymbol{z}}, \tag{3.12}$$

with x-component,

$$-2\Omega_0\sin\vartheta\frac{\partial u_0}{\partial z} = g\alpha\frac{\mathrm{d}T_0}{\mathrm{d}y} = g\alpha T_0'\left(y\right). \tag{3.13}$$

As $T_0'\left(y\right)$ is a constant, we have,

$$u_0 = -\frac{g\alpha T_0'}{2\Omega_0\sin\vartheta}z + \mathrm{const} \tag{3.14}$$

Without loss of generality we choose the constant to be zero, and hence

$$u_0 = \gamma z, \tag{3.15}$$

where

$$\gamma = -\frac{g\alpha T_0'}{2\Omega_0\sin\vartheta}. \tag{3.16}$$

We note that γ has the units time^{-1}. So $\boldsymbol{u}_0(z) = \gamma z\hat{\boldsymbol{x}}$ is the thermal wind that is now driven rather than forced. For ease of analysis, we introduce the scalings,

$$A = B_0 d\tilde{A}, \tag{3.17a}$$

$$J_y = \mathrm{Rm}\frac{B_0}{d^3\mu}\tilde{J}_y, \tag{3.17b}$$

$$v = \mathrm{Rm}\Lambda\frac{\eta}{d}\tilde{v}, \tag{3.17c}$$

$$H = B_0\mathrm{Rm}\Lambda\tilde{H}, \tag{3.17d}$$

$$\psi = \eta\mathrm{Rm}\Lambda^2\tilde{\psi}, \tag{3.17e}$$

where $\sim$ represents a dimensionless quantity. We also introduce the dimensionless numbers

$$\mathrm{Rm} = \frac{\gamma d^2}{\eta}, \tag{3.18a}$$

$$\Lambda = \frac{B_0^2}{2\Omega_0\rho\mu\eta\sin\vartheta}, \tag{3.18b}$$

$$\mathrm{B_s} = \frac{B_H}{B_0}, \tag{3.18c}$$

$$\mathrm{E_k} = \frac{\nu}{2d^2\Omega_0\rho\mu\eta\sin\vartheta}, \tag{3.18d}$$

$$\mathrm{Ha} = \sqrt{\frac{\Lambda}{\mathrm{E_k}}}. \tag{3.18e}$$

The choice of Rm is because γ has units of time^{-1} which means the ratio $\gamma d^2\eta^{-1}$ has the correct dimension of $\frac{UL}{\eta}$ where U and L are a typical velocity and length scale. $\mathrm{B_s}$ determines the ratio between the imposed field at the bottom boundary B_0 and the horizontal field B_H.

The remaining contribution of the flow,

$$\boldsymbol{u}_M = \nabla\times\psi(x,z)\,\hat{\boldsymbol{y}} + v(x,z)\,\hat{\boldsymbol{y}} \tag{3.19}$$

is the magnetic wind $\boldsymbol{u}_M$, which satisfies

$$2(\boldsymbol{\Omega}\times\boldsymbol{u}_M)\rho = -\nabla\Pi_M + \boldsymbol{J}\times\boldsymbol{B} + \rho\nu\nabla^2\boldsymbol{u}_M, \tag{3.20}$$

where Π_M is the magnetic pressure, and is independent of y, this being consistent with the magnetic field and $\boldsymbol{u}_M$ being independent of y. The y-component of (3.20) is,

$$\frac{\partial \psi}{\partial z} = \frac{\partial (H, A)}{\partial (x, z)} - \mathrm{B_s}\frac{\partial H}{\partial x} - \frac{1}{\mathrm{Ha}^2}\left(\frac{\partial^2 v}{\partial x^2} + \frac{\partial^2 v}{\partial z^2}\right). \tag{3.21}$$

$H(x, z)$ is required to be non-zero to generate a meridional circulation contribution to the magnetic wind. The y-component of the curl of (3.20) is

$$\frac{\partial v}{\partial z} = \frac{\partial (J_y, A)}{\partial (x, z)} - \mathrm{B_s}\frac{\partial J_y}{\partial x} + \frac{\Lambda}{\mathrm{Ha}^2}\left(\frac{\partial^4 \psi}{\partial x^4} + \frac{\partial^4 \psi}{\partial z^4} + 2\frac{\partial^4 \psi}{\partial x^2 \partial z^2}\right). \tag{3.22}$$

Note that $J_y(x, z)$ and $A(x, z)$ are non-zero in the kinematic Stevenson problem, this forces non-zero $v(x, z)$ and this then generates a magnetic wind in the dynamic problem. The induction equation, assuming a steady flow is,

$$0 = \nabla \times ((\boldsymbol{u}_0 + \boldsymbol{u}_M) \times \boldsymbol{B}) + \eta \nabla^2 \boldsymbol{B}. \tag{3.23}$$

The y-component of the uncurled induction equation is

$$J_y = -z\frac{\partial A}{\partial x} + \Lambda^2 \frac{\partial (A, \psi)}{\partial (x, z)} + \mathrm{B_s}\frac{\partial \psi}{\partial x}. \tag{3.24}$$

Note that the balance in Stevenson's kinematic theory is just (3.24) with $\psi(x, z) = 0$ meaning that there is no back reaction between the magnetic field and flow. Finally, the y-component of the induction equation is

$$0 = \frac{\partial (A, v)}{\partial (x, z)} - \mathrm{Rm} z\frac{\partial H}{\partial x} + \mathrm{Rm}\Lambda^2 \frac{\partial (H, \psi)}{\partial (x, z)} + \left(\frac{\partial^2 H}{\partial x^2} + \frac{\partial^2 H}{\partial z^2}\right) + \mathrm{B_s}\frac{\partial v}{\partial x}. \tag{3.25}$$

The system is governed by the four coupled PDE's (3.21), (3.22), (3.24) and (3.25), for the four unknowns, A, H, v and ψ. The full set of equations are then,

$$\mathrm{Rm}^{-1}\left(\frac{\partial^2 A}{\partial x^2} + \frac{\partial^2 A}{\partial z^2}\right) = z\frac{\partial A}{\partial x} + \Lambda^2 \frac{\partial (\psi, A)}{\partial (x, z)} - \mathrm{B_s}\Lambda^2 \frac{\partial \psi}{\partial x}, \tag{3.26}$$

$$J_y = -z\frac{\partial A}{\partial x} + \Lambda^2 \frac{\partial (A, \psi)}{\partial (x, z)} + \mathrm{B_s}\Lambda^2 \frac{\partial \psi}{\partial x}, \tag{3.27}$$

$$\frac{\partial v}{\partial z} = \frac{\partial (J_y, A)}{\partial (x, z)} - \mathrm{B_s}\frac{\partial J_y}{\partial x} + \frac{\Lambda}{\mathrm{Ha}^2}\left(\frac{\partial^4 \psi}{\partial x^4} + \frac{\partial^4 \psi}{\partial z^4} + 2\frac{\partial^4 \psi}{\partial x^2 z^2}\right), \tag{3.28}$$

$$\frac{\partial^2 H}{\partial x^2} + \frac{\partial^2 H}{\partial z^2} = \frac{\partial (v, A)}{\partial (x, z)} + \mathrm{Rm} z\frac{\partial H}{\partial x} + \mathrm{Rm}\Lambda^2 \frac{\partial (\psi, H)}{\partial (x, z)} - \mathrm{B_s}\frac{\partial v}{\partial x}, \tag{3.29}$$

$$\frac{\partial \psi}{\partial z} = \frac{\partial (H, A)}{\partial (x, z)} - \mathrm{B_s}\frac{\partial H}{\partial x} - \frac{1}{\mathrm{Ha}^2}\left(\frac{\partial^2 v}{\partial x^2} + \frac{\partial^2 v}{\partial z^2}\right). \tag{3.30}$$

The additional equation (3.27) is also included for J_y. Equations (3.26)–(3.30) form the full set of equations that we shall be investigating throughout the rest of this thesis. In the next chapter we shall consider the simplest case of an inviscid, small Rm, small Λ and $\mathrm{B_s} = 0$ system. In subsequent chapters we will build up to solving the system for small Λ with more general Rm and $\mathrm{B_s}$.

3.3 Boundary conditions

As the magnetic induction equation is second order in $\boldsymbol{B}$, we require two boundary conditions for $\boldsymbol{B}$ in order to determine its full solution. At the top of the dynamo region ($z = 0$) we impose a vertical magnetic field $B_z = B_0 \cos(kx)\,\hat{\boldsymbol{z}}$, in terms of the magnetic potential A, this is,

$$A(x, z) = \frac{B_0}{k} \sin(kx)\,. \tag{3.31}$$

At the top of the stratified layer ($z = 1$) is the insulating region, so we match to a potential field

$$\nabla^2 \boldsymbol{B} = 0. \tag{3.32}$$

The normal component of $\boldsymbol{B}$ is continuous across the interface and this will give us our second boundary condition for the magnetic field potential $A(x, z)$,

$$\frac{\mathrm{d}A}{\mathrm{d}z} = -kA. \tag{3.33}$$

As there is no meridional field imposed at $z = 0$ the meridional field satisfies

$$H(x, z) = 0 \tag{3.34}$$

at both $z = 0$ and $z = 1$. This completes the set of magnetic boundary conditions.

For the mechanical boundary conditions; the bottom and top boundaries are impenetrable, hence the normal velocity (u_z) must vanish. Hence

$$\left.\frac{\partial \psi}{\partial x}\right|_{z=0,1} = 0 \implies \psi = \text{constant on } z = 0, 1. \tag{3.35}$$

Viscous boundary conditions are not required for small Λ, this is because the $\nabla^4 \psi$ term does not appear in (3.28) in limit $\Lambda \to 0$. As a result, this reduces (3.28) from a fourth order equation to a second order equation, and hence we require only the impenetrable boundary condition. When we consider solutions for $\mathrm{Ha} \sim \mathcal{O}(1)$

only the $\mathrm{Ha}^{-2}\nabla^2 v$ term will appear in the governing equations in the limit $\Lambda \to 0$. Mathematically speaking, we are solving the interior solution to the governing equations and the limit $\mathrm{Ha} \to \infty$ is interpreted as "inviscid" – although this is only in the sense of an interior solution. All references to inviscid in this thesis are therefore associated within the interior solution. The choice of $\Lambda \to 0$ allows for analytical solutions to be found and simplifies the numerical approach to this problem.

This completes our boundary conditions on A, H and ψ. At first glance one would immediately question why we have two boundary conditions on ψ for a first order equation. However, in the next chapter we show that the freedom in v is constrained by one of the boundary conditions in (3.35), this additional boundary condition is Taylor's constraint. In the next section we explain what the connection is between Taylor's original constraint in spherical geometry and our Cartesian version of the constraint.

3.3.1 Taylor's constraint

A fundamental result which lies at the heart of the problem in the dynamic regime, and as a consequence, this thesis, is Taylor's constraint (Taylor, 1963).

Taylor's constraint is derived from the magnetostrophic limit of the Navier-Stokes equation. This limit is believed to be the case in planetary interiors, where the Rossby number, the balance between rotation and inertial forces

$$\mathrm{Ro} = \frac{|\boldsymbol{u}\cdot\nabla\boldsymbol{u}|}{|2\boldsymbol{\Omega}\times\boldsymbol{u}|} \tag{3.36}$$

and the Ekman number, (3.4), are small. Since our problem is independent of y, Taylor's constraint enters in a rather unusual way. In this section we describe the usual way Taylor's constraint enters planetary dynamo theory, and then we discuss how a similar constraint is relevant to our problem.

In a spherical geometry, Taylor's constraint arises when the magnetostrophic limit of the Navier-Stokes equation is integrated over a cylinder. The magnetostrophic limit of the Navier-Stokes equation is

$$2\rho\boldsymbol{\Omega} \times \boldsymbol{u} = -\nabla\Pi + \boldsymbol{J} \times \boldsymbol{B} + F_T\hat{\boldsymbol{z}}, \tag{3.37}$$

where F_T is the buoyancy term in the radial direction. A caveat of (3.37) is that a solution may not exist at all and, as a consequence, Taylor's constraint must be applied in order for a solution to exist. The ϕ-component of equation (3.37) is integrated with respect to ϕ and z (cylindrical) (see figure 3.2); the buoyancy term has no ϕ-component and vanishes, whilst the pressure term must also vanish as it must be continuous in ϕ, the Coriolis force also vanishes as there is no net flow across the cylinder. What remains is the integral of the Lorentz force and as result the integration of (3.37) over the cylinder becomes

$$\int_{C(s)} (\boldsymbol{J} \times \boldsymbol{B})_\phi \, \mathrm{d}z\mathrm{d}s = 0. \tag{3.38}$$

The physical interpretation of (3.38) is a restriction on zonal Lorentz torques, as not all of these torques can be balanced the Coriolis force in this limit.

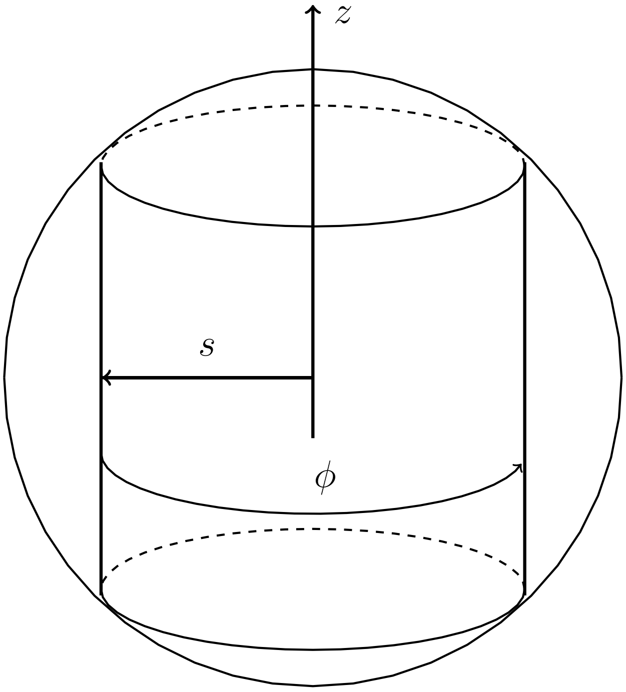

Figure 3.2: The coaxial cylinder in which the magnetostrophic limit of Navier-Stokes is integrated over.

In order to satisfy (3.38) a "free" geostrophic velocity, $V_\phi(s)$, is required that can change the structure of the magnetic field $\boldsymbol{B}$ and hence change $\boldsymbol{J}\times\boldsymbol{B}$ such that (3.38) is satisfied (Malkus & Proctor, 1975). The geostrophic velocity is found in the azimuthal (ϕ) direction in the original Taylor's constraint and fully determines $\boldsymbol{u}$ in this problem. The mathetical interpretation of Taylor's constraint is a solveability condition on the geostrophic flow $V_\phi(s)$ in the spherical problem. We note that due to the nature of the geostrophic cylinders this problem corresponds to an axisymmetric solution. A similar analogy for a solveability condition can be seen in the Cartesian derivation in §3.3.3 where non-axisymmetric solutions are considered.

Not only does the field satisfy equation (3.38) at an initial time but the geostrophic flow must also change such that the field satisfies Taylor's constraint at subsequent times. Unfortuately such solutions hae yet to be found in this scenario. This problem is circumvented by including the small viscous effects from the Ekman boundary layer. In reality, even when small, the viscous term will have some non-zero contribution to the zonal Lorentz torques, leading to the formation of Ekman layers at the cylinder boundary. This leads to a slightly different expression for (3.38) i.e.

$$\int_{C(s)} (\boldsymbol{J}\times\boldsymbol{B})_\phi \,\mathrm{d}s\mathrm{d}z = 4\pi s\frac{V_\phi\,(E_k)^{\frac{1}{2}}}{(1-s^2)^{\frac{1}{4}}}. \tag{3.39}$$

The derivation of (3.39) can be found in the asymptotic analysis of Hollerbach (1996). The difference between equation (3.38) and (3.39) is that (3.38) implicitly defines the geostrophic flow $V_\phi(s)$ due to its nature as a solveability condition whilst (3.39) explicitly defines the geostrophic flow via,

$$V_\phi(s) = E_k^{-\frac{1}{2}}\frac{(1-s^2)^{\frac{1}{4}}}{4\pi s}\int_{C(s)} (\boldsymbol{J}\times\boldsymbol{B})_\phi \,\mathrm{d}s\mathrm{d}z. \tag{3.40}$$

The connection between the spherical and Cartesian geometry for Taylor's constraint as a solveability condition can be seen in the next section. Whilst a non-axisymmetric constraint is also derived; this is somewhat less obvious to conceive given the basis of the axisymmetric coaxial cylinders Taylor's constraint is originally based on.

3.3.2 Soward & Jones (1983) Cartesian Taylor's constraint

Soward & Jones (1983) (and later Abdel-Aziz & Jones (1988)) developed a Cartesian model of flows subject to Taylor's constraint; their Cartesian set up was such that the meridional, azimuthal and radial directions were represented by (x, y, z) respectively, here we stress that their (x, y) coordinates are the opposite way round to our model. A plane layer bound between $z = \pm d$ is considered and the flow is expressed as,

$$\boldsymbol{u} = \nabla \times \psi\,(x,z)\,\hat{\boldsymbol{y}} + u_y\hat{\boldsymbol{y}} \tag{3.41}$$

where u_y contains thermal, magnetic and geostrophic contributions, and the magnetic field is expressed as,

$$\boldsymbol{B} = \nabla \times A\,(x,z)\,\hat{\boldsymbol{y}} + B\,(x,z)\,\hat{\boldsymbol{y}}. \tag{3.42}$$

The equation of motion is

$$2\rho\,(\boldsymbol{\Omega} \times \boldsymbol{u}) = -\nabla\Pi + \boldsymbol{J} \times \boldsymbol{B} + \boldsymbol{F}_A + \boldsymbol{F}_\nu, \tag{3.43}$$

where $\boldsymbol{F}_A$ represents buoyancy forces and $\boldsymbol{F}_\nu$ the viscous terms. The thermal and magnetic contributions are defined such that they balance the buoyancy and magnetic forces respectively. The geostrophic contribution to u_y is determined by taking the y-component of the equation of motion, and integrating over the domain i.e.

$$-2\rho\Omega\int_{-d}^{d}\frac{\partial\psi}{\partial z}\mathrm{d}z = \mu^{-1}\int_{-d}^{d}\frac{\partial\,(A,B)}{\partial\,(x,z)}\mathrm{d}z + \int_{-d}^{d}F_{\nu y}\mathrm{d}z \tag{3.44}$$

For axisymmetric solutions (y-invariant), the resulting geostrophic velocity is in the azimuthal direction. Here a direct comparison to the original Taylor's constraint can be made to the axisymmetric problem; a constraint on the azimuthal component of the Lorentz force relates to an azimuthal geostrophic flow. This basis for the Cartesian version of the Taylor's constraint is considered for our problem.

3.3.3 Cartesian Taylor's constraint for non-axisymmetric solutions

In our Cartesian geometry, (x, y, z) represents the azimuthal, meridional and radial directions respectively. For our system of equations, we take the y-component of (3.20) as we are looking for non-axisymmetric solutions giving,

$$\frac{\partial \psi}{\partial z}=\frac{\partial\left(H,A\right)}{\partial\left(x,z\right)}-\mathrm{B_s}\frac{\partial H}{\partial x}-\frac{1}{\mathrm{Ha}^2}\left(\frac{\partial^2 v}{\partial x^2}+\frac{\partial^2 v}{\partial z^2}\right). \tag{3.45}$$

Equation (3.45) is integrated over the domain z,

$$\psi\left(x,1\right)-\psi\left(x,0\right)=\int_0^1\frac{\partial\left(H,A\right)}{\partial\left(x,z\right)}-\mathrm{B_s}\frac{\partial H}{\partial x}-\frac{1}{\mathrm{Ha}^2}\left(\frac{\partial^2 v}{\partial x^2}+\frac{\partial^2 v}{\partial z^2}\right)\mathrm{d}z. \tag{3.46}$$

From (3.35), we are free to set $\psi\left(x,0\right)=0$ without loss of generality as the constant can be absorbed into $\psi\left(x,1\right)$, as a consequence (3.46) becomes

$$\psi\left(x,1\right)=\int_0^1\frac{\partial\left(H,A\right)}{\partial\left(x,z\right)}-\mathrm{B_s}\frac{\partial H}{\partial x}-\frac{1}{\mathrm{Ha}^2}\left(\frac{\partial^2 v}{\partial x^2}+\frac{\partial^2 v}{\partial z^2}\right)\mathrm{d}z, \tag{3.47}$$

this quantity is to be a constant, however to fully determine the solution we use the fact that the x-derivative should be zero, i.e.

$$\frac{\partial}{\partial x}\psi\left(x,1\right)=\frac{\partial}{\partial x}\int_0^1\frac{\partial\left(H,A\right)}{\partial\left(x,z\right)}-\mathrm{B_s}\frac{\partial H}{\partial x}-\frac{1}{\mathrm{Ha}^2}\left(\frac{\partial^2 v}{\partial x^2}+\frac{\partial^2 v}{\partial z^2}\right)\mathrm{d}z=0. \tag{3.48}$$

This result is analogous to (3.44) which is Taylor's constraint in a Cartesian geometry for axisymmetric solutions. Hence, (3.48) is Taylor's constraint for non-axisymmetric solutions. The geostrophic velocity arises from integrating (3.28) and is determined by satisfying (3.48).

The difference between the two models is the direction in geostrophic velocity. For axisymmetric solutions, the resulting geostrophic velocity is in the azimuthal direction. Here a direct comparison to the original Taylor's constraint can be made to the axisymmetric problem; a constraint on the azimuthal component of the Lorentz force relates to an azimuthal geostrophic flow. Whilst in our non-axisymmetric scenario the geostrophic velocity is in the meridional direction, which a direct comparison to Taylor's constraint is not so obvious.

The final term in (3.48) is analogous to the Ekman boundary layers that form when small viscous effects are included in the spherical problem as seen in equation (3.39). We expect to see boundary layer formation when including small viscous effects.

Taylor's constraint would not be used if we are considering a viscous system with finite Λ, instead we would revert to no slip boundary conditions. We do not consider such a case in this thesis, as all solutions considered are for $\Lambda \to 0$. This simplifies our calculations both in an analytical and numerical scope.

Chapter 4

Asymptotic solutions at small Rm for an inviscid model

In order to make analytical progress with the governing equations, in this chapter we make the additional assumptions that $\mathrm{Rm} \ll 1$ and $\mathrm{B_s} = 0$. It should be pointed out that the regime of $\Lambda \ll 1$, $\mathrm{Rm} \ll 1$ is not that which occurs in planetary interiors; there $\Lambda \sim \mathcal{O}(1)$ and $\mathrm{Rm} \gg 1$. Nonetheless, this regime allows analytical progress, which contributes to our understanding of the general problem. As a result of these assumptions, the governing equations are as follows:

$$\frac{\partial^2 A}{\partial x^2} + \frac{\partial^2 A}{\partial z^2} = \mathrm{Rm} z \frac{\partial A}{\partial x}, \tag{4.1}$$

$$J_y = -z \frac{\partial A}{\partial x}, \tag{4.2}$$

$$\frac{\partial v}{\partial z} = \frac{\partial (J_y, A)}{\partial (x, z)}, \tag{4.3}$$

$$\frac{\partial^2 H}{\partial x^2} + \frac{\partial^2 H}{\partial z^2} = \frac{\partial (v, A)}{\partial (x, z)} + \mathrm{Rm} z \frac{\partial H}{\partial x}, \tag{4.4}$$

$$\frac{\partial \psi}{\partial z} = \frac{\partial (H, A)}{\partial (x, z)}. \tag{4.5}$$

As we are considering $\mathrm{Rm} \ll 1$, the variables A, J_y, v, H and ψ, are expressed as asymptotic series in Rm, namely,

$$A\left(x,z\right) = A_0\left(x,z\right) + \mathrm{Rm}A_1\left(x,z\right) + \mathrm{Rm}^2A_2\left(x,z\right) + \ldots, \tag{4.6}$$

$$J_y\left(x,z\right) = J_{y,0}\left(x,z\right) + \mathrm{Rm}J_{y,1}\left(x,z\right) + \mathrm{Rm}^2J_{y,2}\left(x,z\right) + \ldots, \tag{4.7}$$

$$v\left(x,z\right) = v_0\left(x,z\right) + \mathrm{Rm}v_1\left(x,z\right) + \mathrm{Rm}^2v_2\left(x,z\right) + \ldots, \tag{4.8}$$

$$H\left(x,z\right) = H_0\left(x,z\right) + \mathrm{Rm}H_1\left(x,z\right) + \mathrm{Rm}^2H_2\left(x,z\right) + \ldots, \tag{4.9}$$

$$\psi\left(x,z\right) = \psi_0\left(x,z\right) + \mathrm{Rm}\psi_1\left(x,z\right) + \mathrm{Rm}^2\psi_2\left(x,z\right) + \cdots. \tag{4.10}$$

On substituting (4.6)–(4.10), into (4.1)–(4.5) the leading order equations are

$$\frac{\partial^2 A}{\partial x^2} + \frac{\partial^2 A}{\partial z^2} = 0, \tag{4.11}$$

$$J_y = -z\frac{\partial A}{\partial x}, \tag{4.12}$$

$$\frac{\partial v}{\partial z} = \frac{\partial\left(J_y, A\right)}{\partial\left(x,z\right)}, \tag{4.13}$$

$$\frac{\partial^2 H}{\partial x^2} + \frac{\partial^2 H}{\partial z^2} = \frac{\partial\left(v, A\right)}{\partial\left(x,z\right)}, \tag{4.14}$$

$$\frac{\partial \psi}{\partial z} = \frac{\partial\left(H, A\right)}{\partial\left(x,z\right)}. \tag{4.15}$$

There is a clear order in which to solve these equations: one begins with (4.11) followed by (4.12), (4.13), (4.14) and finally (4.15).

4.1 Leading order solutions

The leading order solution for A satisfies (4.11), subject to the boundary conditions

$$A\left(x,0\right) = \frac{1}{k}\sin\left(kx\right), \tag{4.16}$$

$$\left.\frac{\mathrm{d}A}{\mathrm{d}z}\right|_{z=1} = -kA, \tag{4.17}$$

and has solution,

$$A_0\left(x,z\right) = \frac{1}{k}\sin\left(kx\right)e^{-kz}. \tag{4.18}$$

The solution (4.18) is plotted in figure 4.1; the field emitted at the bottom of the layer is not attenuated entirely at $z = 1$ in the small Rm case; it is also antisymmetric about $x = \pi$.

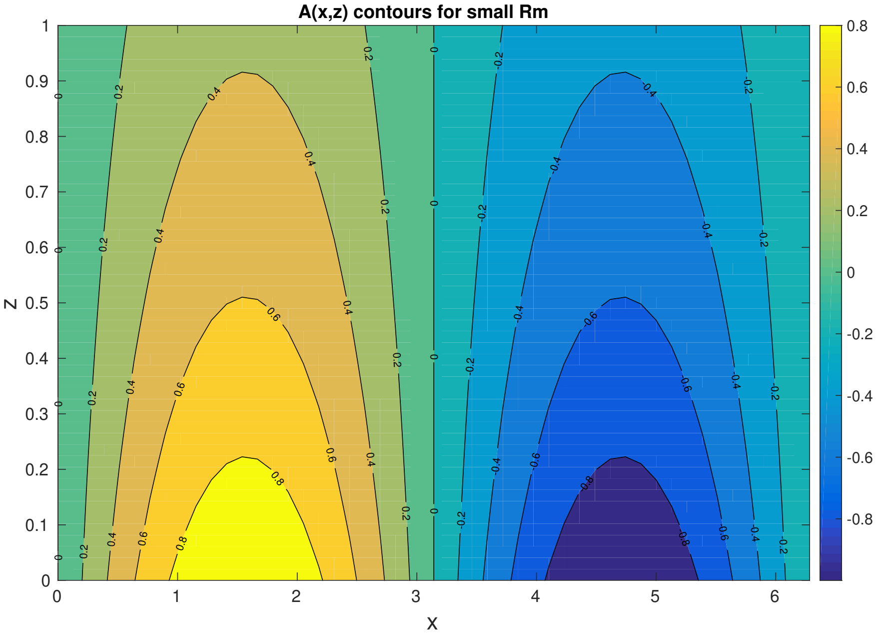

Figure 4.1: Contour plot of $A\left(x,z\right)$ in the small Rm limit for $k=1$.

The leading order solution for the current density is

$$J_{y,0}\left(x,z\right)=-z\cos\left(kx\right)e^{-kz}. \tag{4.19}$$

Substituting into (4.13) and integrating with respect to z gives

$$v_0\left(x,z\right)=-\frac{1}{4k}e^{-2kz}\cos\left(2kx\right)+\frac{1}{2}ze^{-2kz}+V_0\left(x\right), \tag{4.20}$$

where $V_0\left(x\right)$ is the geostrophic flow, i.e. it has only azimuthal structure. The remaining terms in (4.20) contribute to the ageostrophic flow, which has both azimuthal and radial dependence. The geostrophic flow is normally found by satisfying Taylor's constraint (3.38), with the resulting geostrophic velocity found in the azimuthal direction, $V_\phi\left(s\right)$. However, because we are looking at non-axisymmetric solutions which are invariant in y, the geostrophic velocity here is in the meridional direction y, and not the azimuthal direction x. Owing to our choice of geometry, Taylor's constraint itself is slightly different in this analysis. To determine the geostrophic flow in this geometry requires us to use the boundary condition for $\psi\left(x,z\right)$ at the top of the layer.

The ageostrophic component of (4.20) is plotted in figure 4.2. There is symmetry about $x = \pi$ and the strength of the velocity is much greater in the lower half of the domain. At this stage, we are yet to determine the solution of the geostrophic part $V_0(x)$; this will be determined by our ψ boundary condition at $z = 1$. Expression (4.20) is substituted directly into equation (4.14), giving the leading order PDE

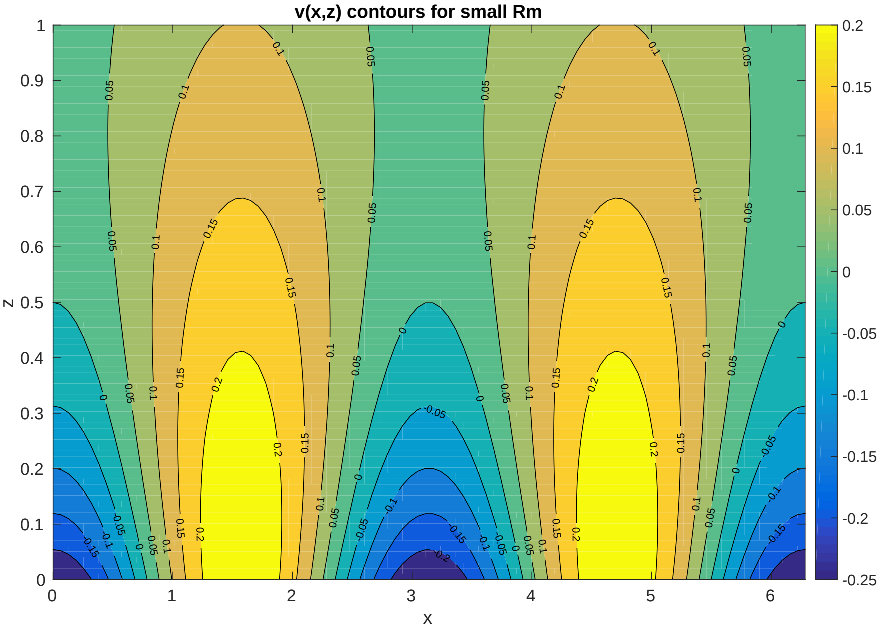

Figure 4.2: Contour plot of the ageostrophic part of $v(x,z)$ in the small Rm limit for $k = 1$.

$$\left(\frac{\partial^2}{\partial x^2} + \frac{\partial^2}{\partial z^2}\right) H_0(x,z) = ke^{-3kz}\left(z - \frac{1}{k}\right)\cos(kx) - e^{-kz}V_0'(x)\sin(kx)\,. \quad (4.21)$$

We write

$$H_0(x,z) = H^a(x,z) + H^g(x,z)\,. \quad (4.22)$$

where $H^a(x,z)$ and $H^g(x,z)$ are the ageostrophic and geostrophic parts respectively. The geostrophic part, $H^g(x,z)$, is such that it is dependent solely on the contribution from the geostrophic flow $V_0'(x)$, and the ageostrophic part, $H^a(x,z)$, the contrary. By expressing $H_0(x,z)$ in the form (4.22), equation (4.21) can be separated into an ODE for $H^a(x,z)$ and a PDE for $H^g(x,z)$. The ageostrophic part already has its

x-dependence determined via balancing the ageostrophic part of (4.21), i.e.

$$H^{a}\left(x,z\right)=h_{a}\left(z\right)\cos\left(kx\right), \tag{4.23}$$

where $h_a\left(z\right)$ obeys the second order ODE

$$\frac{\mathrm{d}^{2}h_{a}}{\mathrm{d}z^{2}}-k^{2}h_{a}=k\left(z-\frac{1}{k}\right)e^{-3kz}, \tag{4.24}$$

subject to the boundary conditions $h_a\left(0\right)=h_a\left(1\right)=0$. The geostrophic part, $H^g\left(x,z\right)$, then obeys the PDE

$$\frac{\partial^{2}H^{g}}{\partial x^{2}}+\frac{\partial^{2}H^{g}}{\partial z^{2}}=-e^{-kz}V_{0}'\left(x\right)\sin\left(kx\right). \tag{4.25}$$

The solution to (4.24) is

$$h_{a}\left(z\right)=\alpha_{0}\sinh\left(kz\right)+\alpha_{1}\cosh\left(kz\right)+\frac{1}{8k}\left(z-\frac{1}{4k}\right)e^{-3kz}, \tag{4.26}$$

where

$$\alpha_{0}=\frac{1}{8k^{2}\sinh\left(k\right)}\left[k\left(\frac{1}{4k}-1\right)e^{-3k}-\frac{1}{4}\cosh\left(k\right)\right], \tag{4.27}$$

$$\alpha_{1}=\frac{1}{32k^{2}}. \tag{4.28}$$

On substituting (4.18) and (4.22) into (4.15), and making use of (4.23), we obtain

$$\begin{aligned}\frac{\partial\psi_{0}}{\partial z}=&-\frac{1}{2}\cos\left(2kx\right)\left[\frac{\mathrm{d}}{\mathrm{d}z}\left(h_{a}e^{-kz}\right)+2ke^{-kz}h_{a}\right]\\&-\frac{1}{2}\frac{\mathrm{d}}{\mathrm{d}z}\left(h_{a}e^{-kz}\right)-e^{-kz}\left[\cos\left(kx\right)\frac{\partial H^{g}}{\partial z}+\sin\left(kx\right)\frac{\partial H^{g}}{\partial x}\right].\end{aligned} \tag{4.29}$$

Equation (4.29) is integrated over the domain, noting that the bottom boundary condition gives $\psi\left(x,0\right)=0$, to give the the following expression,

$$\begin{aligned}\psi_{0}\left(x,1\right)=&-k\cos\left(2kx\right)\int_{0}^{1}h_{a}\left(z\right)e^{-kz}\mathrm{d}z\\&-\int_{0}^{1}e^{-kz}\left(\cos\left(kx\right)\frac{\partial H^{g}}{\partial z}+\sin\left(kx\right)\frac{\partial H^{g}}{\partial x}\right)\mathrm{d}z.\end{aligned} \tag{4.30}$$

Assuming $H^g\left(x,z\right)$ is of the separable form $H^g\left(x,z\right)=\mathcal{F}_1\left(x\right)\mathcal{G}_1\left(z\right)$, equation (4.30) can be expressed in the form

$$\alpha\sin\left(kx\right)\frac{\mathrm{d}\mathcal{F}_{1}}{\mathrm{d}x}+\beta\cos\left(kx\right)\mathcal{F}_{1}=\gamma\cos\left(2kx\right), \tag{4.31}$$

where

$$\alpha = \int_0^1 e^{-kz} \mathcal{G}_1(z)\,\mathrm{d}z, \tag{4.32}$$

$$\beta = \int_0^1 e^{-kz} \mathcal{G}_1'(z)\,\mathrm{d}z = k\int_0^1 e^{-kz} \mathcal{G}_1(z)\,\mathrm{d}z = k\alpha. \tag{4.33}$$

The left hand side of (4.31) can be expressed as a perfect derivative and can be solved via an integrating factor, I_f, with

$$I_f = \sin(kx)^{\frac{\beta}{\alpha k}} = \sin(kx). \tag{4.34}$$

Hence

$$\mathcal{F}_1(x) = \frac{\gamma}{2k\alpha}\frac{\sin(2kx)}{\sin(kx)} = \frac{\gamma}{k\alpha}\cos(kx). \tag{4.35}$$

Equation (4.35) indicates that $H^g(x,z)$ takes the form

$$H^g(x,z) = h_g(z)\cos(kx), \tag{4.36}$$

where $h_g(z)$ is to be determined. Substituting (4.36) back into (4.25) gives

$$\frac{\mathrm{d}^2 h_g}{\mathrm{d}z^2} - k^2 h_g = -e^{-kz} V_0'(x)\frac{\sin(kx)}{\cos(kx)}. \tag{4.37}$$

Equation (4.37) can be reduced to an ODE in z provided that we choose

$$V_0'(x) = \widetilde{\mathrm{V}}_0 k\cot(kx). \tag{4.38}$$

The x-dependence of the geostrophic flow has now been determined. In order to determine its amplitude $\widetilde{\mathrm{V}}_0$ we need to apply the condition

$$\frac{\partial}{\partial x}\psi(x,1) = 0. \tag{4.39}$$

This is possible once we have the full solution to $H_1(x,z)$. With the choice (4.38) of $V_0'(x)$, we see that $h_g(z)$ satisfies the second order ODE

$$\frac{\mathrm{d}^2 h_g}{\mathrm{d}z^2} - k^2 h_g = -\widetilde{\mathrm{V}}_0 k e^{-kz}. \tag{4.40}$$

Equation (4.40) is subject to the boundary conditions $h_g(0) = h_g(1) = 0$. This has solution

$$h_g(z) = \frac{\widetilde{\mathrm{V}}_0}{2}\left[z e^{-kz} - \frac{\sinh(kz)\,e^{-k}}{\sinh(k)}\right]. \tag{4.41}$$

Hence from (4.26) and (4.41),

$$\begin{aligned}H_0\left(x,z\right) =& \cos\left(kx\right)\left[\left(\alpha_0\sinh\left(kz\right)+\alpha_1\cosh\left(kz\right)+\frac{1}{8k}\left(z-\frac{1}{4k}\right)e^{-3kz}\right)\right.\\ &\left.+\frac{\widetilde{\mathrm{V}}_0}{2}\left(ze^{-kz}-\frac{\sinh\left(kz\right)e^{-k}}{\sinh\left(k\right)}\right)\right]. \end{aligned} \tag{4.42}$$

The final steps are to determine $\widetilde{\mathrm{V}}_0$, thus leading to a complete expression for the geostrophic flow and then determining $\psi\left(x,z\right)$. $\widetilde{\mathrm{V}}_0$ is evaluated using the top boundary condition for the stream function,

$$\frac{\partial}{\partial x}\psi\left(x,1\right)=\frac{\partial}{\partial x}\int_0^1\frac{\partial\left(H,A\right)}{\partial\left(x,z\right)}\mathrm{d}z=0. \tag{4.43}$$

On introducing the notation, $H_0\left(x,z\right)=\hat{h}\left(z\right)\cos\left(kx\right)$, (4.43) becomes

$$\begin{aligned}\frac{\partial}{\partial x}\psi_1\left(x,1\right)=&-\frac{1}{2}\frac{\partial}{\partial x}\int_0^1\frac{\mathrm{d}}{\mathrm{d}z}\left(\hat{h}e^{-kz}\right)\mathrm{d}z\\ &-\frac{\partial}{\partial x}\cos\left(2kx\right)\int_0^1\left[\frac{1}{2}\frac{\mathrm{d}}{\mathrm{d}z}\left(\hat{h}e^{-kz}\right)+k\hat{h}e^{-kz}\right]\mathrm{d}z=0.\end{aligned} \tag{4.44}$$

At the top and bottom boundaries, $H\left(x,z\right)$ is subject to (3.34), i.e.

$$\hat{h}\left(0\right)=\hat{h}\left(1\right)=0 \tag{4.45}$$

at $z=0,1$, thus simplifying the evaluation of (4.44). We are now left with just one term to evaluate, which will determine the coefficient of $V_0\left(x\right)$. Equation (4.44) becomes

$$\int_0^1\hat{h}\left(z\right)e^{-kz}\mathrm{d}z=0, \tag{4.46}$$

which will determine $\widetilde{\mathrm{V}}_0$ which is contained within the function $\hat{h}\left(z\right)$ and as a result will satisfy (4.43). Equation (4.46) is

$$\begin{aligned}&\frac{\widetilde{\mathrm{V}}_0}{2}\int_0^1 ze^{-2kz}-\frac{\sinh\left(kz\right)e^{-k}e^{-kz}}{\sinh\left(k\right)}\mathrm{d}z\\ &\quad=-\int_0^1\alpha_0e^{-kz}\sinh\left(kz\right)+\alpha_1e^{-kz}\cosh\left(kz\right)+\frac{1}{8k}\left(z-\frac{1}{4k}\right)e^{-4kz}\mathrm{d}z;\end{aligned} \tag{4.47}$$

after some algebraic manipulation, we derive the following expression for $\widetilde{\mathrm{V}}_0$,

$$\begin{aligned}\widetilde{\mathrm{V}}_0=&-\left\{-\frac{e^{-2k}}{2k}\left(1+\frac{1}{2k}\right)+\frac{1}{4k^2}-\frac{e^{-k}}{\sinh\left(k\right)}\left(\frac{e^{-2k}}{4k}+\frac{1}{2}-\frac{1}{4k}\right)\right\}^{-1}\\ &\times\left\{\alpha_0\left(\frac{1}{2k}\left(e^{-2k}-1\right)+1\right)+\alpha_1\left(1+\frac{1}{2k}\left(1-e^{-2k}\right)\right)-\frac{ke^{-4k}}{16}\right\}.\end{aligned} \tag{4.48}$$

We note that $\widetilde{\mathrm{V}}_0 = -0.302913$ when $k = 1$. The stream function $\psi\left(x, z\right)$ is

$$\begin{aligned}\psi_0\left(x, z\right) = &-\frac{1}{2}\int_0^z \frac{\mathrm{d}}{\mathrm{d}z'}\left(\hat{h}\left(z'\right)e^{-kz'}\right)\mathrm{d}z' \\ &-\cos\left(2kx\right)\int_0^z \frac{1}{2}\frac{\mathrm{d}}{\mathrm{d}z'}\left(\hat{h}\left(z'\right)e^{-kz'}\right) + k\hat{h}\left(z'\right)e^{-kz'}\mathrm{d}z',\end{aligned} \tag{4.49}$$

i.e.,

$$\begin{aligned}\psi_0\left(x, z\right) = &-\frac{1}{2}\left\{e^{-kz}\left[\alpha_0\sinh\left(kz\right) + \alpha_1\cosh\left(kz\right) + \frac{1}{8k}\left(z - \frac{1}{4k}\right)e^{-3kz}\right.\right. \\ &\left.\left.+\frac{\widetilde{\mathrm{V}}_0}{2}\left(ze^{-kz} - \frac{\sinh\left(kz\right)e^{-k}}{\sinh\left(k\right)}\right)\right]\right\} \\ &-\frac{k}{2}\cos\left(2kx\right)\left\{e^{-kz}\left[\alpha_0\sinh\left(kz\right) + \alpha_1\cosh\left(kz\right) + \frac{1}{8k}\left(z - \frac{1}{4k}\right)e^{-3kz}\right.\right. \\ &\left.+\frac{\widetilde{\mathrm{V}}_0}{2}\left(ze^{-kz} - \frac{\sinh\left(kz\right)e^{-k}}{\sinh\left(k\right)}\right)\right] \\ &+\alpha_0\left(\frac{e^{-2kz}}{2k} + z - \frac{1}{2k}\right) + \alpha_1\left(z - \frac{e^{-2kz}}{2k} + \frac{1}{2k}\right) - \frac{1}{16k^2}ze^{-4kz} \\ &\left.+\widetilde{\mathrm{V}}_0\left[\frac{1}{4k^2} - \frac{e^{-2kz}}{2k}\left(z + \frac{1}{2k}\right) + \frac{e^{-k}}{\sinh\left(k\right)}\left(\frac{1}{4k} - \frac{e^{-2kz}}{4k} - \frac{z}{2}\right)\right]\right\}.\end{aligned} \tag{4.50}$$

This completes the solution to the system of equations at $\mathcal{O}\left(\mathrm{Rm}\right)$.

The meridional field $H\left(x, z\right)$, given by (4.42), is plotted in figure 4.3. The meridional field is also symmetric about $x = \pi$ and has maximum amplitude of 4×10^{-3}.

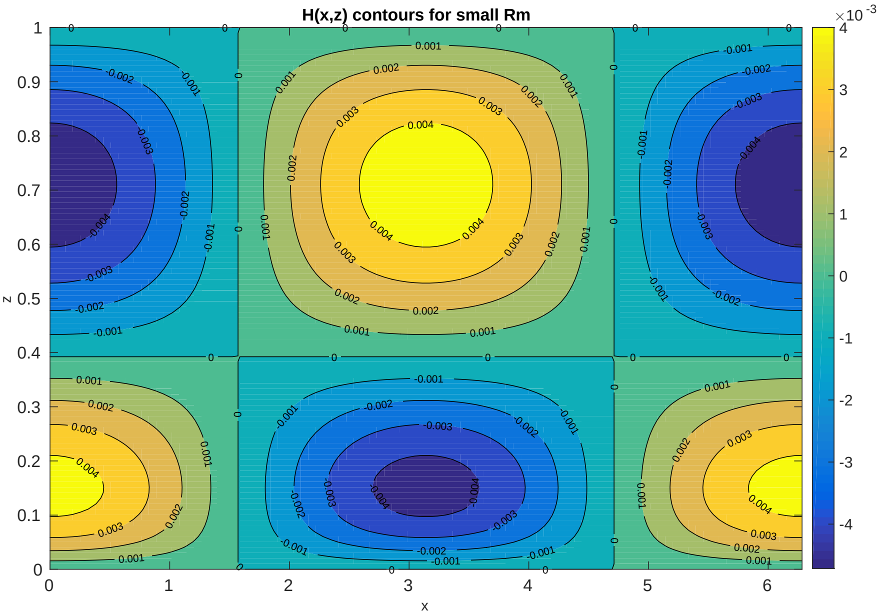

Figure 4.3: Contour plot of $H\left(x,z\right)$ in the small Rm limit for $k=1$.

The stream function ψ is plotted in figure 4.4; ψ takes the form of cellular-like patterns and is symmetric about $x=\pi$ with maximum amplitude of 4×10^{-3}.

The individual harmonics of $\psi\left(x,z\right)$ are plotted in figure 4.5. The harmonic $\psi^{(0)}\left(x,z\right)$ corresponds to the purely z part of $\psi\left(x,z\right)$,

$$\begin{aligned}\psi^{(0)}\left(x,z\right)=-\frac{1}{2}e^{-kz}&\left[\alpha_0\sinh\left(kz\right)+\alpha_1\cosh\left(kz\right)+\frac{1}{8k}\left(z-\frac{1}{4k}\right)e^{-3kz}\right.\\&\left.+\frac{\widetilde{\mathrm{V}}_0}{2}\left(ze^{-kz}-\frac{\sinh\left(kz\right)e^{-k}}{\sinh\left(k\right)}\right)\right],\end{aligned}\tag{4.51}$$

and $\psi^{(2)}\left(x,z\right)$ corresponds to the $\cos\left(2kx\right)$ part,

$$\begin{aligned}\psi^{(2)}\left(x,z\right)=-\frac{k}{2}\Bigg\{&e^{-kz}\left[\alpha_0\sinh\left(kz\right)+\alpha_1\cosh\left(kz\right)+\frac{1}{8k}\left(z-\frac{1}{4k}\right)e^{-3kz}\right.\\&\left.+\frac{\widetilde{\mathrm{V}}_0}{2}\left(ze^{-kz}-\frac{\sinh\left(kz\right)e^{-k}}{\sinh\left(k\right)}\right)\right]\\&+\alpha_0\left(\frac{e^{-2kz}}{2k}+z-\frac{1}{2k}\right)+\alpha_1\left(z-\frac{e^{-2kz}}{2k}+\frac{1}{2k}\right)-\frac{1}{16k^2}ze^{-4kz}\\&+\widetilde{\mathrm{V}}_0\left[\frac{1}{4k^2}-\frac{e^{-2kz}}{2k}\left(z+\frac{1}{2k}\right)+\frac{e^{-k}}{\sinh\left(k\right)}\left(\frac{1}{4k}-\frac{e^{-2kz}}{4k}-\frac{z}{2}\right)\right]\Bigg\}.\end{aligned}\tag{4.52}$$

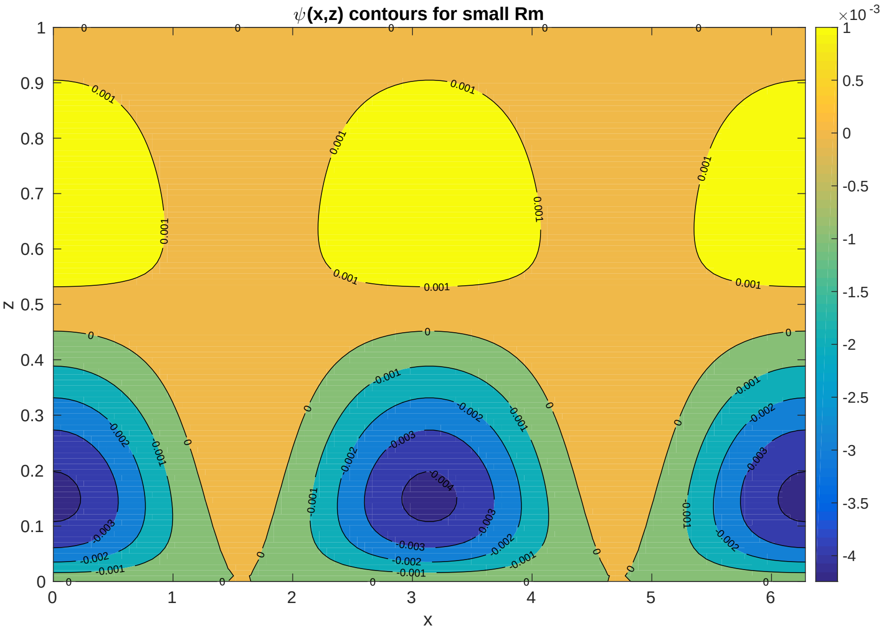

Figure 4.4: Contour plot of the stream function $\psi\left(x,z\right)$ in the small Rm limit for $k=1$.

Both satisfy the boundary conditions at $z=0,1$.

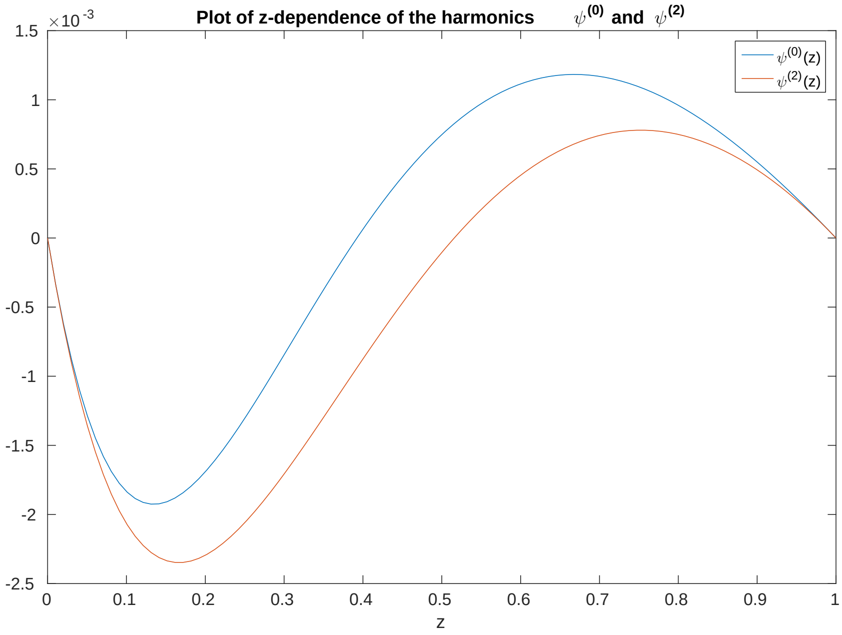

Figure 4.5: A plot of the stream function harmonics $\psi^{(0)}\left(z\right)$ and $\psi^{(2)}\left(z\right)$ in the small Rm limit for $k=1$.

Integrating (4.38) with respect to x gives,

$$V_0(x) = \widetilde{\mathrm{V}}_0 \log(\sin(kx)). \tag{4.53}$$

$V_0(x)$ goes to infinity as $x \to 0$ and $x \to \pi$. In figure 4.6, $V_0'(x)$ is plotted to show this singular behaviour near these points. Of course, this property is physically unrealistic as such velocities cannot exist. The reason for this singular behaviour stems from the generation of the meridional magnetic field $H(x, z)$ which is generated from the magnetic stretching of the potential field $A(x, z)$ by the meridional circulation $v(x, z)$. Magnetic stretching is described by the term

$$(\boldsymbol{B} \cdot \nabla) u_y = \frac{\partial A}{\partial x}\frac{\partial v}{\partial z} - \frac{\partial A}{\partial z}\frac{\partial v}{\partial x}, \tag{4.54}$$

and the geostrophic contribution to magnetic stretching arises from $V_0(x)$ acting on the azimuthal field $B_x = \frac{\partial A}{\partial x}$. Since the horizontal field is zero at $x = 0$, there is no field to stretch out into the y-direction at $x = 0$. In order to get a non-zero effect from $B_x \frac{\mathrm{d}V_0}{\mathrm{d}x}$ at $x = 0$, we require an infinite $\frac{\mathrm{d}V_0}{\mathrm{d}x}$ to counter the lack of B_x there, whence this singularity occurs.

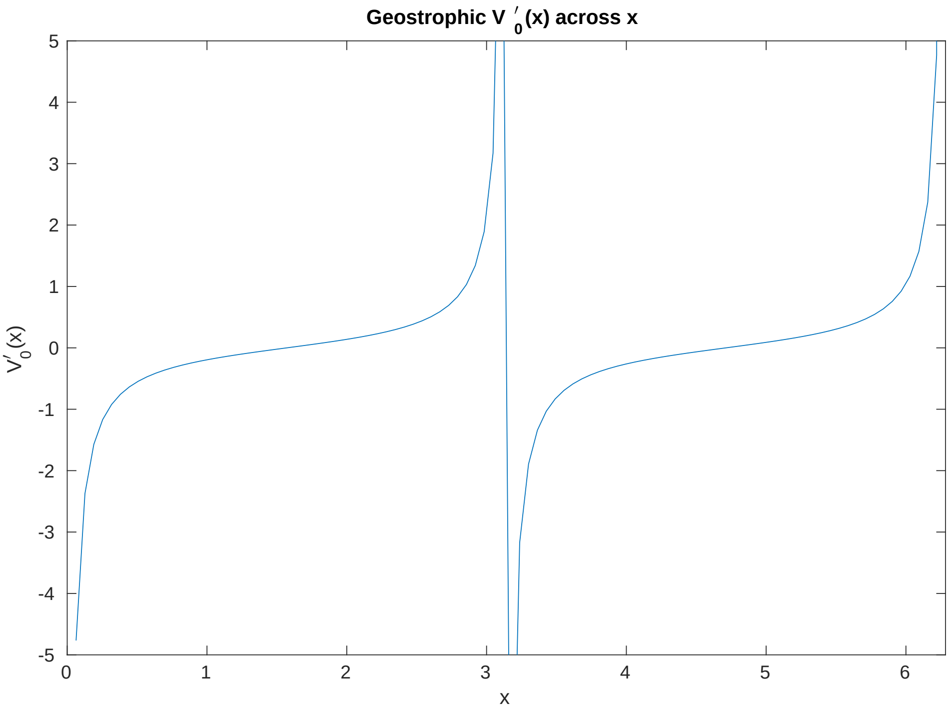

Figure 4.6: A plot of the geostrophic flow in the small Rm limit for $k = 1$.

Chapter 5

Numerical method for general Rm and Ha

In general, for finite values of Rm and Ha, equations (3.26)–(3.30) require a numerical solution. In this chapter an overview of the methodology is discussed for solving the equations for a general Rm-Ha system.

The asymptotic solutions found for small Rm can be used to test whether the code is working correctly. Of course, a slightly different approach has to be made in the inviscid regime where the geostrophic flow is singular – this causes difficulties when trying to directly evaluate $V_0'(x)$ numerically. A comparison between the two methods is given.

5.1 Method of solution

The numerical approach to solving (3.26)–(3.30) is somewhat unconventional compared to standard methods. As we are dealing with what is essentially a constraint on the geostrophic flow, we require a root finding algorithm to be implemented into the numerical code. The PDEs that are to be solved are

$$\frac{\partial^2 A}{\partial x^2}+\frac{\partial^2 A}{\partial z^2}=\mathrm{Rm}z\frac{\partial A}{\partial x}, \tag{5.1}$$

$$J_y=-z\frac{\partial A}{\partial x}, \tag{5.2}$$

$$\frac{\partial v}{\partial z}=\frac{\partial\left(J_y,A\right)}{\partial\left(x,z\right)}-\mathrm{B_s}\frac{\partial J_y}{\partial x}, \tag{5.3}$$

$$\frac{\partial^2 H}{\partial x^2}+\frac{\partial^2 H}{\partial z^2}=\frac{\partial\left(v,A\right)}{\partial\left(x,z\right)}+\mathrm{Rm}z\frac{\partial H}{\partial x}-\mathrm{B_s}\frac{\partial v}{\partial x}, \tag{5.4}$$

$$\frac{\partial \psi}{\partial z}=\frac{\partial\left(H,A\right)}{\partial\left(x,z\right)}-\mathrm{B_s}\frac{\partial H}{\partial x}-\frac{1}{\mathrm{Ha}^2}\left(\frac{\partial^2 v}{\partial x^2}+\frac{\partial^2 v}{\partial z^2}\right). \tag{5.5}$$

The solution to (5.1) at finite Rm is the Hankel function solution found earlier in Chapter 2. We express the solution to (5.1) as

$$A\left(x,z\right)=-\frac{i}{2}\left(f\left(z\right)e^{ikx}-\bar{f}\left(z\right)e^{-ikx}\right), \tag{5.6}$$

where $f\left(z\right)$ is the Hankel function solution (2.18). We shall leave the solutions in terms of $f\left(z\right)$. The choice of the prefactor $\frac{i}{2}$ is to ensure that in the low Rm limit, $A\left(x,z\right)$ takes the form,

$$A\left(x,z\right)=A\left(z\right)\sin\left(kx\right). \tag{5.7}$$

We can find $A\left(x,z\right)$ by solving for the harmonics e^{ikx} and e^{-ikx}. By considering the e^{ikx} harmonic, the corresponding second order ODE for $f\left(z\right)$ is

$$\frac{\mathrm{d}^2 f}{\mathrm{d}z^2}=k^2 f+ik\mathrm{Rm}zf, \tag{5.8}$$

where the boundary conditions (3.31) and (3.33) are applied, i.e.

$$f\left(0\right)=\frac{1}{k}, \tag{5.9}$$

$$f'\left(1\right)=-kf\left(1\right). \tag{5.10}$$

The conjugate solution, $\bar{f}\left(z\right)$, is the solution to (5.8) but with $-i$ in the final term. Equation (5.8) with the boundary conditions (5.9), (5.10) is then solved by using the inbuilt MATLAB function `bvp4c`; this integrates a system of ODEs over a given interval when subject to two boundary conditions, using a finite difference code in order to integrate the ODEs.

The current density, J_y, is expressed in terms of $f(z)$ as

$$J_y = -\frac{k}{2} z \left(f(z) e^{ikx} + \bar{f}(z) e^{-ikx} \right). \tag{5.11}$$

On substitution of (5.6) and (5.11) into (5.3), $v(x,z)$ takes the form,

$$v(x,z) = v_0(z) + v_1(z) e^{ikx} + \bar{v}_1(z) e^{-ikx} + v_2(z) e^{2ikx} + \bar{v}_2(z) e^{-2ikx} + V_0(x), \tag{5.12}$$

where each of the harmonics in the ageostrophic solution is governed by the ODEs:

$$\frac{\mathrm{d}v_0}{\mathrm{d}z} = \frac{k^2}{2} \left[z f' \bar{f} + z f \bar{f}' + f \bar{f} \right], \tag{5.13}$$

$$\frac{\mathrm{d}v_1}{\mathrm{d}z} = \frac{ik^2 \mathrm{B}_s z}{2} f, \tag{5.14}$$

$$\frac{\mathrm{d}v_2}{\mathrm{d}z} = \frac{k^2}{4} f^2. \tag{5.15}$$

The solution f is carried throughout the numerical routine, meaning that we only need to solve for f once and, as a result, this solution is then used for each of the harmonics in $v(x,z)$. It is important to note that in the theory, and from equation (5.3), there are no boundary conditions explicitly applied to $v(x,z)$, but we add in a geostrophic flow term $V_0(x)$, which is subsequently determined by Taylor's constraint. In the numerical code we must however provide a boundary condition to solve equations (5.13)- (5.15). The choice of boundary conditions will change the solutions to (5.13)-(5.15) individually, but when we apply Taylor's constraint, $V_0(x)$ adjusts so that whichever boundary condition is used, a unique solution (up to a constant) for $v(x,z)$ is obtained for the sum of the ageostrophic and geostrophic components. Therefore it is important to stress that the choice of boundary condition is arbitrary. We solve equations (5.13)- (5.15) using `bvp4c` and set $v(x,z) = 0$ at $z = 0$. A comparison is provided later which shows that changing the boundary condition does not change the overall solution.

The geostrophic velocity, $V_0(x)$, is still to be determined in this problem. The derivative to the geostrophic velocity is the only explicit term throughout the system of equations and it is expressed as a Fourier series in x in order to satisfy periodicity. We write

$$V_0'(x) = \sum_{n=1}^{N} (u_n + iv_n) e^{inkx} + \text{c.c.}, \tag{5.16}$$

where u_n and v_n are purely real and N is the number of modes. Here N is chosen to be large enough so that the omitted terms in the Fourier expansion are numerically small, but not so large that the amount of computation becomes impractically large. Substituting the expressions (5.12) and (5.6) into equation (5.4) gives the following PDE,

$$\begin{aligned}\nabla^2 H - \mathrm{Rm} z\frac{\partial H}{\partial x} =& \frac{\mathrm{d}V_0}{\mathrm{d}x}\left(\frac{i}{2}\bar{f}'e^{-ikx} - \frac{i}{2}f'e^{ikx} - \mathrm{B}_s\right) \\ & - \frac{k}{2}\left(f\bar{v}_1' + \bar{f}v_1' + f'\bar{v}_1 + \bar{f}'v_1\right) \\ & + ke^{3ikx}\left[f'v_2 - \frac{1}{2}fv_2'\right] \\ & - ke^{2ikx}\left[2i\mathrm{B}_s v_2 + \frac{1}{2}fv_1' - \frac{1}{2}f'v_1\right] \\ & - ke^{ikx}\left[i\mathrm{B}_s v_1 + \bar{f}'v_2 + \frac{1}{2}fv_0' + \frac{1}{2}\bar{f}v_2'\right] + \text{c.c.} \end{aligned} \tag{5.17}$$

By expressing $H(x,z)$ as

$$\begin{aligned}H(x,z) =& h_0(z) + h_1(z)e^{ikx} + \bar{h}_1(z)e^{-ikx} + h_2(z)e^{2ikx} + \bar{h}_2(z)e^{-2ikx} \\ & + h_3(z)e^{3ikx} + \bar{h}_3(z)e^{-3ikx} + h_g(x,z), \end{aligned} \tag{5.18}$$

equation (5.17) can then be separated into seven linear ODEs and one PDE. $h_g(x,z)$ represents the geostrophic part of the meridional field. The PDE and the four non-conjugate ODEs are

$$\frac{\mathrm{d}^2 h_0}{\mathrm{d}z^2} = -\frac{k}{2}\left(f\bar{v}_1' + \bar{f}v_1' + f'\bar{v}_1 + \bar{f}'v_1\right), \tag{5.19}$$

$$\frac{\mathrm{d}^2 h_1}{\mathrm{d}z^2} - k^2 h_1 - ik\mathrm{Rm} z h_1 = -k\left(i\mathrm{B}_s v_1 + \bar{f}'v_2 + \frac{1}{2}fv_0' + \frac{1}{2}\bar{f}v_2'\right), \tag{5.20}$$

$$\frac{\mathrm{d}^2 h_2}{\mathrm{d}z^2} - 4k^2 h_2 - 2ik\mathrm{Rm} z h_2 = -k\left(2i\mathrm{B}_s v_2 + \frac{1}{2}fv_1' - \frac{1}{2}f'v_1\right), \tag{5.21}$$

$$\frac{\mathrm{d}^2 h_3}{\mathrm{d}z^2} - 9k^2 h_3 - 3ik\mathrm{Rm} z h_3 = k\left(f'v_2 - \frac{1}{2}fv_2'\right), \tag{5.22}$$

$$\frac{\partial^2 h_g}{\partial z^2} + \frac{\partial^2 h_g}{\partial x^2} - \mathrm{Rm} z\frac{\partial h}{\partial x} = \frac{\mathrm{d}V_0}{\mathrm{d}x}\left(\frac{i}{2}\bar{f}'e^{-ikx} - \frac{i}{2}f'e^{ikx} - \mathrm{B}_s\right), \tag{5.23}$$

the three corresponding conjugate ODEs for (5.20) (5.21) and (5.22) complete the set of ODEs/PDE for (5.18). The ODE for $h_0(z)$ arises only in the non-zero horizontal field case. The solution to equations (5.19)-(5.22) provide the ageostrophic contributions to $H(x,z)$ and are subject to

$$h_n(0) = 0, \tag{5.24}$$

$$h_n(1) = 0, \tag{5.25}$$

for $n = 0 \ldots 3$. The boundary conditions (5.24) and (5.25) correspond to the magnetic boundary condition (3.34). Using (5.16), equation (5.23) will reduce to a system of ODEs in z, which can then be solved for each harmonic in x. Equation (5.23) becomes

$$\begin{aligned}\mathcal{L}(h_g) =& \frac{i}{2}\left[\sum_{n=1}^{N}(u_n+iv_n)\bar{f}'e^{ik(n-1)x} - (u_n+iv_n)f'e^{ik(n+1)x} + \text{c.c.}\right]\\ &- \mathrm{B}_s\left[\sum_{n=1}^{N}(u_n+iv_n)e^{inkx} + \text{c.c}\right],\end{aligned} \tag{5.26}$$

where $\mathcal{L}$ denotes the linear operator acting on the left hand side of (5.23). It is apparent that the geostrophic meridional field, $h_g(x,z)$, takes the form of a Fourier series in x with unknown functions of z as its coefficients. We may then express $h_g(x,z)$ as

$$h_g(x,z) = \frac{1}{2}q_0(z) + \sum_{n=1}^{N+1} q_n(z)e^{inkx} + \text{c.c.}, \tag{5.27}$$

where the coefficients $q_n(z)$ satisfy the following ODEs,

$$q_0'' = i\left[(u_1+iv_1)\bar{f}' - (u_1-iv_1)f'\right], \tag{5.28}$$

$$q_1'' - k^2q_1 - ik\mathrm{Rm}zq_1 = \frac{i}{2}(u_2+iv_2)\bar{f}' - \mathrm{B}_s(u_1+iv_1), \tag{5.29}$$

$$\begin{aligned}q_n'' - n^2k^2q_n - ink\mathrm{Rm}zq_n =& \frac{i}{2}\left[(u_{n+1}+iv_{n+1})\bar{f}'\right.\\ &\left.-(u_{n-1}+iv_{n-1})f'\right] - \mathrm{B}_s(u_n+iv_n),\end{aligned} \tag{5.30}$$

$$q_N'' - N^2k^2q_N - iNk\mathrm{Rm}zq_N = -\frac{i}{2}(u_{N-1}+iv_{N-1})f' - \mathrm{B}_s(u_N+iv_N), \tag{5.31}$$

$$q_{N+1}'' - (N+1)^2k^2q_{N+1} - i(N+1)k\mathrm{Rm}zq_{N+1} = -\frac{i}{2}(u_N+iv_N)f', \tag{5.32}$$

and are subject to the boundary conditions

$$q_n(0) = 0, \tag{5.33}$$

$$q_n(1) = 0, \tag{5.34}$$

for $n = 0 \ldots N+1$.

Finally, the stream function is evaluated by substitution of (5.6), (5.18) and (5.27) into (5.5), giving

$$\begin{aligned}
\frac{\partial \psi}{\partial z} = &-\frac{k}{2}\left[h_1\bar{f}' + h_1'\bar{f} + \bar{h}_1 f' + \bar{h}_1' f\right] - \frac{k}{2}\left[2h_2\bar{f}' + h_2'\bar{f} + \frac{1}{2}fq_0' + h_0' f + 2i\mathrm{B}_s h_1\right]e^{ikx} \\
&+ \frac{k}{2}\left[h_1 f' - 3h_3\bar{f}' - h_1' f - h_3'\bar{f} - 4i\mathrm{B}_s h_2\right]e^{2ikx} + \frac{k}{2}\left[2h_2 f' - h_2' f - 6i\mathrm{B}_s h_3\right]e^{3ikx} \\
&+ \frac{k}{2}\left[3h_3 f - h_3' f\right]e^{4ikx} + \frac{k}{2}\left(f'e^{ikx} - \bar{f}'e^{-ikx}\right)\left(\sum_{n=1}^{N+1} nq_n e^{inkx} + \text{c.c.}\right) \\
&- \frac{k}{2}\left(fe^{ikx} + \bar{f}e^{-ikx}\right)\left(\sum_{n=1}^{N+1} q_n' e^{inkx} + \text{c.c.}\right) - ik\mathrm{B}_\mathrm{s}\sum_{n=1}^{N} nq_n e^{inkx} + \text{c.c.} \\
&+ \frac{1}{\mathrm{Ha}^2}\left[v_0'' + \left(v_2'' - 4k^2 v_2\right)e^{2ikx} + \left(\bar{v}_2'' - 4k^2\bar{v}_2\right)e^{-2ikx}\right] \\
&+ \frac{1}{\mathrm{Ha}^2}\sum_{n=1}^{N}\left(ikn\left(u_n + iv_n\right)e^{inkx} + \text{c.c.}\right). \qquad (5.35)
\end{aligned}$$

By letting

$$\psi\left(x,z\right) = \frac{1}{2}\psi_0\left(z\right) + \sum_{n=1}^{N+2}\psi_n\left(z\right)e^{inkx} + \text{c.c.}, \qquad (5.36)$$

equation (5.35) can be then split into $2N+1$ first order ODEs, which includes the conjugate ODEs.

We then solve for the harmonics $n = 0 \dots N$,

$$
\begin{aligned}
\frac{\mathrm{d}\psi_0}{\mathrm{d}z} =& -\frac{k}{2}\left[h_1\bar{f}' + h_1'\bar{f} + \bar{h}_1 f' + \bar{h}_1' f + q_1\bar{f}' + \bar{q}_1 f' + \bar{q}_1' f + q_1'\bar{f}\right] \\
& - \frac{k^2}{\mathrm{Ha}^2}\left[f'\bar{f} + f\bar{f}' + zf'\bar{f}' + k^2 z\bar{f}f\right], && (5.37) \\
\frac{\mathrm{d}\psi_1}{\mathrm{d}z} =& -\frac{k}{4}fq_0' - \frac{k}{2}\left[2q_2\bar{f}' + \bar{f}q_2'\right] - \frac{ik}{\mathrm{Ha}^2}\left(u_1 + iv_1\right) - i\mathrm{B_s}kq_1, && (5.38) \\
\frac{\mathrm{d}\psi_2}{\mathrm{d}z} =& \frac{k}{2}\left[h_1 f' - 3h_3\bar{f}' - h_1' f - h_3'\bar{f} - q_1' f - q_3'\bar{f} - 3q_3\bar{f}' + q_1 f'\right] \\
& - \frac{1}{\mathrm{Ha}^2}\left[\frac{k^2}{2}ff' - 4k^2 v_2 + 2ik\left(u_2 + iv_2\right)\right] - 2i\mathrm{B_s}kq_2, && (5.39) \\
\frac{\mathrm{d}\psi_3}{\mathrm{d}z} =& \frac{k}{2}\left[2q_2 f' - 4q_4\bar{f}' - q_2' f - q_4'\bar{f}\right] - \frac{3ik}{\mathrm{Ha}^2}\left(u_3 + iv_3\right) - 3i\mathrm{B_s}kq_3, && (5.40) \\
\frac{\mathrm{d}\psi_4}{\mathrm{d}z} =& \frac{k}{2}\left[3h_3 f' - h_3' f + 3q_3 f' - 5q_5\bar{f}' - q_3' f - q_5'\bar{f}\right] \\
& - \frac{4ik}{\mathrm{Ha}^2}\left(u_4 + iv_4\right) - 4i\mathrm{B_s}kq_4, && (5.41) \\
\frac{\mathrm{d}\psi_n}{\mathrm{d}z} =& \frac{k}{2}\left[\left(n-1\right)q_{n-1}f' - \left(n+1\right)q_{n+1}\bar{f}' - q_{n-1}' f - q_{n+1}\bar{f}\right] \\
& - \frac{ink}{\mathrm{Ha}^2}\left(u_n + iv_n\right) - in\mathrm{B_s}kq_n. && (5.42)
\end{aligned}
$$

Equations (5.37) to (5.42) are solved subject to the boundary condition $\psi = 0$ at $z = 0$. However, we also aim to satisfy the boundary condition

$$\frac{\partial}{\partial x}\psi\left(x, 1\right) = 0, \tag{5.43}$$

since there is no fluid flux through the boundary at $z = 1$. This second boundary condition on a first order in z system determines the geostrophic, flow which up to this point has been arbitrary. This gives the condition

$$\psi_n\left(1\right) = 0, \tag{5.44}$$

for $n = 1 \dots N$. The choice of solving up to the N^{th} harmonic in ψ_n is to keep the problem square so that the system of equations is not overdetermined.

All the equations we wish to solve are solved by `bvp4c`. However, an initial choice of u_n and v_n will not (in practice) satisfy (5.44), meaning that the geostrophic velocity has to readjust in order to satisfy (5.44). To overcome this issue, the ODEs that depend on the geostrophic coefficients, i.e. equations (5.28)–(5.32) and (5.38)–(5.42), are solved inside an `Fsolve` routine. `Fsolve` is an inbuilt Matlab function that solves a system of nonlinear equations subject to

$$F\left(\boldsymbol{x}\right) = \mathbf{0}, \tag{5.45}$$

where $F\left(\boldsymbol{x}\right)$ is set to (5.44) and $\boldsymbol{x}$ is a vector containing the coefficients u_n and v_n.

For a given initial seed of $\boldsymbol{x} = (u_1, \ldots, u_n, v_1, \ldots, v_n)$, the quantities $h\left(x,z\right)$ and $\psi\left(x,z\right)$ are calculated inside `Fsolve` and $\psi_n\left(1\right)$ is evaluated. If (5.44) is not satisfied then the coefficients $\boldsymbol{x}$ are changed and the system of equations is re-evaluated for the new coefficients. This process is repeated until (5.44) is achieved within a numerical tolerance; the tolerance can be imposed on the step size in $\boldsymbol{x}$, the function evaluation or the first order optimality. We set the step size and function evaluation tolerances to 10^{-7} and the first order optimality tolerance is left at its default value of 10^{-6}. Once the tolerance has been achieved, the program terminates and Taylor's constraint is then satisfied to the required degree of accuracy.

To summarise this procedure, an N-term expansion for (5.16) results in $2N$ unknowns (N for u_n and N for v_n). We then solve for $2N+3$ equations in $q_n\left(z\right)$ $(q_0, \ldots, q_{N+1}, \bar{q}_1 \ldots, \bar{q}_{N+1})$,; this is to ensure all the terms are accounted for when integrating $\psi\left(x,z\right)$. To keep the problem square, we solve $2N$ equations for the $\psi\left(z\right)$ harmonics (ψ_n up to the N^{th} harmonic and the conjugates) for the $2N$ unknowns in u_n and v_n. We note that $\psi_0\left(z\right)$ trivially satisfies (5.44) as it does not have any x-dependence, so this is not included in the constraint in the `Fsolve` routine, but it is still calculated for the full solution to $\psi\left(x,z\right)$.

In figure 5.1 a flow chart highlights the main steps and processes for the numerical procedure.

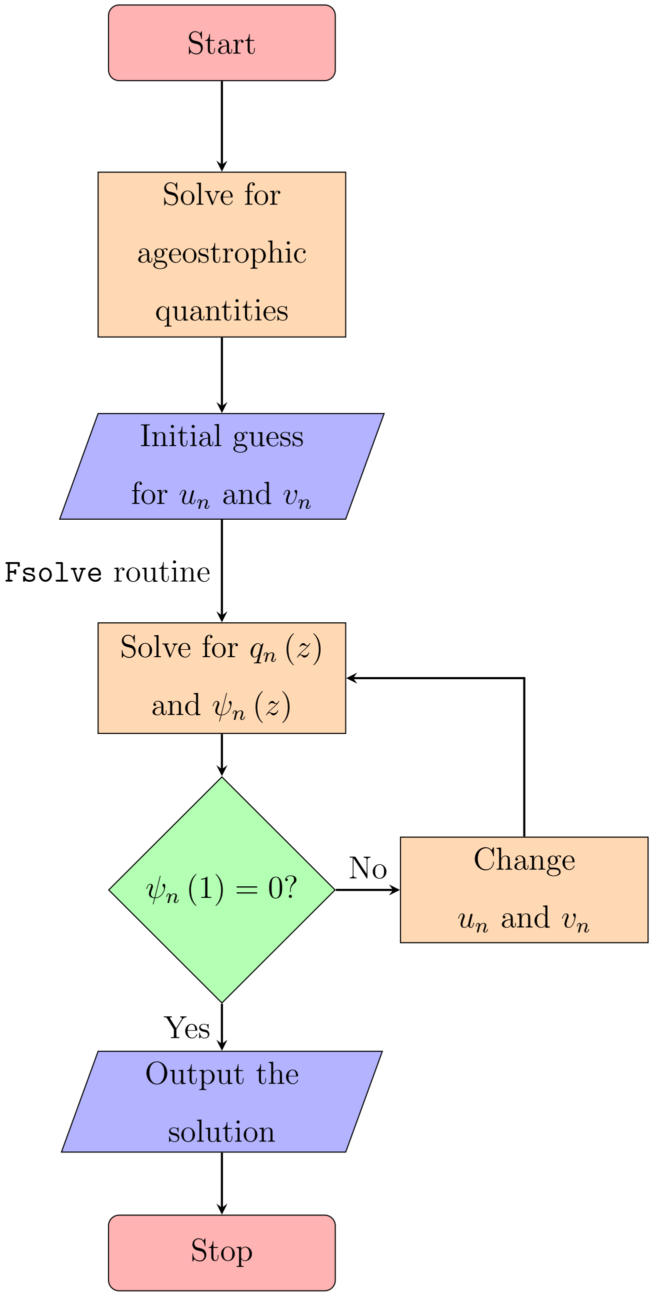

Figure 5.1: Flow chart for MATLAB implementation.

5.1.1 Low Rm, inviscid approach

In the inviscid, small Rm limit and when $\mathrm{B_s} = 0$, the numerical method described in §5.1 has its limitations. Unfortunately the `Fsolve` routine, as expected, struggles to resolve the geostrophic flow since the solution is singular in the small Rm limit. In theory, the code would require infinitely many modes to resolve the infinite gradient at $x = 0$. To overcome this, we employ a different approach. The method described next will be for the $\mathrm{B_s} = 0$ case.

In the low Rm regime, the geostrophic flow is of the form

$$V_0'(x) = \tilde{V}_0 k \cot(kx). \tag{5.46}$$

We therefore introduce the quantity

$$\mathcal{W}(x) = \sin(kx) V_0'(x), \tag{5.47}$$

which is well behaved and takes the form of $\cos(kx)$ as $\mathrm{Rm} \to 0$. The aim now is to solve for the function $\mathcal{W}(x)$. We write (5.47) as a Fourier expansion,

$$\mathcal{W}(x) = \frac{i}{2}\left(e^{-ikx} - e^{ikx}\right) V_0'(x) = \sum_{n=1}^{N} (u_n + iv_n) e^{inkx} + \text{c.c.}. \tag{5.48}$$

The PDEs for $A(x,z)$, $J_y(x,z)$ and $v(x,z)$ are the same as before, i.e. (5.1),(5.2) and (5.3) with $\mathrm{B_s} = 0$, so the focus is now on (5.23) and (5.5),

$$\frac{\partial^2 h_g}{\partial z^2} + \frac{\partial^2 h_g}{\partial x^2} - \mathrm{Rm} z \frac{\partial h_g}{\partial x} = \frac{\mathrm{d}V_0}{\mathrm{d}x}\left(\frac{i}{2}\bar{f}' e^{-ikx} - \frac{i}{2} f' e^{ikx}\right), \tag{5.49}$$

$$\frac{\partial \psi}{\partial z} = \frac{\partial (H, A)}{\partial (x, z)}. \tag{5.50}$$

Multiplying (5.49) by $\sin(kx)$ we can express it in terms of $\mathcal{W}(x)$ as

$$\frac{i}{2}\left(e^{-ikx} - e^{ikx}\right) \mathcal{L}(h_g) = \mathcal{W}(x)\left(\frac{i}{2}\bar{f}' e^{-ikx} - \frac{i}{2} f' e^{ikx}\right), \tag{5.51}$$

where $\mathcal{L}$ is the linear operator on the left-hand side of (5.49). Substituting the expression (5.48) into (5.51) gives

$$\frac{i}{2}\left(e^{-ikx} - e^{ikx}\right) \mathcal{L}(h_g) = \left[\sum_{n=1}^{N} \frac{i}{2}(u_n + iv_n) \bar{f}' e^{ik(n-1)x} - \frac{i}{2}(u_n + iv_n) f' e^{ik(n+1)x} + \text{c.c.}\right], \tag{5.52}$$

which can be expressed as,

$$\begin{aligned}\frac{i}{2}\left(e^{-ikx}-e^{ikx}\right)\mathcal{L}\left(h_g\right)=&\frac{i}{2}\left[\sum_{n=0}^{N-1}\left(u_{n+1}+iv_{n+1}\right)\bar{f}'e^{inkx}\right.\\&\left.-\sum_{n=2}^{N+1}\left(u_{n-1}+iv_{n-1}\right)f'e^{inkx}+\text{c.c.}\right]\end{aligned}\tag{5.53}$$

The function $h_g\left(x,z\right)$ must take the form

$$h_g\left(x,z\right)=\sum_{n=1}^{N}q_n\left(z\right)e^{inkx}+\text{c.c.}.\tag{5.54}$$

The left hand side of (5.52) is then expanded as

$$\begin{aligned}&\sum_{n=0}^{N-1}\frac{i}{2}\left(q''_{n+1}-\left(n+1\right)^2k^2q_{n+1}-i\left(n+1\right)k\text{Rm}zq_{n+1}\right)e^{inkx}+\text{c.c.}\\-&\sum_{n=2}^{N+1}\frac{i}{2}\left(q''_{n-1}-\left(n-1\right)^2k^2q_{n-1}-i\left(n-1\right)k\text{Rm}zq_{n-1}\right)e^{inkx}+\text{c.c.}\end{aligned}$$

By substituting the next harmonic in $q_i\left(z\right)$, we can simplify the ODEs, and as a result, the even terms satisfy

$$q''_{2n}-4n^2k^2q_{2n}-2ink\text{Rm}zq_{2n}=\left(u_{2n}+iv_{2n}\right)\bar{f}'+\sum_{m=1}^{n}\left(u_{2m}+iv_{2m}\right)\left(\bar{f}'-f'\right)$$

whereas the odd terms satisfy

$$\begin{aligned}q''_{2n+1}-\left(2n+1\right)^2k^2q_{2n+1}-i\left(2n+1\right)k\text{Rm}zq_{2n+1}=&\left(u_{2n+1}+iv_{2n+1}\right)\bar{f}'\\&+\sum_{m=0}^{n-1}\left(u_{2m+1}+iv_{2m+1}\right)\left(\bar{f}'-f'\right).\end{aligned}$$

The solution to $\psi\left(x,z\right)$ follows the same procedure as outlined above.

5.2 Verification of solutions

Before we begin a full exploration of parameter space we need to verify that the numerical solutions are correct and well resolved. The obvious starting point is to compare the numerics to the asymptotic results found in Chapter 4. We shall also consider varying the boundary condition of the ageostrophic part of $v\left(x,z\right)$, which is not required in the theory, but numerically is required for integration of the individual harmonics (5.13) – (5.15).

In order to test whether the solution is well resolved we shall consider increasing the number of modes in the expansion of $V_0'(x)$ and comparing the solutions. Plotting the energy spectra of the harmonics of $V_0'(x)$, $q_n(z)$ and $\psi_n(z)$ will also help confirm whether the solution to the system of equations is resolved appropriately.

5.2.1 Comparison with asymptotic results

By using the asymptotic results we can verify that the code is working in the small Rm regime. The difficulty with the inviscid regime is that the geostrophic flow is singular, which is difficult to achieve numerically. For plotting purposes we use $N_x = N_z = 100$ meshpoints — this does not affect the truncation or solution in any sense as this is determined by the choice of modes in the Fourier expansion of the geostrophic flow.

Below we compare the asymptotic and numerical results for an inviscid fluid at small Rm. In both codes we expect the ageostrophic quantities to match with high accuracy since they are well-behaved for the inviscid interior solution at small Rm. The geostrophic quantities in $h(x,z)$ and $\psi(x,z)$ will be different between the two numerical approaches because of the difference in evaluating the singular $V_0'(x)$ term and the nonsingular $\mathcal{W}(x)$.

In figure 5.2, the numerical solution of (5.6) matches well when compared to the z component of (4.18) in the asymptotic theory. This is achieved by setting $\mathrm{Rm} = 0$ in the numerical code.

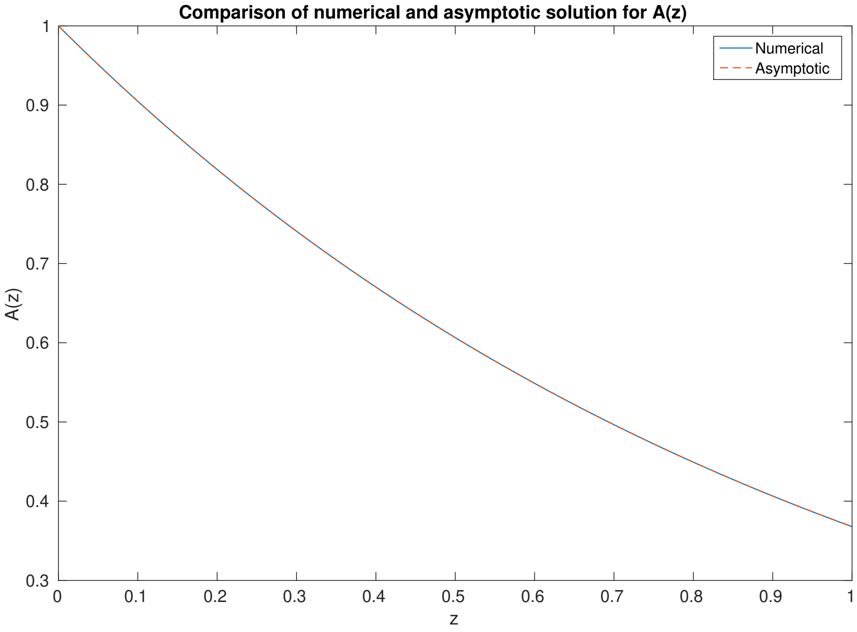

Figure 5.2: Comparison of numerical solution of (5.8) and (4.18) for $k = 1$.

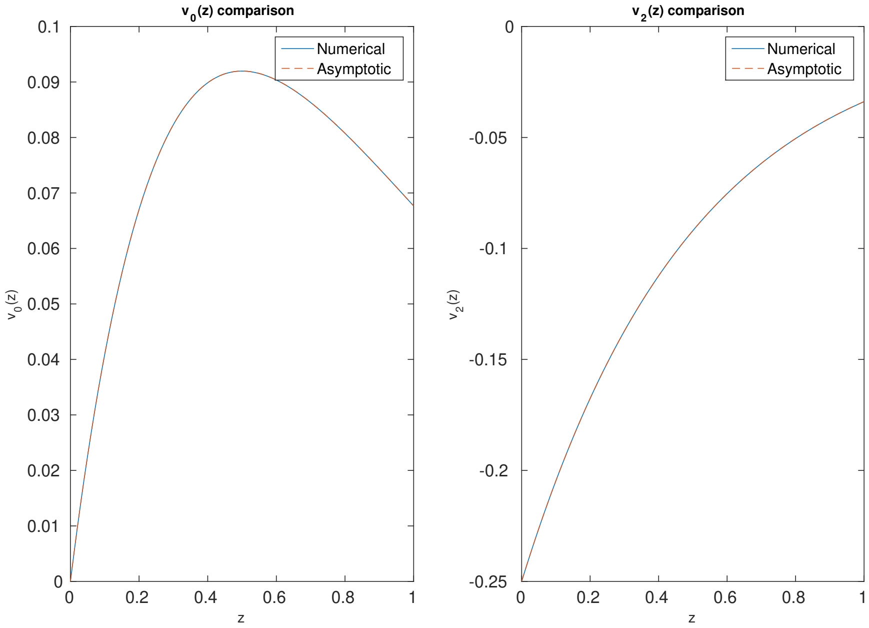

Figure 5.3: Comparison of numerical solution of (5.13), (5.15) and (4.20) for $k = 1$.

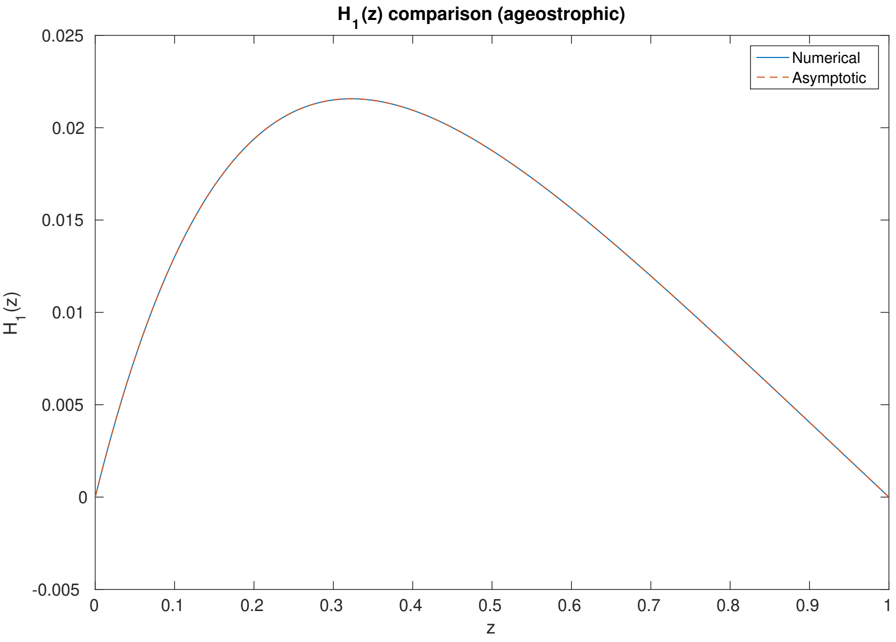

Figure 5.4: Comparison of (4.26) and the solution to (5.20).

In figure 5.3, the ageostrophic solutions $v_0(z)$ and $v_2(z)$ are plotted against the corresponding asymptotic solution (4.20). In order for the numerical solution to match to the asymptotic solution (4.20) we impose a boundary condition derived from the asymptotic result by evaluating (4.20) at $z = 0$, namely

$$v(x, z) = -\frac{1}{4k}\cos(2kx). \tag{5.55}$$

Hence the boundary condition at $z = 0$ is

$$v_0(z) = 0, \tag{5.56}$$

$$v_2(z) = -\frac{1}{8k}. \tag{5.57}$$

We note that the choice of boundary condition is arbitrary as it does not affect the overall solution (see §5.2.2). From herein all solutions are subject to the boundary conditions (5.56)–(5.57).

In figure 5.4 the small Rm ageostrophic solution to $H(x, z)$, given by (5.20), is compared to the numerical solution of (4.26), thus confirming that the solution is correct in this regime.

In figure 5.5, using the numerical method that evaluates (5.16), the numerical solution of the geostrophic meridional field, $h\left(x,z\right)$, the harmonics $\psi_0\left(z\right)$ and $\psi_2\left(z\right)$, and the geostrophic flow are plotted, together with their corresponding asymptotic result. As expected, the code struggles to find a smooth solution to $V_0'\left(x\right)$, owing to the singularity at $x=0,\pi$. Away from the singularity there is some agreement, but it is quite poor. Near the singularity Gibbs phenomena occurs. Even when increasing the number of modes, the singularity will always cause an issue when evaluating (5.16), as shown in figure 5.7 where we have tested for the cases $M=10,20,30,40$ modes.

In figure 5.6 the same quantities are evaluated, but for the code in which $\mathcal{W}\left(x\right)$ is evaluated and in which $V_0'\left(x\right)$ is then recovered by dividing through by $\sin\left(kx\right)$. Here we can see that this is a much better match for the geostrophic flow. Figure 5.6 shows the solution to an $M=5$ mode expansion, taking 96.6 seconds to compute, whilst figure 5.5 is the solution to an $M=40$ mode expansion, taking 7975.3 seconds to compute.

Although the direct evaluation of (5.16) for an inviscid fluid at small Rm results in a poorly resolved solution for the geostrophic flow, the code works reasonably well at solving the harmonics of $h\left(x,z\right)$ and $\psi\left(x,z\right)$. We are confident that the solutions will be accurate providing we are not in the inviscid small Rm limit. The indirect evaluation of $V_0'\left(x\right)$ is computationally cheaper, but limited to only inviscid solutions at small Rm.

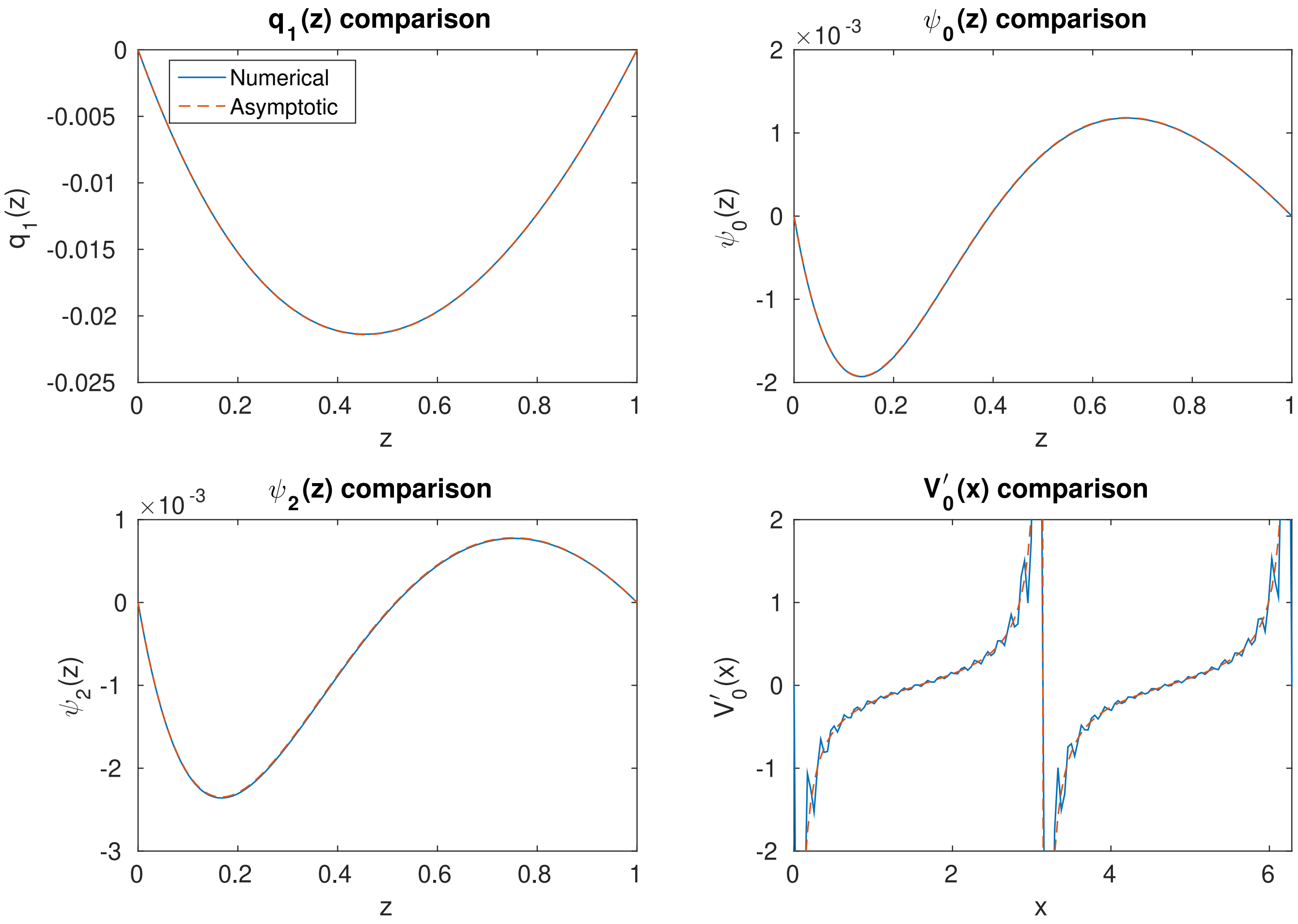

Figure 5.5: Comparison of the geostrophic solution for the z dependence of $h\,(x, z)$, $\psi\,(x, z)$ and $V_0'\,(x)$ using $M = 40$ modes.

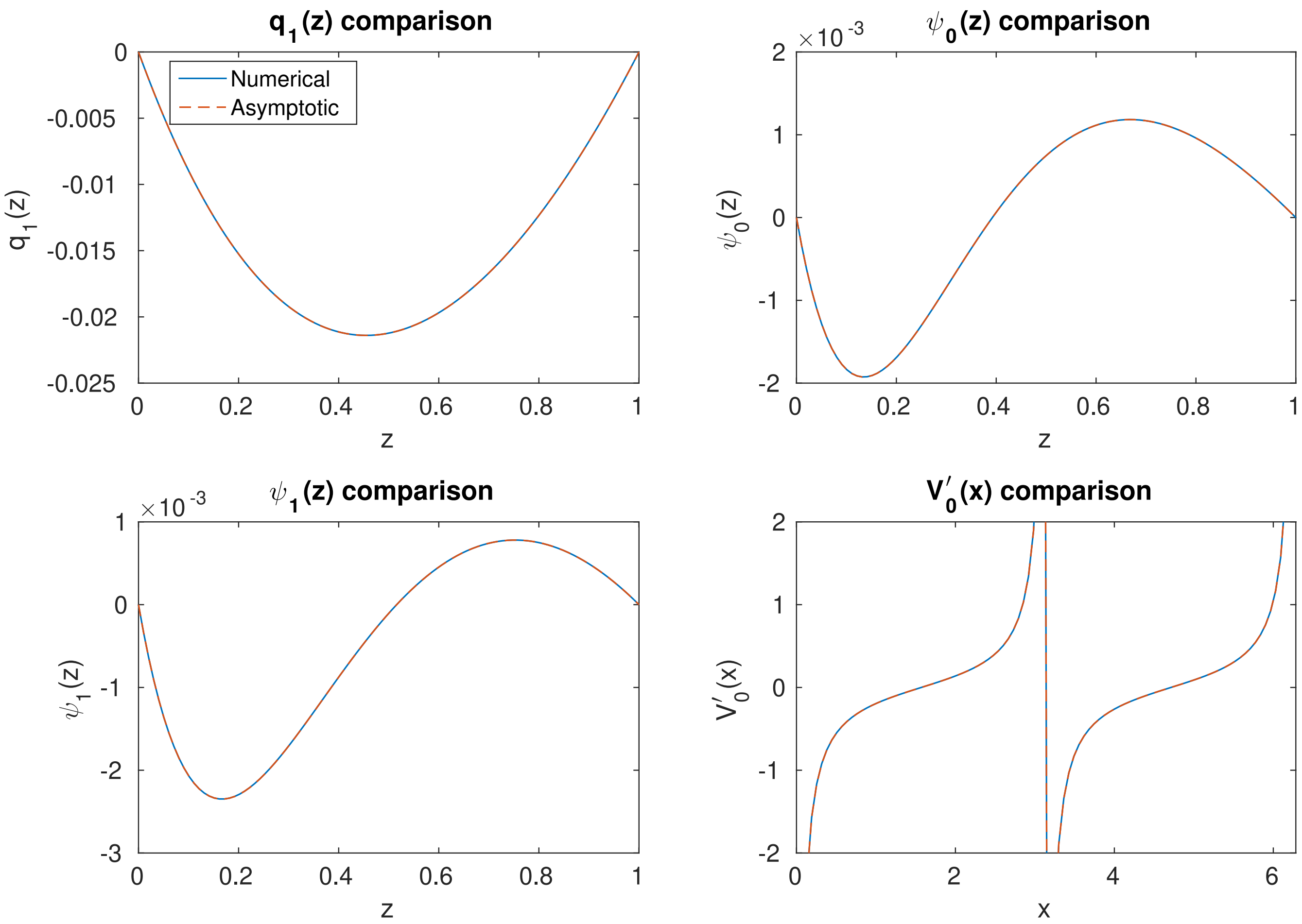

Figure 5.6: Comparison of the geostrophic solution for the z dependence of $h(x,z)$, $\psi(x,z)$ and $V_0'(x)$ evaluting the function $\mathcal{W}(x)$ using $M=5$ modes.

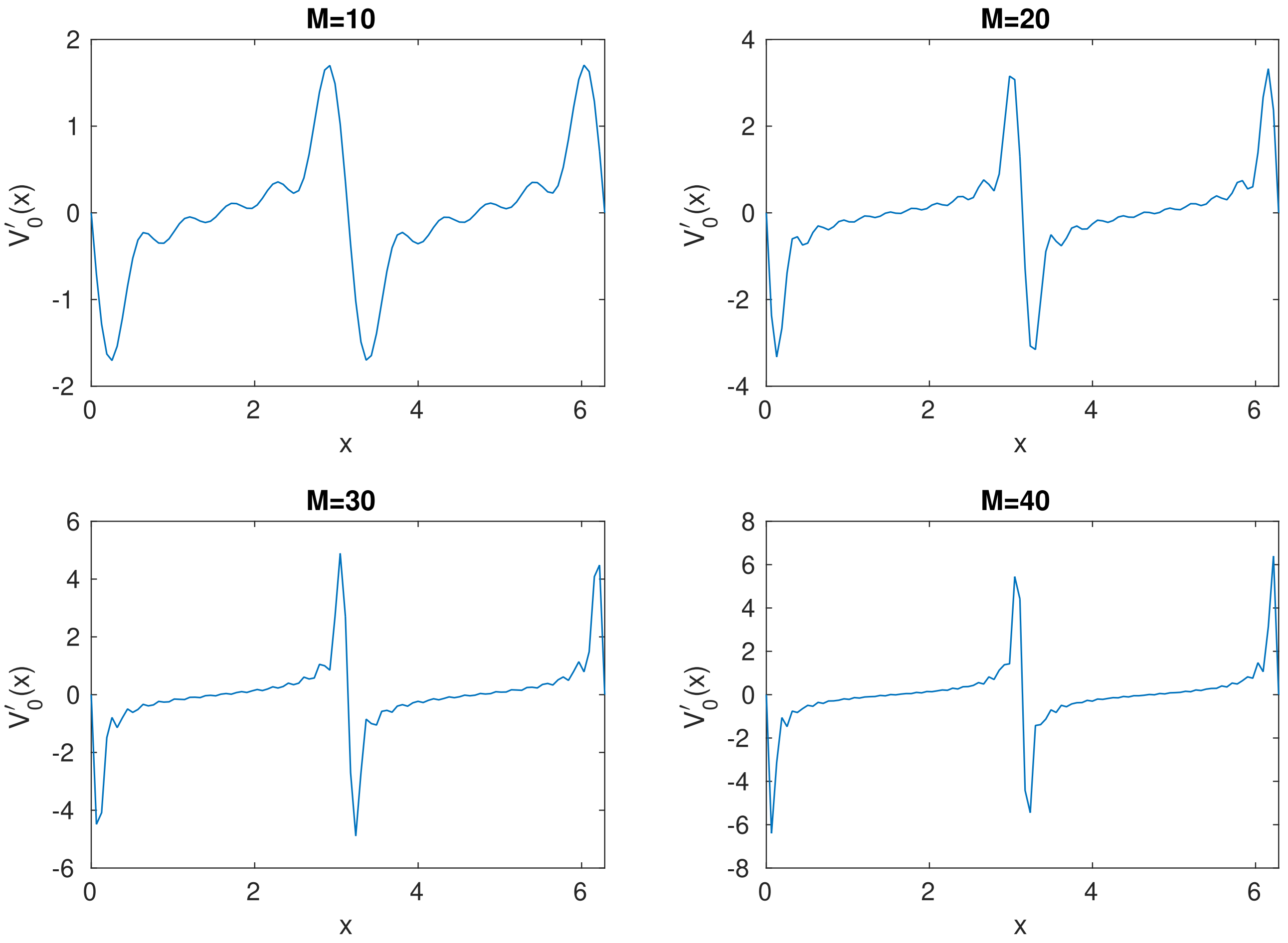

Figure 5.7: Direct $V_0'(x)$ evaluation for different number of modes. Computational times for $M = 10, 20, 30, 40$ are $t = 385.7, 1861.1, 4627.8, 7975.3s$ respectively.

5.2.2 Boundary conditions

The subtlety in the code compared to the theory is the integration of the ageostrophic component of $v\left(x,z\right)$, i.e. integrating equations (5.13)–(5.15). The numerical solver requires one boundary condition to solve the first order ODE, and the choice of this will change the solution to the geostrophic part $V_0'\left(x\right)$. However, this should not change $v_x\left(x,z\right)$ in its entirety, as it only adds an extra constant to $v\left(x,z\right)$. The same also applies to the full solution of $H\left(x,z\right)$ and $\psi\left(x,z\right)$.

To highlight this issue, we test two cases: one with the boundary conditions (5.55), and the other with a boundary condition in which we simply impose zero meridional flux at the bottom of the layer, i.e. $v\left(x,z\right)=0$. Neither of these should change the solution, although they almost always change the solution to the separated ageostrophic and geostrophic quantities.

In figure 5.8 we plot the contours of both solutions and, in figure 5.9, the difference between them, namely

$$D=\sqrt{\left(Q_A-Q_B\right)^2}, \tag{5.58}$$

where Q is one of $v_x\left(x,z\right)$, $H\left(x,z\right)$ and $\psi\left(x,z\right)$ evaluated with boundary condition A (equations (5.56)–(5.57)) or boundary condition B ($v\left(x,z\right)=0$). This is tested for the case $\mathrm{Rm}\to 0$, $\mathrm{B_s}=0$, $\mathrm{Ha}=1$ and $k=1$.

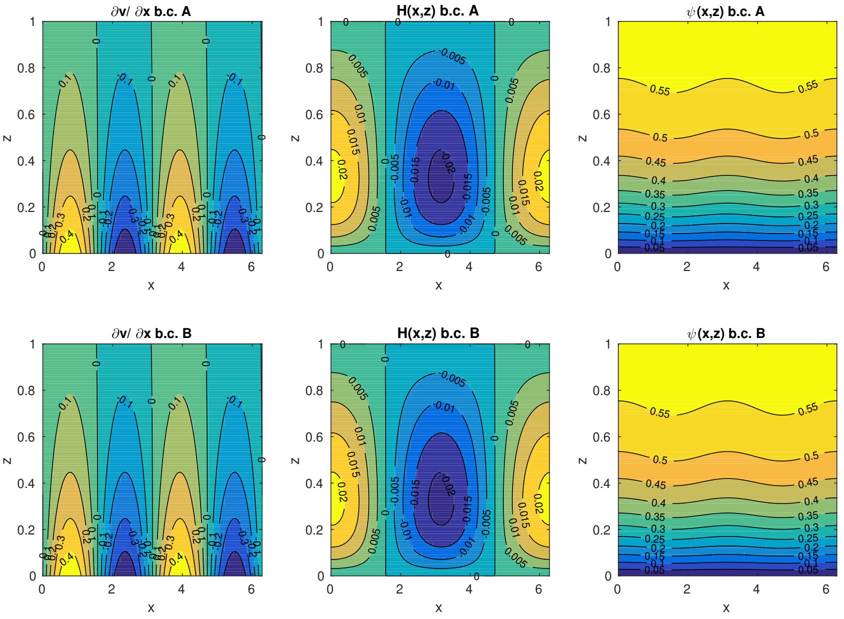

Figure 5.8: Plots of $v_x\,(x, z)$, $H\,(x, z)$ and $\psi\,(x, z)$ for two different boundary conditions at $\mathrm{Ha} = 1$, $\mathrm{Rm} \to 0$, $\mathrm{B_s} = 0$ and $k = 1$.

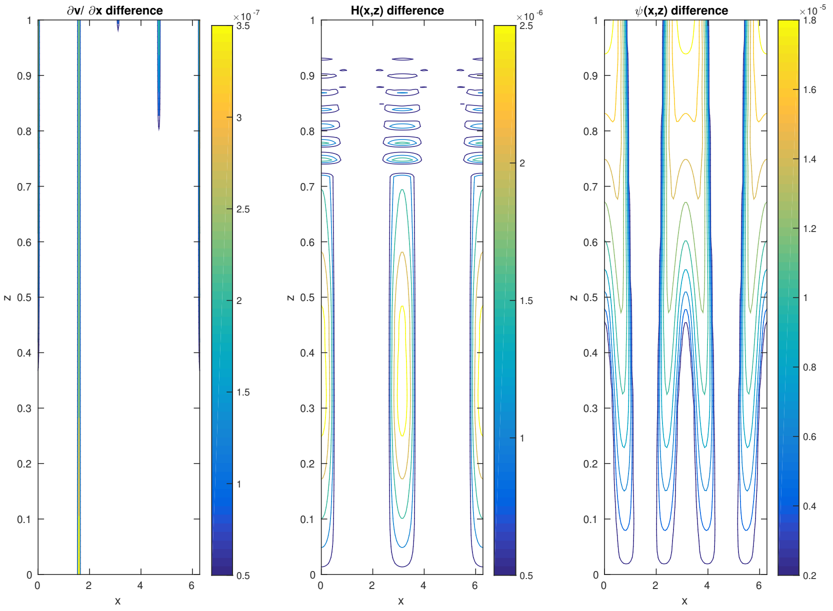

Figure 5.9: Contour plots of the difference between the two boundary conditions for ageostrophic $v\,(x, z)$

5.2.3 Energy spectra and scalings

The choice of how many modes to retain in the expansion (5.16) depends on the structure of $V_0'(x)$; too few modes can lead to a solution that is not well resolved. This will become apparent when we investigate the effects of varying the Hartmann number, Ha, at small Rm. To be confident that our solution is well resolved, one can either rerun the code for a variety of modes to see if the solution changes, or plot the energy spectra of the coefficients of $V_0'(x)$. In a well resolved solution, the energy of the higher harmonics should be insignificant compared to the rest of the spectra. We measure the energy of the harmonics of $V_0'(x)$ using

$$E_{u_n} = \frac{1}{2}u_n^2, \tag{5.59}$$

$$E_{v_n} = \frac{1}{2}v_n^2, \tag{5.60}$$

and for both $q_n(z)$, $\psi_n(z)$ we take the average over the domain, then calculate

$$E_{\psi_n} = \frac{1}{2}\langle\psi_n(z)\rangle^2. \tag{5.61}$$

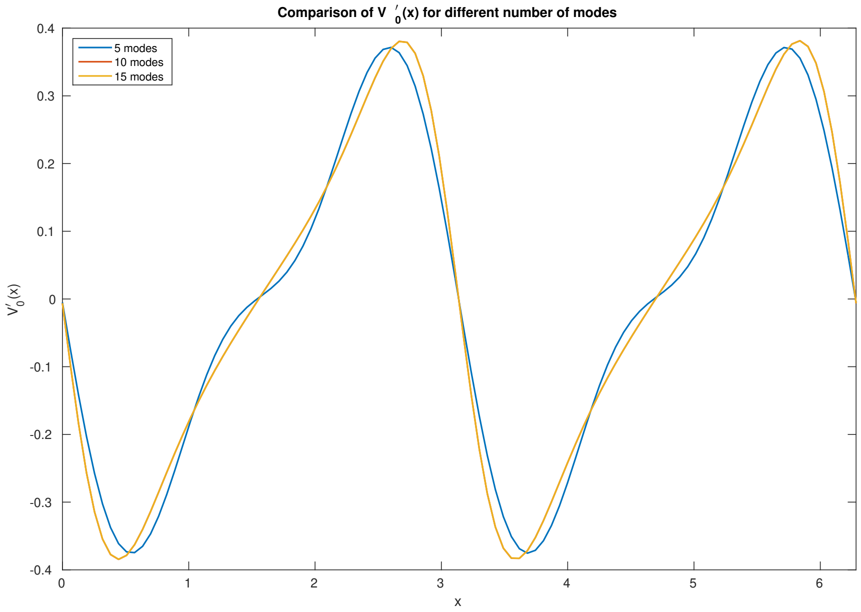

Figure 5.10: An example where the solution is not resolved at $N = 5$ modes, but $N = 10$ and $N = 15$ are consistent. $\mathrm{Ha} = 15$, $\mathrm{Rm} \to 0.1$ and $\mathrm{B_s} = 0$. Note that the red curve is obscured by the overlapping yellow curve in this plot.

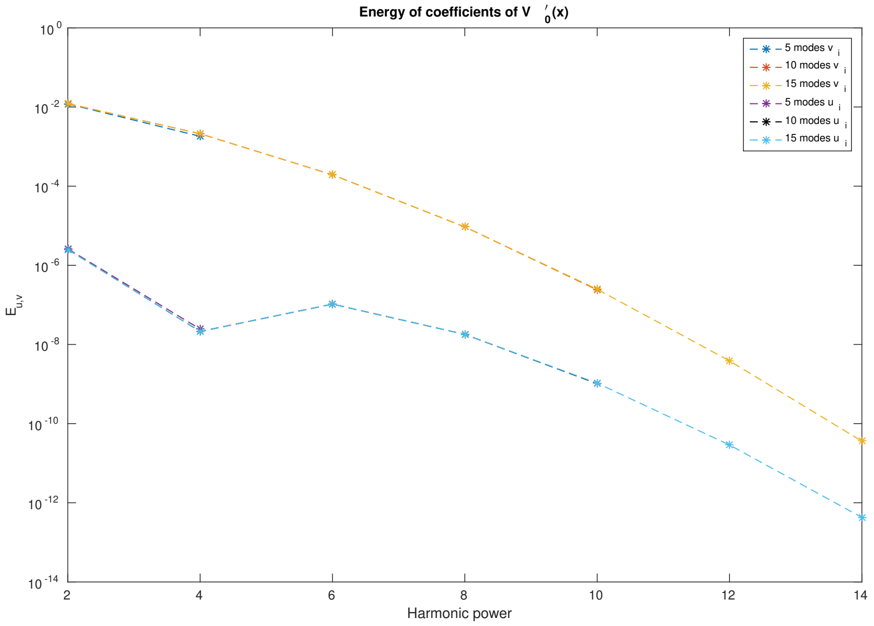

Figure 5.11: Comparisons of the energy spectra of the coefficients of $V_0'(x)$. The odd harmonics are omitted as they are numerically small.

Figure 5.11 confirms that the solution is well resolved with $N = 15$ modes, since the energy in the higher harmonics is much smaller than that at lower harmonics. Owing to the nature of the solutions in the $\mathrm{B_s} = 0$ case, only the even harmonics in $V_0'(x)$ are calculated, since the solutions have symmetry in x and, as a consequence, the odd harmonics are numerically small. Even with an initial seed of purely non-zero odd modes, the solution always reverts to the even harmonics being the only non-zero contribution.

5.2.4 Computation time

When running the code, it is useful to know how the running time scales with increasing modal expansion; this allows us to know what the limitations are for parameter space exploration. In the cases for large Ha, the number of modes will have to increase to accommodate for the small-scale structure near the boundary layer, so it is good to know how large can Ha be and how long it will take to compute a solution.

Below we plot the computational time for the code with increasing number of modes, to indicate how long it takes to find the solution. A line of fit can be made if we assume that the simulation time take the form

$$\tau = \lambda N^{\alpha}, \tag{5.62}$$

where τ is the time in seconds using a single processor machine. We would expect the scaling with N to be approximately independent of the computer used. We calculate the parameters as $\lambda = 15.26$ and $\alpha = 1.78$, where N is the number of modes.

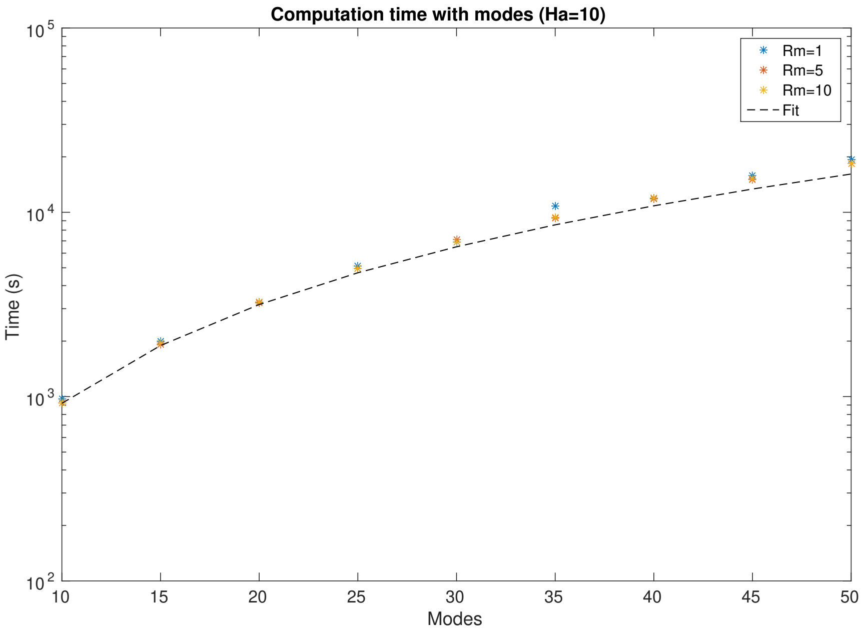

Figure 5.12: Computation time of runs with fixed Ha and various Rm against increasing modes.

5.3 Symmetries of the solutions

Equations (5.1) to (5.5) with the given boundary conditions have certain symmetry properties. All our solutions are periodic in space with period $2\pi/k$. This occurs because the magnetic field forcing at $z = 0$ is assumed periodic in $2\pi/k$ in the x-direction, and there is no other explicit x-dependence in the model equations.

However, some solutions have additional symmetries. There is an important distinction between the cases with $\mathrm{B_s} = 0$ and $\mathrm{B_s} \neq 0$. In Chapter 8 we will see that $\mathrm{B_s} \neq 0$ will break the following symmetries.

5.3.1 The case $\mathrm{B_s} = 0$ and $\mathrm{Rm} \sim \mathcal{O}\left(1\right)$

From (5.6), we note that because of the nature of the imposed field

$$A\left(x+\pi, z\right) = -A\left(x, z\right). \tag{5.63}$$

It follows that the current density has the symmetry

$$J_y\left(x+\pi, z\right) = -J_y\left(x, z\right). \tag{5.64}$$

From (5.3), when $\mathrm{B_s} = 0$, the right hand side of (5.3) consists of products of $A\left(x, z\right)$ and $J_y\left(x, z\right)$, it is apparent that the meridional flow has the symmetry

$$v\left(x+\pi, z\right) = v\left(x, z\right). \tag{5.65}$$

When $\mathrm{B_s} \neq 0$ this symmetry will be broken, as the $\mathrm{B_s}$ term in (5.3) reverses sign under the transition $x \to x+\pi$ but the Jacobian term does not.

From equations (5.4)–(5.5) we see that

$$H\left(x+\pi, z\right) = -H\left(x, z\right), \tag{5.66}$$

$$\psi\left(x+\pi, z\right) = \psi\left(x, z\right), \tag{5.67}$$

noting that the Hartmann number term in (5.5) preserves this symmetry. The geostrophic flow also respects this symmetry since $V_0'\left(x+\pi\right) = V_0'\left(x\right)$.

5.3.2 The case $\mathrm{B_s} = 0$ and $\mathrm{Rm} \to 0$

In this limit, (5.1) becomes purely real, and hence we have the additional symmetry,

$$A\left(x, z\right) = -A\left(-x, z\right), \tag{5.68}$$

along with the previous symmetry of (5.63). In this limit, all quantities become purely real, and noting that taking an x-derivative transforms odd functions into even functions, and vice versa, we have the following additional symmetries:

$$J_y\left(x,z\right) = J_y\left(-x,z\right), \tag{5.69}$$

$$v\left(x,z\right) = v\left(-x,z\right), \tag{5.70}$$

$$H\left(x,z\right) = H\left(-x,z\right), \tag{5.71}$$

$$\psi\left(x,z\right) = \psi\left(-x,z\right), \tag{5.72}$$

$$V_0'\left(x\right) = -V_0'\left(-x\right). \tag{5.73}$$

These results are all consistent with the results presented in Chapter 4.

Chapter 6

Numerical solutions in the absence of a horizontal field

In this chapter we present the solutions to the system of equations for general values of Rm and Ha without an imposed horizontal field, i.e. $\mathrm{B_s} = 0$. All the diagnostics described in §5 are used to determine whether the solution is well resolved.

6.1 General behaviour of ageostrophic quantities at moderate Rm

The effect of Rm on the ageostrophic components of $A(x,z)$, $v(x,z)$ and $H(x,z)$ is the same for both the inviscid and viscous regimes for small Λ. Large values of Rm are related to an increase in strength of the thermal shear in the stratified layer. At large Rm we expect the magnetic field to be strongly attenuated within the layer such that very little of the non-axisymmetric field exists at the top of the domain. This is supported by figure (6.1), which shows the magnetic potential field for specific values of Rm up to $\mathrm{Rm} = 100$.

In figure 6.1 we can see that the radial structure is strongly dependent on Rm; the field lines are bent by the strong shearing effect. The solutions presented in (6.1) are for $k = 1$; larger values of k correspond to shorter wavelengths, which would result in greater attenuation.

The ageostrophic meridional flow is plotted in figure 6.2. The magnitude of the velocity field does not change substantially as Rm increases. It is quite surprising that $v\,(x,z)$ does not follow a similar pattern to $A\,(x,z)$ as Rm increases given that $v\,(x,z)$ depends on the solution of $A\,(x,z)$. However, the large Rm solutions in figure 6.2 do become rather independent of z in the upper region where $A\,(x,z)$ and $J_y\,(x,z)$ are small. From equation (5.3), this is to be expected. Interestingly though, $v\,(x,z)$ itself is not necessarily small in the upper regions because the forcing due to $A\,(x,z)$ and $J_y\,(x,z)$ near $z=0$ generates a finite $v\,(x,z)$ which persists to the upper layers. This non-zero upper region $v\,(x,z)$ structure would be wiped out if there were significant viscous diffusion in the layer, but viscous diffusion is believed to be small in stably stratified layers. So although Stevenson's argument that non-axisymmetric magnetic fields are sheared away by the thermal wind in the stable layer still holds in the dynamical regime, it does not necessarily follow that the non-axisymmetric flow generated by the fluid is wiped out at the top of the layer.

Figure 6.3 shows that the ageostrophic part of the meridional field $H\,(x,z)$ is compressed into the lower half of the domain as Rm is increased. At large Rm we may begin to see boundary layer formation at $z=0$.

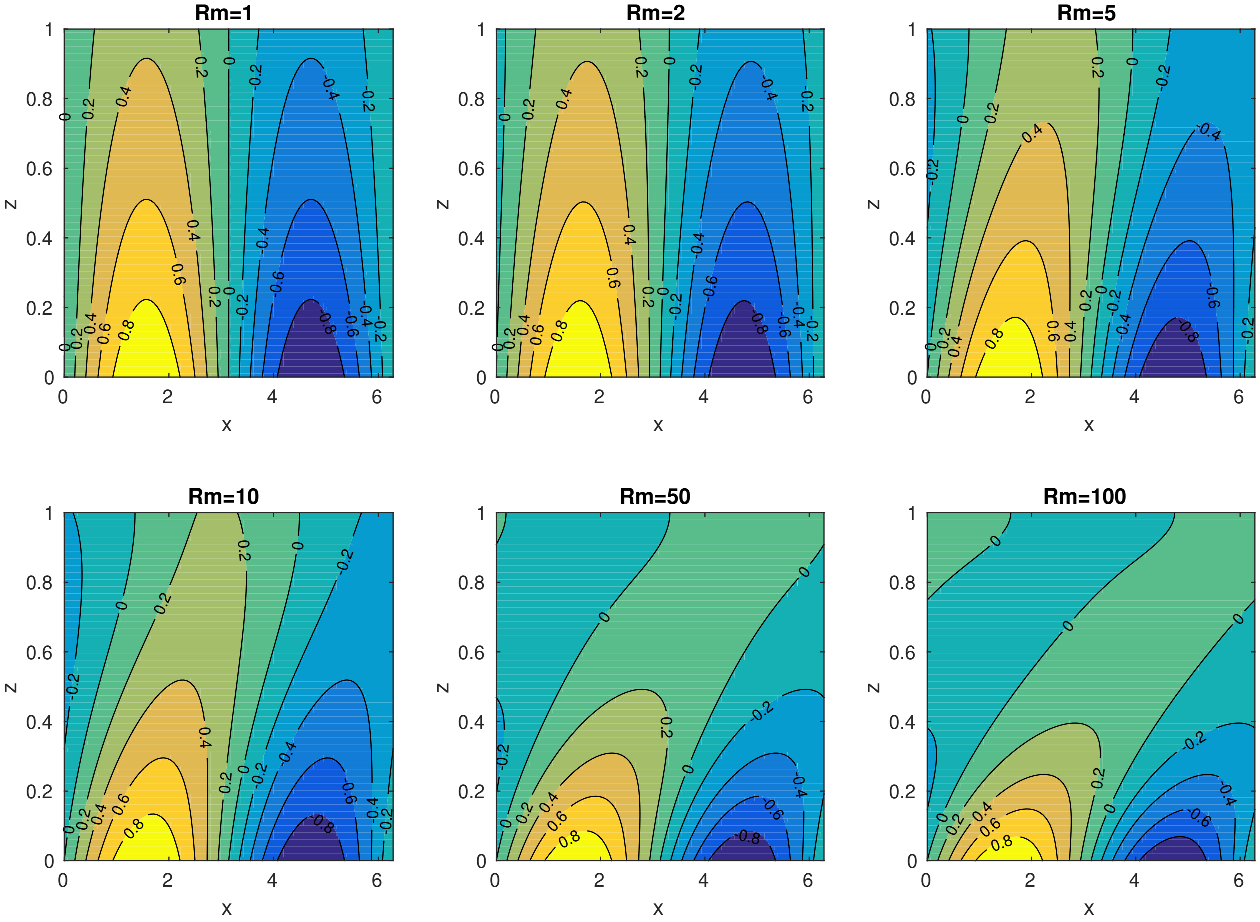

Figure 6.1: Contour plots of $A\left(x,z\right)$ as Rm increases.

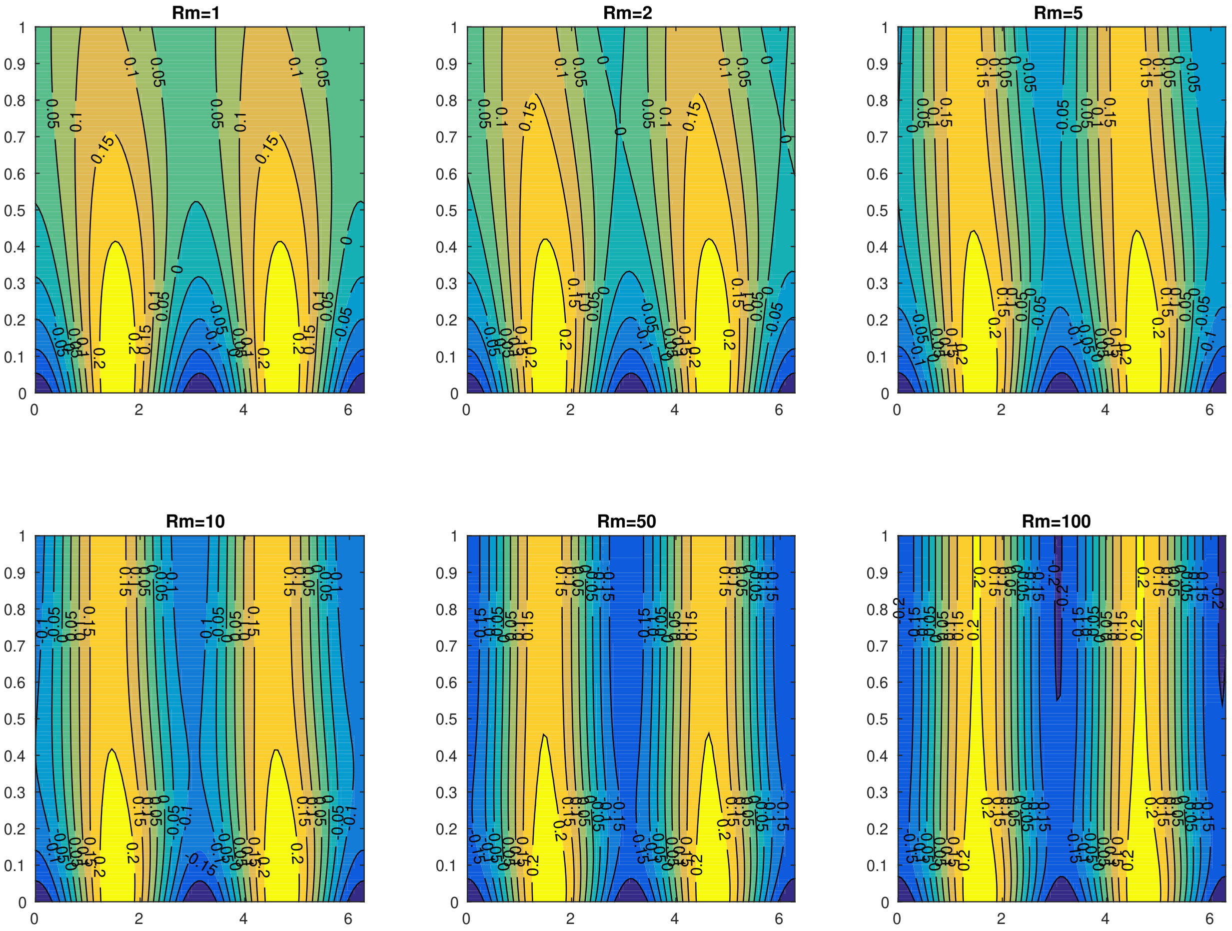

Figure 6.2: Contour plots of ageostrophic $v\,(x, z)$ as Rm increases.

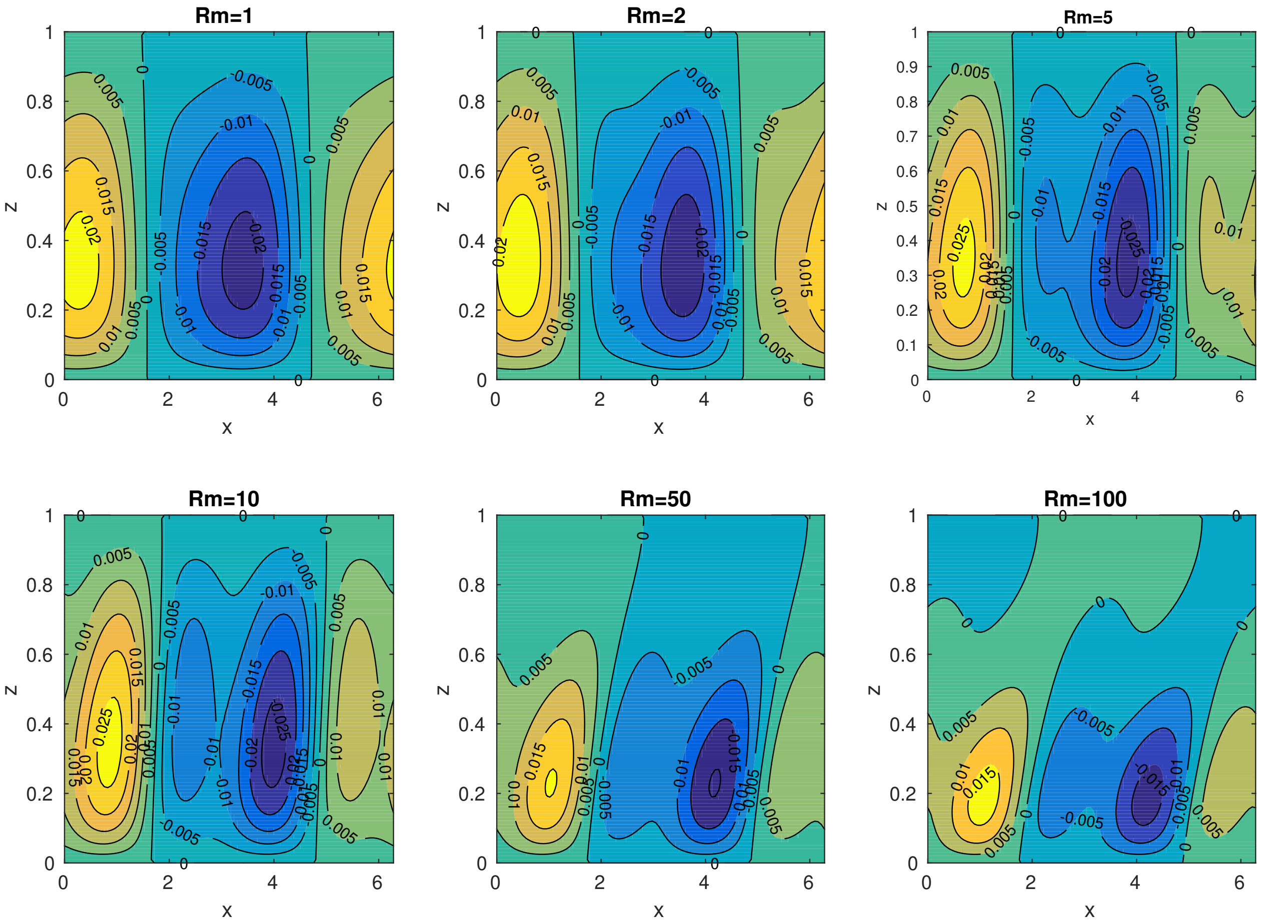

Figure 6.3: Contour plots of ageostrophic $H(x,z)$ as Rm increases.

6.2 Inviscid, moderate Rm

At moderate Rm the geostrophic velocity, $V_0'(x)$, is no longer singular for an inviscid fluid, i.e. $\text{Ha} \to \infty$. This was somewhat unexpected as one might expect this singularity to continue to exist until either the introduction of the horizontal field or viscosity into the system of equations.

In figure 6.5, $H(x,z)$, $\psi(x,z)$, $v_x(x,z)$ and $V_0'(x)$ are plotted at $\text{Rm} = 100$ for an inviscid fluid. The solution presented is calculated using $N = 30$ modes in the expansion for $V_0'(x)$, given by equation (5.16). Figure 6.5 shows that $V_0'(x)$ is smooth and continuous in x. The other three quantities considered all feature a radial structure that is strongly confined to the lower half of the domain.

The azimuthal symmetry of $\psi(x,z)$ is still π-periodic, but is no longer symmetric about π unlike in the $\text{Rm} \to 0$ solution (cf. figure 4.4). The effect of increasing Rm is to shear the structure of the stream function and compress it. The radial structure of $\psi(x,z)$ is compressed to the lower third of the domain at $\text{Rm} = 100$.

The solution presented in figure 6.5 is well resolved, as verified by the energy spectra of $V_0'(x)$ and $\psi(x,z)$. In figure 6.6, these energies, defined by equations (5.59), (5.60) and (5.61), decrease rapidly with harmonic power n — this being a sign of a well-resolved solution. We note that there are some unusual spikes in energy in E_ψ around $n = 20$ but this is due to numerical noise given the size of E_ψ at $n = 20$. Only the even harmonics are plotted in the energy spectra for $\psi(x,z)$ and $V_0'(x)$ as the odd harmonics are numerically small; this is a consequence of the zero horizontal field solutions. The geostrophic flow and stream function are symmetric throughout the $\text{B}_\text{s} = 0$ case.

The meridional field has a much more drastic change in its structure as Rm is increased; there is both the effect of shearing in x and compression in z; its amplitude has also decreased by a factor of 10 from the small Rm solution as seen in figure 6.3. The maximum amplitude of the ageostrophic magnetic field $H^a(x,z)$ is plotted against Rm in figure 6.4. As we can see, there is a trend of decreasing amplitude for the meridional magnetic field as Rm increases.

Higher values of Rm lead to boundary layer formation, which suggest that there is singular behaviour in $\psi\left(x,z\right)$ as $\mathrm{Rm}\rightarrow\infty$. In figure 6.7, higher values of Rm are sampled and the leading harmonic $\psi_0\left(z\right)$ is plotted, showing a decreasing width of the boundary layer near $z=0$. From inspection of higher values of Rm, the boundary layer maximum is calculated. A line of fit of these values is plotted in figure 6.8, showing that the maxima decrease approximately as $\mathrm{Rm}^{-0.65}$.

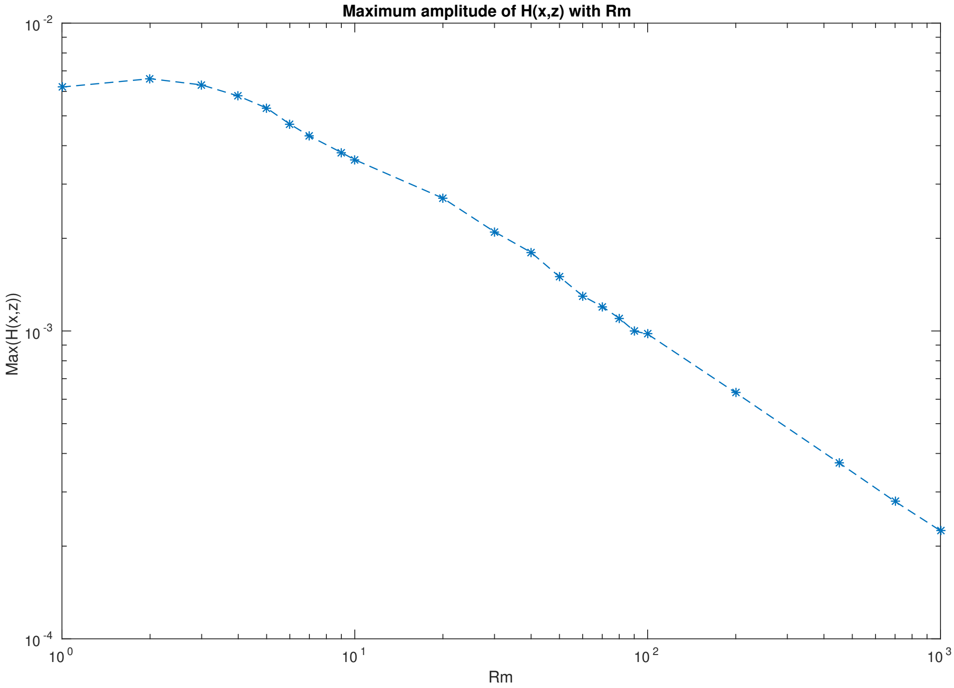

Figure 6.4: Maximum amplitude of $H^a\left(x,z\right)$ as Rm increases.

6.2.1 Why does Rm remove the singularity in $V_0'\left(x\right)$?

As shown in §4, in the limit as $\mathrm{Rm}\rightarrow 0$, the magnetic potential $A\left(x,z\right)$ vanishes at the point $x=0$ and $x=\pi$ throughout the whole layer. This means that the magnetic stretching term has to overcome the lack of field at the points $x=0,\pi$ by having an infinite geostrophic gradient at these points as the geostrophic flow is purely a function of x. When Rm increases the strength of the shear flow, it causes the field lines to bend, as seen in figure 6.1. The consequence of this is that at the given fixed points $x = 0, \pi$ there will eventually be a point in z where there is a non-zero field line, resulting in the magnetic stretching no longer requiring an infinite geostrophic gradient at those points. This suggests that there is a critical Rm beyond which the singularity does not occur. As soon as Rm is non-zero, there will be a small field contribution at $x = 0, \pi$ and hence the singularity will no longer occur. For non-zero Rm it would be expected that a finite peak in $V_0'(x)$ occurs around the two points.

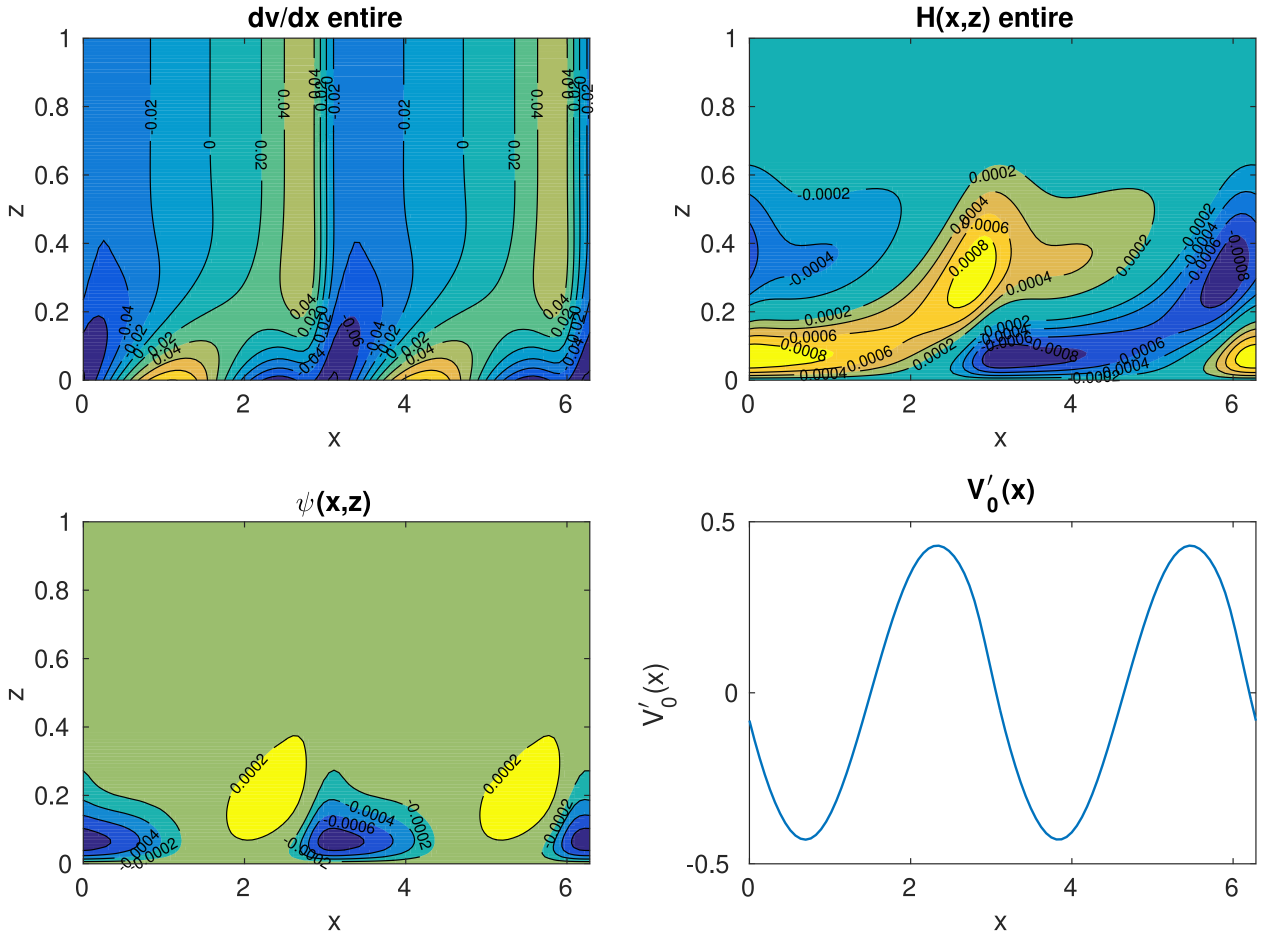

Figure 6.5: Contours of $v_x(x,z)$, $H(x,z)$ and $\psi(x,z)$ at $\mathrm{Rm} = 100$ and $\mathrm{Ha}^{-1} = 0$ with $N = 30$ modes.

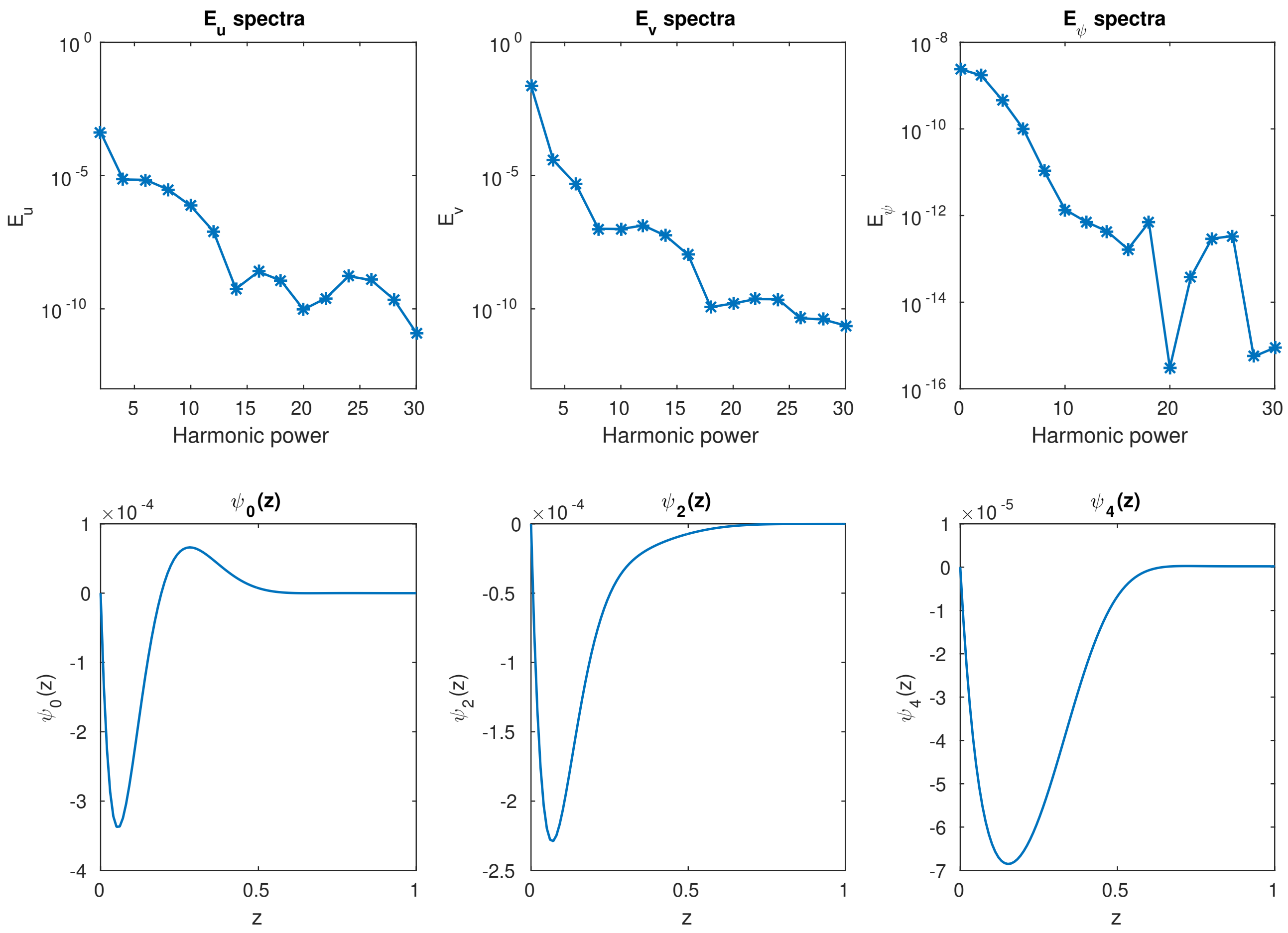

Figure 6.6: Energy spectra of $\psi\,(x,z)$ at $\mathrm{Rm} = 100$ and $\mathrm{Ha}^{-1} = 0$ with $N = 30$ modes.

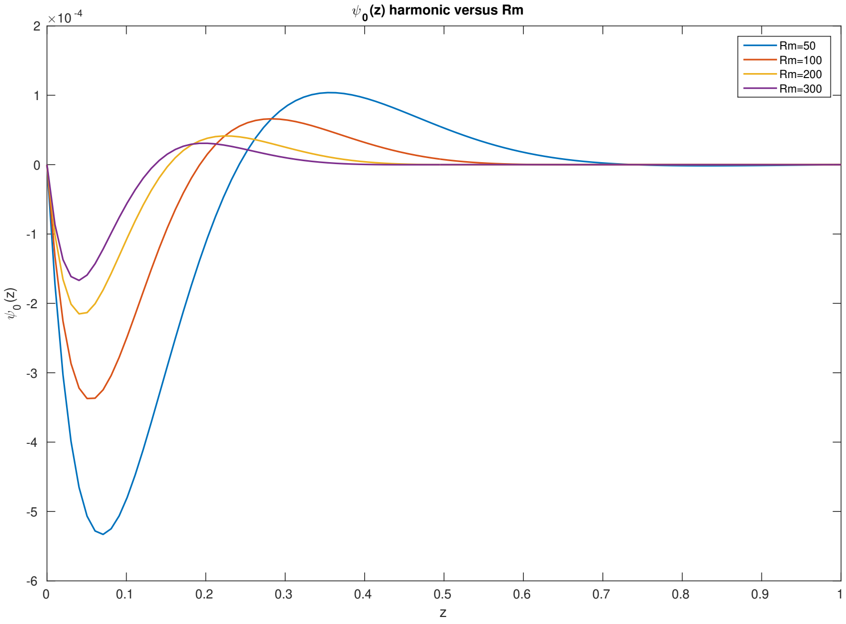

Figure 6.7: z-structure of $\psi_0\left(z\right)$ with increasing Rm. The boundary layer thickness decreases with Rm as well as the size of the minima.

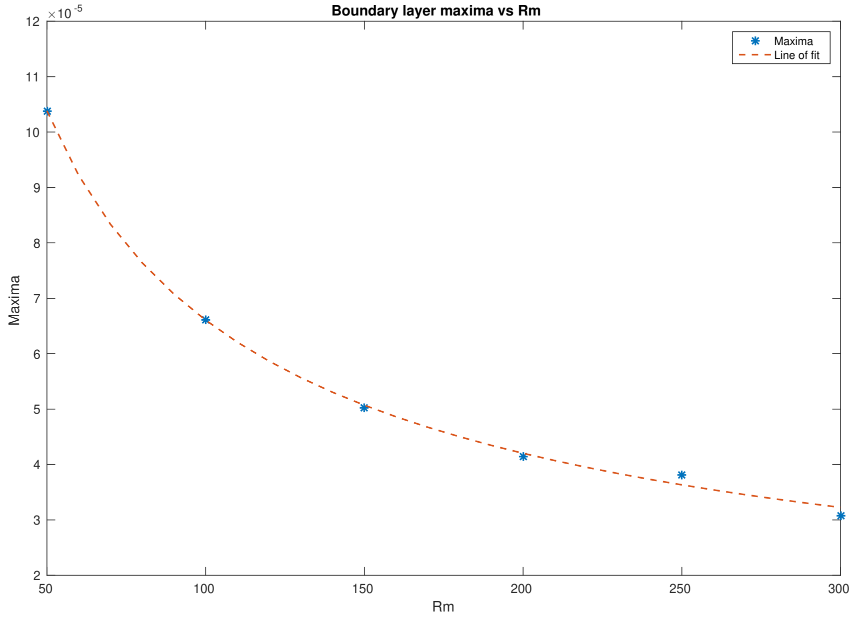

Figure 6.8: Maxima of $\psi_0\left(z\right)$ with Rm. Assuming a fit of $\sigma \mathrm{Rm}^{\beta}$ gives $\sigma = 1.333 \times 10^{-3}$ and $\beta = -0.6525$.

6.3 Viscous flow moderate Rm

An extensive parameter space search was conducted for $(\mathrm{Rm}, \mathrm{Ha}) = 0 \to 100$. Generally most of the solutions were quite "easy" to find in the sense that there was no singular behaviour found at finite values of the parameter space covered. It is not practical or possible to show every possible solution at every possible parameter value, so we are selective with how we display our results. We first show a general overview of $v_x\left(x, z\right)$ in parameter space by measuring the root-mean square speed,

$$v_{rms} = \sqrt{\frac{1}{N_x N_z} \sum_{i=1}^{N_x} \sum_{j=1}^{N_z} v_x^2\left(x_i, z_j\right)}. \tag{6.1}$$

where N_x and N_z are the number of mesh points in the x and z direction. The choice of combining both the ageostrophic and geostrophic parts is to ensure that this choice is independent of the boundary condition on the ageostrophic component of $v\left(x, z\right)$ as mentioned in §5.2.2.

Figure 6.9 plots v_{rms} of $v_x\left(x, z\right)$, given by (6.1), for fixed values of Rm with increasing Hartmann number. There is a non-monotonic relationship with Ha throughout the selected values of Rm, which highlights three regimes of viscosity to discuss: dominant viscosity $\mathrm{Ha} < 0.1$, moderate viscosity $1 < \mathrm{Ha} < 10$ and weak viscosity $\mathrm{Ha} > 10$.

It can be seen in figure 6.9 that v_{rms} does not become large with increasing Ha for moderate values of Rm. As expected, v_{rms} should become large in the singular limit of $\mathrm{Rm} \to 0$ and $\mathrm{Ha} \to \infty$, as seen in the blue line of figure 6.9. The moderate values of Rm, given by the yellow, purple and green lines, further support the notion that the geostrophic flow is no longer singular for finite values of Rm.

In figures 6.10 to 6.13, an overview of Ha-Rm space is provided for $V_0'\left(x\right)$, $v_x\left(x, z\right)$, $H\left(x, z\right)$ and $\psi\left(x, z\right)$, showing the behaviour of the solutions for the extreme values and also a quick glance at the intermediate values.

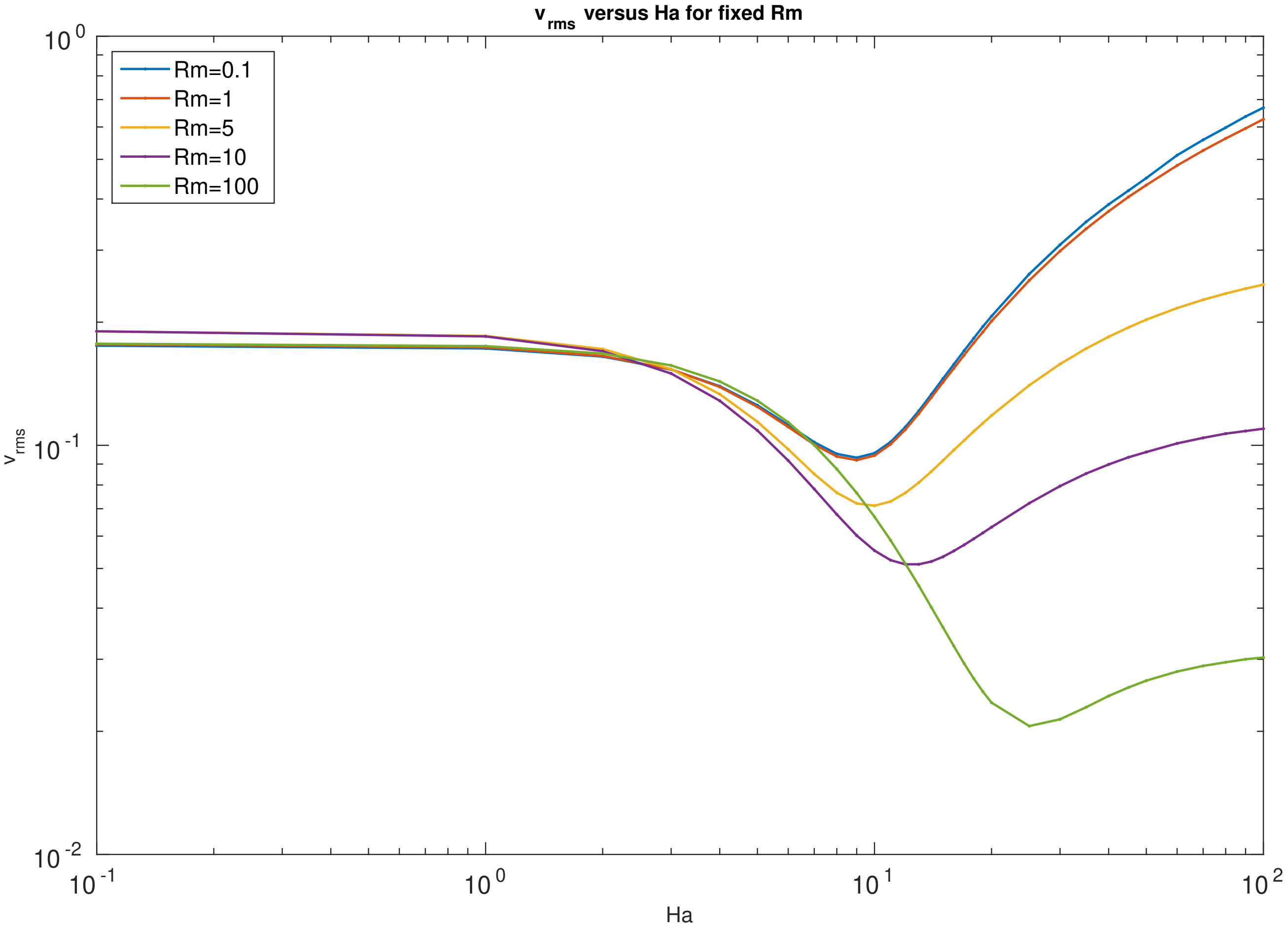

Figure 6.9: v_{rms} with increasing Ha.

6.3.1 Dominant viscosity $\mathrm{Ha} \ll 1$

In the dominant viscous limit, $\mathrm{Ha} \to 0$, there is a wide variety of behaviour with Rm amongst the four quantities studied, these being, $A(x,z)$, $v(x,z)$, $H(x,z)$ and $\psi(x,z)$. On the basis of the results presented in figures 6.10-6.13 we develop an asymptotic theory in this limit in section 7.1 below. As $\mathrm{Rm} \to 0$, the geostrophic flow and the geostrophic meridional field are noticeably smaller in magnitude than the corresponding solutions found in the inviscid regime. In figure 6.13, the contour plot of the stream function for $\mathrm{Rm} \to 0$ and $\mathrm{Ha} = 0.1$ has no azimuthal dependence, which strongly suggests that both the geostrophic flow and meridional field are in fact zero in the $\mathrm{Ha} \to 0$ limit. If viscosity dominates, then (5.5) is approximated by

$$\frac{\partial \psi}{\partial z} = \frac{1}{\mathrm{Ha}^2} \nabla^2 v. \tag{6.2}$$

If the right hand side of (6.2) is purely a function of z, as the numerics suggest, then clearly $V_0'(x) \to 0$ as $\mathrm{Ha} \to 0$, as seen in figure 6.10.

From 6.10 it can be seen that as Rm increases in the dominant viscous regime (refer to the $\mathrm{Ha} = 0.1$ column) the amplitude of the geostrophic flow is no longer small and hence begins to have an influence on the azimuthal dependence of $\psi(x,z)$, as seen in the corresponding plots of figure 6.13. Consequently, the stream function takes the form of cellular-like patterns with π-periodicity. The magnitude of the stream function is doubled between $\mathrm{Rm} \to 0$ to $\mathrm{Rm} = 100$.

There is little variation in the average speed of $v_x(x,z)$ in the dominant viscosity regime even when Rm generates non-zero $V_0'(x)$. This is countered by the change in the ageostrophic meridional flow. Changing Rm leads to changes in the structure of ageostrophic $v(x,z)$ (see figure 6.2) but does not have much effect on its v_{rms}.

6.3.2 Moderate viscosity $\mathrm{Ha} \sim \mathcal{O}(1)$

Away from the dominant viscosity limit, where $\mathrm{Ha} \sim \mathcal{O}(1)$, the geostrophic flow is no longer negligible and appears to take the form of a $\sin(2kx)$ function at $\mathrm{Ha} = 1$. In this region of parameter space the Jacobian term plays an influence in the stream function equation. The azimuthal dependence of the meridional field is linked with the geostrophic flow, and hence this dependence manifests itself in the contours of $\psi(x, z)$ as the Hartmann number becomes order 1. At the same time, there is a decrease in the magnitude of $\psi(x, z)$ on leaving the dominant viscous regime.

For more moderate values, Ha $= 1 \rightarrow 10$, there is a shift in the structure of $V_0'(x)$ and a rapid transition to cellular patterns in $\psi(x, z)$, due to the fact that the viscous term scales as Ha^{-2}. In figure 6.10, the geostrophic flow at moderate Ha has elements of the singular behaviour found at Ha $\rightarrow \infty$ and can be seen to have a tendency to shift to that singularity. Increasing Rm shifts this structure back to the well behaved solution found at large Rm.

6.3.3 Weak viscosity

A boundary layer forms in the geostrophic flow as we approach the inviscid limit of Ha $\rightarrow \infty$ when Rm is small. This is not so surprising as the geostrophic flow has to make the transition from a continuous solution in the viscous regime to the singular solution found in the asymptotic inviscid limit. An asymptotic theory to the viscous regime helps verify this behaviour as Ha $\rightarrow \infty$ for Rm $\rightarrow 0$; this is considered in §7.3.

For moderate values of Rm, the boundary layer begins to disappear, as can be seen in figure 6.10 for Ha $= 100$. It is clear that Rm $= 1$ is not large enough to remove the singularity, whilst Rm $= 10$ seems to be a critical point in which the transition away from the boundary layer begins. At Rm $= 100$ the solution is well behaved for Ha $= 100$; the reason for this well-behaved solution at large Rm is discussed in §6.2.1.

The v_{rms} begins to slow down in the transition from moderate to weak viscosity, as seen in figure 6.9. The location of the minima for v_{rms} moves to higher Ha as Rm is increased. The values of Rm plotted all display non-monotonic behaviour in v_{rms}, although the reason for this is not so clear. This non-monotonic nature may not always be the case for Rm > 100, as figure 6.9 suggests that this larger Rm may in fact have monotonically decreasing behaviour.

For weak viscosity, figure 6.12 shows that the meridional field has two regions of opposite polarity between the bottom and the top of the layer (Ha = 100). This is a distinct feature of the weakly viscous regime for the meridional field as smaller values of Ha do not display this behaviour. Increasing Rm results in both the compression of the field into the lower half of the domain, and the shearing of the field in x.

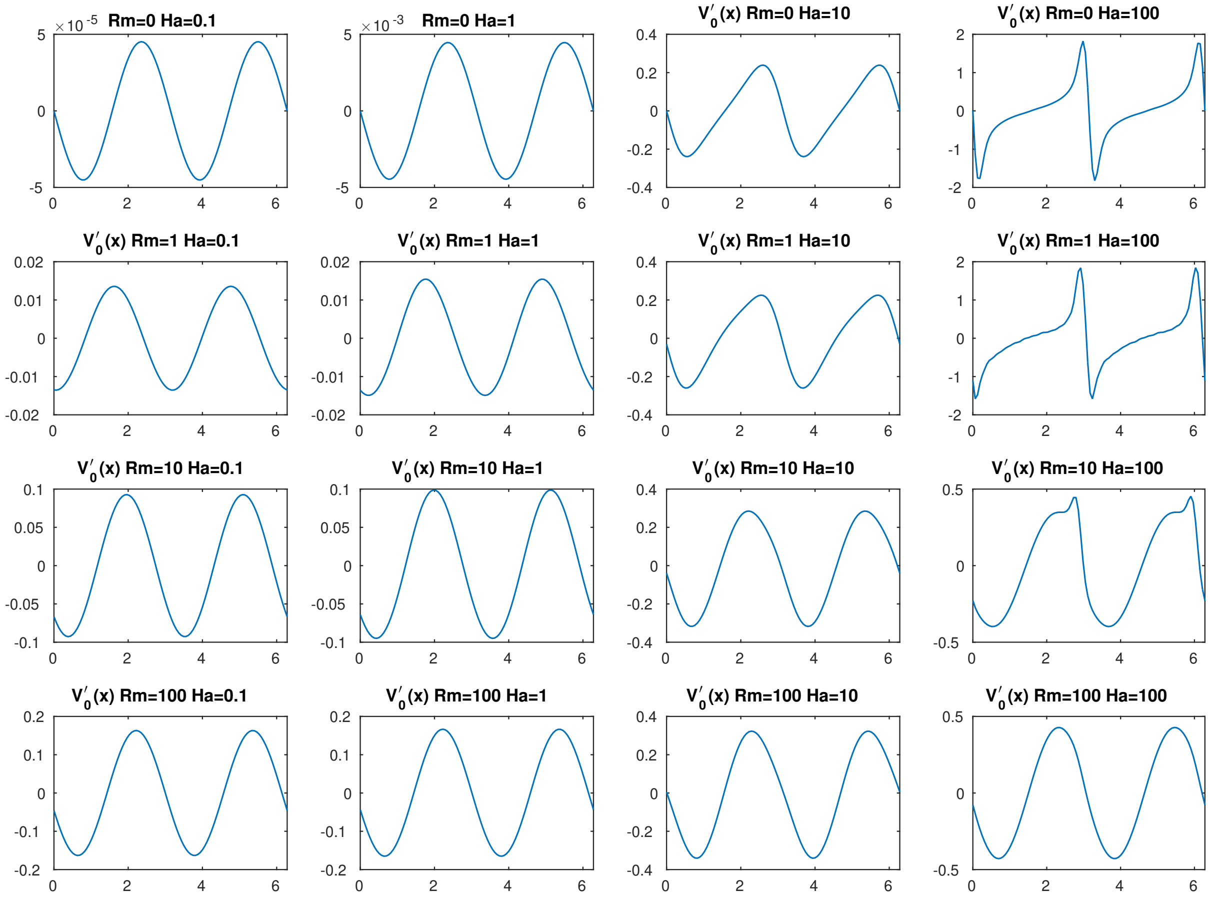

Figure 6.10: An overview of Rm-Ha space for the geostrophic flow.

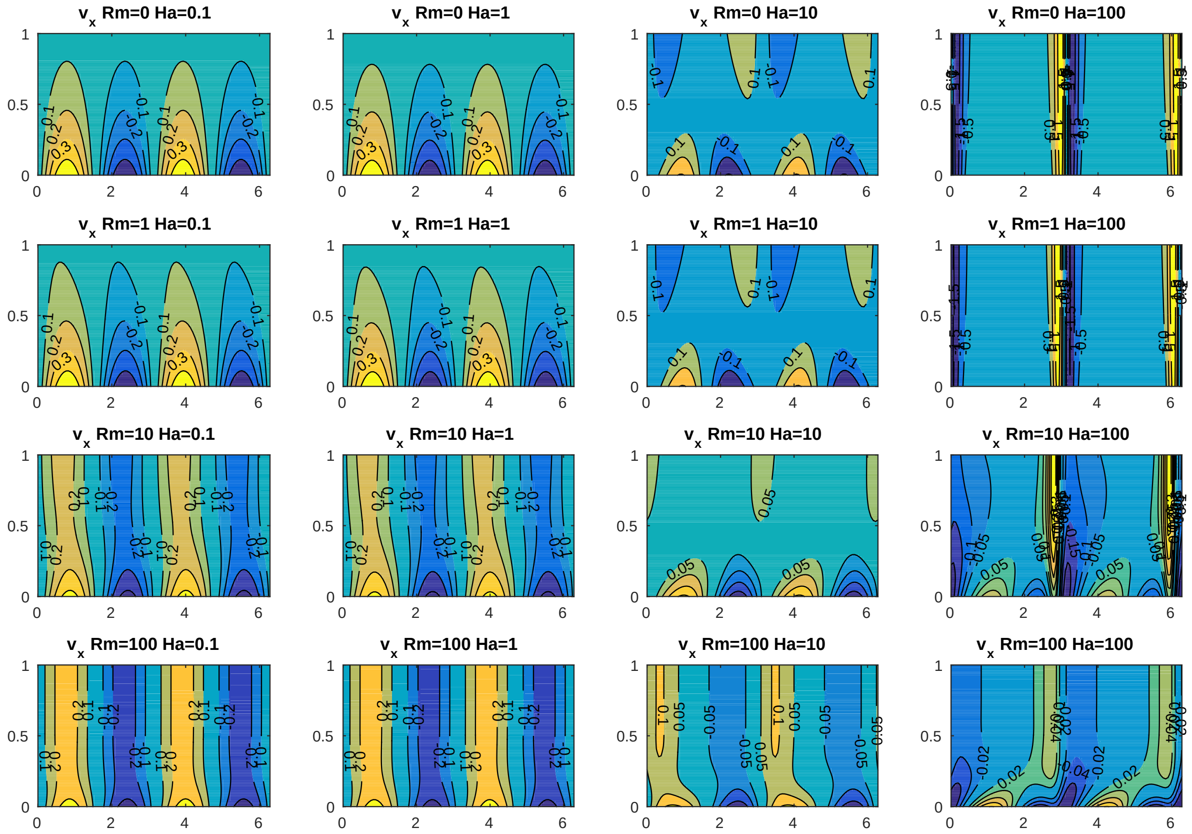

Figure 6.11: An overview of Rm-Ha space for $v_x\left(x,z\right)$.

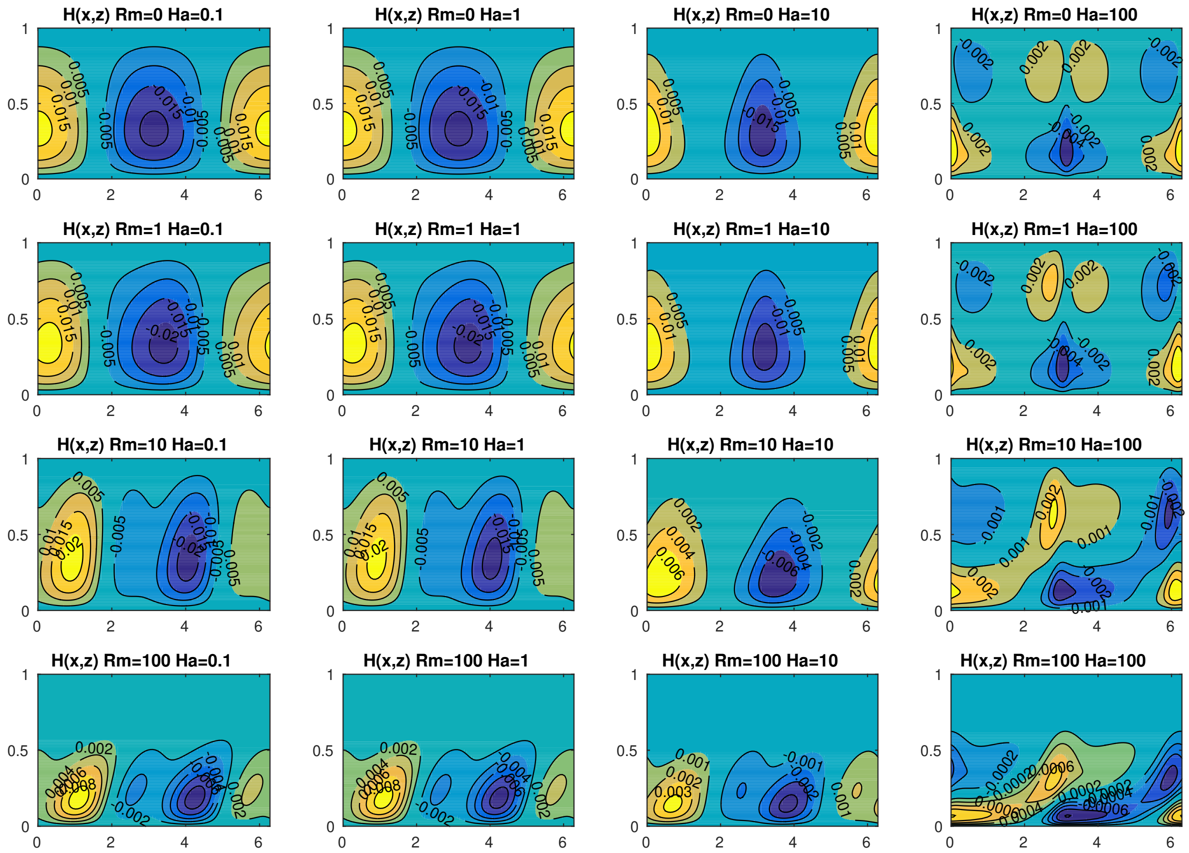

Figure 6.12: An overview of Rm-Ha space for the meridional field.

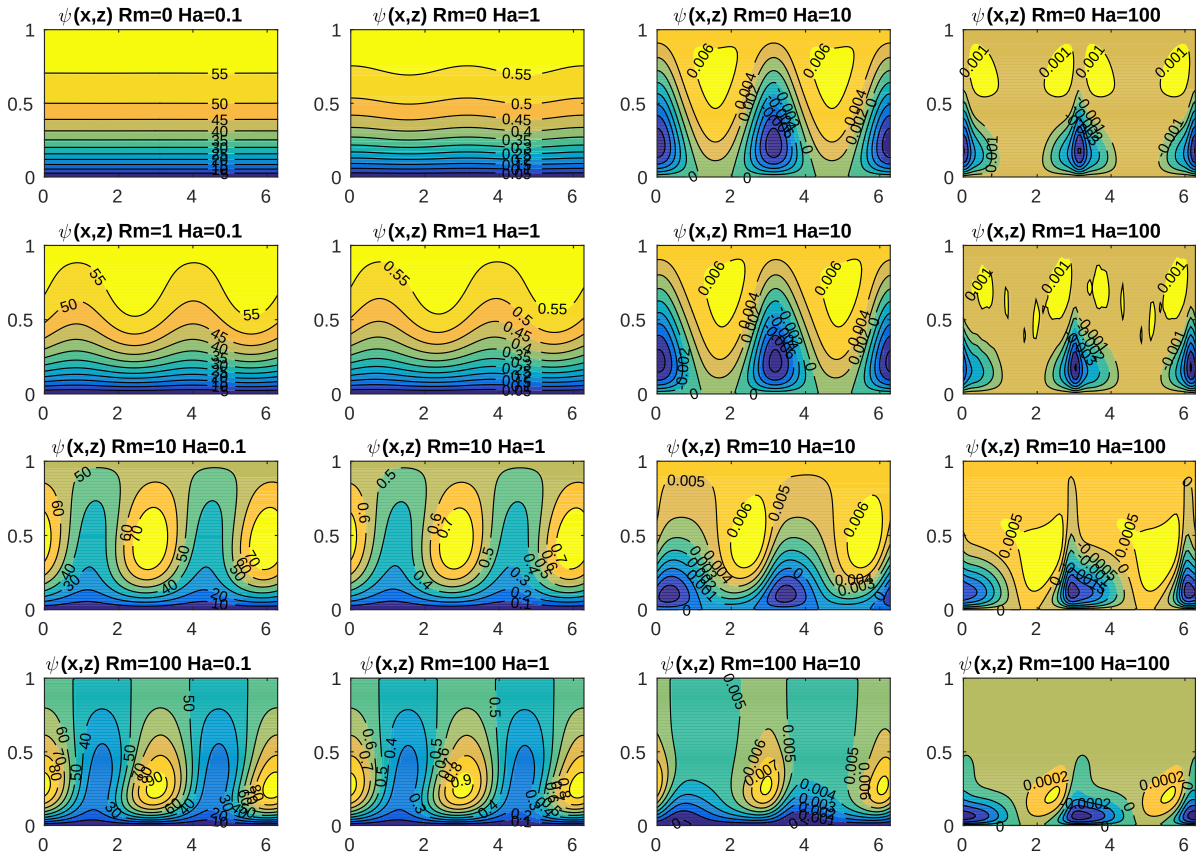

Figure 6.13: An overview of Rm-Ha space for the stream function.

6.4 Estimates for flow speeds in Saturn

In reality the Ekman number is extremely small in Saturn ($\mathrm{E_k} \sim 10^{-15}$) and the Elsasser number is of order unity (Christensen & Wicht, 2008). To achieve Ekman numbers of a planetary value would require the Hartmann number to be of order $\mathrm{Ha} \sim 10^7 - 10^8$; this is difficult to achieve even with today's computational power owing to the small scale structures that would be required to resolve the boundary layer. Although we have not calculated solutions in which the Elsasser number is of order unity, typical flow speeds can be calculated from our calculated u_{rms} to see how they compare with the estimates for the meridional flow.

To apply our numerical results to Saturn we derive estimates for the flow speeds expected within the stratified layer. These are calculated from observational evidence and other estimated values which give a rough value for what is expected. The thermal shear in the layer is driven by a pole-equator temperature difference, which is proposed as 10^{-4}K over a range of $d \sim 3 \times 10^6$m, suggested by Stevenson (1982b). Over the whole distance of $55,000$km between the pole and equator this would give a temperature difference of 2×10^{-3}K. The rotation rate of Saturn is given by $\Omega_0 = 1.6 \times 10^{-4}\mathrm{s}^{-1}$, the gravity and coefficient of thermal expansion are $g = 11\mathrm{ms}^{-2}$ and $\alpha = 1 \times 10^{-4}\mathrm{K}^{-1}$. For Saturn the magnetic diffusivity is approximately $\eta = 2\mathrm{m}^2\mathrm{s}^{-1}$.

As a result, the thermal wind given by (3.15), where γ is defined as (3.16), can be estimated to be

$$\gamma \sim \frac{g\alpha T'}{2\Omega_0} \sim 10^{-10}\mathrm{s}^{-1}. \tag{6.3}$$

From (6.3) this gives a typical value of Rm as approximately

$$\mathrm{Rm} \sim \frac{\gamma d^2}{\eta} \sim 450. \tag{6.4}$$

This value suggests that the non-axisymmetric component is reduced by a factor of 10^{-4}, which is roughly consistent with Cassini data. If the non-axisymmetric field in the dynamo region were comparable with the axisymmetric field, after attenuation the non-axisymmetric field would be 10^{-4} times smaller.

In table 6.1, the u_{rms} values are calculated for the meridional flow. The u_{rms} tend to the approximate value of 4×10^{-3} at large Rm. This can be converted into physical dimensions via (**??**), i.e.

$$v \sim \mathrm{Rm}\frac{\eta}{d}\Lambda\tilde{v} \sim \gamma d\Lambda\tilde{v}, \tag{6.5}$$

where we assume $\Lambda = 1$, an appropriate value for Saturn. The resulting velocity is then $v \sim 10^{-6}\mathrm{ms}^{-1}$, which is a small velocity compared to the size of Saturn and the observed surface speeds. The calculated velocity has a turnover time $d/v \sim 3 \times 10^{12}\mathrm{s}$ or approximately 100,000 years. This means that the meridional circulation will not be visible on timescales for which we can observe Saturn. These velocities are significantly slower than the observed jets at the surface which can be up to $400\mathrm{ms}^{-1}$ (Liu *et al.*, 2008). This means that there is a rapid increase in velocity towards the upper parts of the atmosphere of Saturn.

The temperature difference of $T \sim 10^{-4}\mathrm{K}$ can also be independently derived from the heat flux. Convective velocities in Jupiter have been estimated at $10^{-3}\mathrm{ms}^{-1}$ (Ridley & Holme, 2016) and it is reasonable to assume such a value would also be the case for Saturn. Heat flux that is transported by convection is given by

$$F = \rho c_p U T, \tag{6.6}$$

with units Wm^{-2}, where ρ is the density ($\rho \sim 10^3\mathrm{kgm}^{-3}$), c_p is the specific heat ($c_p \sim 1.5 \times 10^4\mathrm{Jkg}^{-1}\mathrm{K}^{-1}$), U is the convective velocity ($U \sim 10^{-3}\mathrm{ms}^{-1}$) and T is the temperature fluctuation (with $T \sim 10^{-4}\mathrm{K}$). These values would give a heat flux of $F \sim 1.5\mathrm{Wm}^{-2}$, which is very close to the observational value of $2\mathrm{Wm}^{-2}$ (Hanel *et al.*, 1983). This supports a typical temperature fluctuation of $10^{-4}\mathrm{K}$ in a convecting region and our calculation suggests that this is also the case in the stably stratified layer.

In the table below we sample u_{rms} speeds for the meridional flow $v\,(x, z)\,\hat{\boldsymbol{y}}$ for varying Rm, including Rm $= 450$, in order to see how our numerical result compares with velocity estimates. At Rm $= 450$ the u_{rms} converts to a meridional flow speed of $4.3 \times 10^{-6}\mathrm{ms}^{-1}$, which is the correct order of magnitude of what is expected in the stable layer.

We note that although computational attempts at higher Rm have been performed, we have omitted them from the table owing to the difficulty in resolving the solution.

Rm	u_{rms}	Velocity (ms^{-1})
1×10^1	0.1098	7.57×10^{-7}
5×10^1	0.0399	1.37×10^{-6}
1×10^2	0.0303	2.10×10^{-6}
4.5×10^2	0.0161	4.83×10^{-6}
1×10^3	0.0114	7.86×10^{-6}
3×10^3	0.0062	1.28×10^{-5}
5×10^3	0.0047	1.62×10^{-5}
7×10^3	0.0042	2.03×10^{-5}
1×10^4	0.0041	2.83×10^{-5}

Table 6.1: The u_{rms} values and corresponding meridional velocity for Saturn for increasing Rm.

Chapter 7

Incorporating viscosity: an asymptotic approach

In this chapter we incorporate viscosity into an asymptotic analysis for our model. There are two regimes to consider: one where viscosity is small, corresponding to $\mathrm{Ha} \gg 1$, and one where viscosity is large, corresponding to $\mathrm{Ha} \ll 1$. The numerical results of Chapter 6 can then be compared to see if the observed behaviour is also confirmed in an analytical framework.

7.1 Viscous model equations

When viscosity is considered, the governing equations become

$$\frac{\partial^2 A}{\partial x^2} + \frac{\partial^2 A}{\partial z^2} = \mathrm{Rm} z \frac{\partial A}{\partial x}, \tag{7.1}$$

$$J_y = -z \frac{\partial A}{\partial z}, \tag{7.2}$$

$$\frac{\partial v}{\partial z} = \frac{\partial \left(J_y, A\right)}{\partial \left(x, z\right)}, \tag{7.3}$$

$$\frac{\partial^2 H}{\partial x^2} + \frac{\partial^2 H}{\partial z^2} = \frac{\partial \left(v, A\right)}{\partial \left(x, z\right)} + \mathrm{Rm} z \frac{\partial H}{\partial x}, \tag{7.4}$$

$$\frac{\partial \psi}{\partial z} = \frac{\partial \left(H, A\right)}{\partial \left(x, z\right)} - \frac{1}{\mathrm{Ha}^2} \left(\frac{\partial^2 v}{\partial x^2} + \frac{\partial^2 v}{\partial z^2} \right). \tag{7.5}$$

There is a new $\mathrm{Ha}^{-2} \nabla^2 v$ term in equation (7.5). As in Chapter 4, we shall again assume Rm is small. We thus have the expressions (4.6)–(4.10), giving the following leading order equations in Rm,

$$\frac{\partial^2 A}{\partial x^2} + \frac{\partial^2 A}{\partial z^2} = 0, \tag{7.6}$$

$$J_y = -z\frac{\partial A}{\partial z}, \tag{7.7}$$

$$\frac{\partial v}{\partial z} = \frac{\partial \left(J_y, A\right)}{\partial \left(x, z\right)}, \tag{7.8}$$

$$\frac{\partial^2 H}{\partial x^2} + \frac{\partial^2 H}{\partial z^2} = \frac{\partial \left(v, A\right)}{\partial \left(x, z\right)}, \tag{7.9}$$

$$\frac{\partial \psi}{\partial z} = \frac{\partial \left(H, A\right)}{\partial \left(x, z\right)} - \frac{1}{\mathrm{Ha}^2}\left(\frac{\partial^2 v}{\partial x^2} + \frac{\partial^2 v}{\partial z^2}\right). \tag{7.10}$$

Usually, the inclusion of viscosity requires additional no slip boundary conditions; this analysis is somewhat peculiar as we do not require any viscous boundary conditions since the highest derivative in ψ is second order in equations (7.6)–(7.10). Taylor's constraint is used to determine the arbitrary geostrophic part, $V_0\left(x\right)$, in (7.8). In a finite Elsasser number regime we would require the additional no slip boundary conditions since the $\Lambda^2\mathrm{Ha}^{-2}\nabla^4\psi$ term would come into (7.8), and so we would then require four boundary conditions on ψ and hence the additional no slip condition.

We present the solution to two asymptotic regimes: one where Ha is small (viscosity is dominant) and one where Ha is large, i.e. approaching the inviscid limit.

7.2 Small Ha analysis

7.2.1 Asymptotic approach

By introducing viscosity one expects that the viscous term will smooth out the steep gradients found near the singularity and hence a smooth, continuous solution can be found for the geostrophic flow. The inclusion of viscosity does not change the solution to A, J_y and the ageostrophic part of v. This is because terms involving Ha do not appear in their corresponding ODEs. As a result, ODEs (7.6), (7.7) and (7.8) have the same solution as found in the analysis of Chapter 4, namely

$$A\left(x,z\right)=\frac{1}{k}\sin\left(kx\right)e^{-kz}, \tag{7.11}$$

$$J_y\left(x,z\right)=-z\cos\left(kx\right)e^{-kz}, \tag{7.12}$$

$$v\left(x,z\right)=-\frac{1}{4k}e^{-2kz}\cos\left(2kx\right)+\frac{1}{2}ze^{-2kz}+V_0\left(x\right). \tag{7.13}$$

What does change though are the solutions to $V_0\left(x\right)$, $H\left(x,z\right)$ and $\psi\left(x,z\right)$. If $\mathrm{Ha}\ll 1$, then at leading order in Ha, (7.10) becomes

$$\frac{\partial\psi}{\partial z}=-\frac{1}{\mathrm{Ha}^2}\left(\frac{\partial^2 v}{\partial x^2}+\frac{\partial^2 v}{\partial z^2}\right). \tag{7.14}$$

This is due to the term $\frac{\partial(H,A)}{\partial(x,z)}$ being $\mathcal{O}\left(1\right)$ and much smaller than $\mathrm{Ha}^{-2}\nabla^2 v$ at leading order. By inspection of (7.14), one can see that we have the asymptotic expansion

$$\psi\left(x,z\right)=\frac{1}{\mathrm{Ha}^2}\psi^{(0)}\left(x,z\right)+\psi^{(1)}\left(x,z\right)+\mathrm{Ha}^2\psi^{(2)}\left(x,z\right)+\mathcal{O}\left(\mathrm{Ha}^4\right). \tag{7.15}$$

On substituting the expansion (7.15) into (7.14), the leading order term $\psi^{(0)}\left(x,z\right)$ has solution,

$$\psi^{(0)}\left(x,z\right)=-\frac{1}{\mathrm{Ha}^2}\left(\frac{1}{2}e^{-2kz}-kze^{-2kz}\right)-\frac{1}{\mathrm{Ha}^2}\frac{\mathrm{d}^2V_0}{\mathrm{d}x^2}z+\hat{k}\left(x\right). \tag{7.16}$$

Imposing the condition $\psi=0$ at $z=0$ gives

$$\hat{k}\left(x\right)=\frac{1}{\mathrm{Ha}^2}\frac{1}{2}. \tag{7.17}$$

We also require $\psi=$ constant at $z=1$, which gives

$$\frac{\partial}{\partial x}\psi^{(0)}\left(x,1\right)=-\frac{1}{\mathrm{Ha}^2}\frac{\partial}{\partial x}\left(\frac{\mathrm{d}^2V_0}{\mathrm{d}x^2}\right)=0, \tag{7.18}$$

implying

$$\frac{\mathrm{d}^2V_0}{\mathrm{d}x^2}=\mathrm{const.} \tag{7.19}$$

Since $V_0\left(x\right)$ should be periodic the constant in (7.19) should be zero. $V_0\left(x\right)$ itself can be a constant as this just adds a constant to the overall solution of the system of equations; however the derivatives of $V_0\left(x\right)$ will be zero. This confirms the numerical result of the geostrophic velocity being negligible when $\mathrm{Ha}=0.1$ and $\mathrm{Rm}\to 0$ in Chapter 6 . As a result, the solution to $\psi\left(x,z\right)$ at leading order is

$$\psi^{(0)}\left(x,z\right)=-\frac{1}{\mathrm{Ha}^2}\left[\frac{1}{2}\left(e^{-2kz}-1\right)-kze^{-2kz}\right]. \tag{7.20}$$

To determine the next order term in $\psi\left(x,z\right)$ we expand the geostrophic flow as an asymptotic series in Ha,

$$V_0\left(x\right) = V_0^{(0)}\left(x\right) + \mathrm{Ha}^2 \hat{V}_0\left(x\right) + \mathcal{O}\left(\mathrm{Ha}^4\right). \tag{7.21}$$

Since the leading order solution for $V_0\left(x\right)$ is zero, this becomes $V_0\left(x\right) = \mathrm{Ha}^2\hat{V}_0\left(x\right)$ on ignoring the higher order Ha terms. The meridional field is expressed in terms of its ageostrophic and geostrophic parts as

$$H\left(x,z\right) = H^a\left(x,z\right) + H^g\left(x,z\right), \tag{7.22}$$

where the solution to $H^a\left(x,z\right)$ is recovered from (4.23) and (4.26), i.e.

$$\begin{aligned} H^a\left(x,z\right) &= \left[\alpha_0 \sinh\left(kz\right) + \alpha_1 \cosh\left(kz\right) + \frac{1}{8k}\left(z - \frac{1}{4k}\right)e^{-3kz}\right]\cos\left(kx\right) && \text{(7.23a)} \\ &= h_a\left(z\right)\cos\left(kx\right), && \text{(7.23b)} \end{aligned}$$

where α_0 and α_1 are given by (4.27) and (4.28). The geostrophic component of (7.23a), $H^g\left(x,z\right)$, when substituted into (7.9), satisfies

$$\frac{\partial^2 H^g}{\partial x^2} + \frac{\partial^2 H^g}{\partial z^2} = \mathrm{Ha}^2 \frac{\mathrm{d}\hat{V}_0}{\mathrm{d}x}\frac{\partial A}{\partial z}. \tag{7.24}$$

Equation (7.24) implies that $H^g\left(x,z\right)$ is now small compared to $H^a\left(x,z\right)$ due to it being $\mathcal{O}\left(\mathrm{Ha}^2\right)$. At $\mathcal{O}\left(1\right)$ we can calculate the next order solution for $\psi\left(x,z\right)$. Substituting (7.11) and (7.23b) into (7.10) gives

$$\begin{aligned} \frac{\partial \psi^{(1)}}{\partial z} =& \frac{k}{2}e^{-kz}h_a\left(z\right) - \frac{1}{2}h_a'\left(z\right)e^{-kz} \\ &- \cos\left(2kx\right)\left[\frac{k}{2}e^{-kz}h_a\left(z\right) + \frac{1}{2}e^{-kz}h_a'\left(z\right)\right] - \frac{\mathrm{d}^2\hat{V}_0}{\mathrm{d}x^2}, \end{aligned} \tag{7.25}$$

which can be expressed as

$$\frac{\partial \psi^{(1)}}{\partial z} = -\frac{1}{2}\frac{\mathrm{d}}{\mathrm{d}z}\left(h_a e^{-kz}\right) - \frac{1}{2}\cos\left(2kx\right)\left[\frac{\mathrm{d}}{\mathrm{d}z}\left(h_a e^{-kz}\right) + 2kh_a e^{-kz}\right] - \frac{\mathrm{d}^2\hat{V}_0}{\mathrm{d}x^2}. \tag{7.26}$$

Integrating (7.26) over the layer and using the boundary conditions $\psi = 0$ on $z = 0$ and $\psi =$ constant on $z = 1$ yields

$$\frac{\mathrm{d}^2\hat{V}_0}{\mathrm{d}x^2} = -\cos\left(2kx\right)\int_0^1 ke^{-kz}h_a\left(z\right)\mathrm{d}z. \tag{7.27}$$

Evaluating (7.27) gives,

$$\hat{V}_0''(x) = -\frac{1}{4}\left[\alpha_1\left(1+2k-e^{-2k}\right) - \alpha_0\left(1-2k-e^{-2k}\right) - \frac{1}{8k}e^{-4k}\right]\cos(2kx)\,. \tag{7.28}$$

Integrating (7.28) then gives,

$$V_0'(x) = -\frac{1}{8k}\left[\alpha_1\left(1+2k-e^{-2k}\right) - \alpha_0\left(1-2k-e^{-2k}\right) - \frac{1}{8k}e^{-4k}\right]\sin(2kx)\,. \tag{7.29}$$

The constant of integration is zero as $V_0'(x)$ is periodic in the domain x. Equation (7.29) is the derivative of the geostrophic velocity in the dominant viscous regime and is plotted in figure 7.1. The singularity has been removed at small Ha.

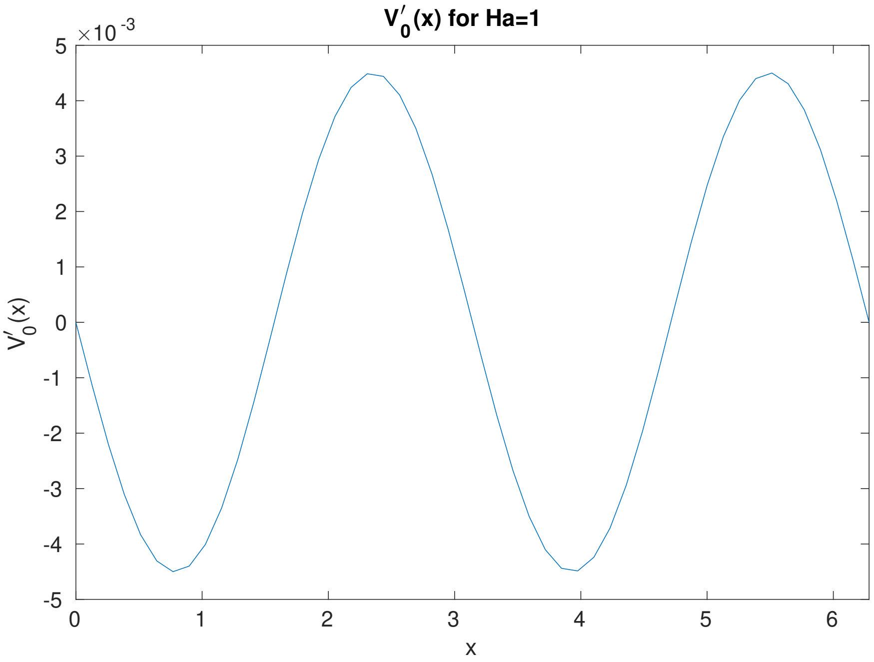

Figure 7.1: Plot of (7.29) for $k = 1$.

Finally, we can evaluate the first order correction to the stream function by integrating (7.26), which gives

$$\begin{aligned}\psi^{(1)}(x,z) = &-\frac{1}{2}h_a(z)\,e^{-kz} - z\hat{V}_0''(x)\\ &-\frac{1}{2}\cos(2kx)\left[h_a(z)\,e^{-kz} + 2k\int_0^z h_a(z')\,e^{-kz'}\mathrm{d}z\right]\end{aligned} \tag{7.30}$$

which, by construction, satisfies $\psi(x,0) = 0$. The $\mathcal{O}(1)$ correction to $\psi(x,z)$ is therefore evaluated by substituting (7.23a) into (7.30) and hence,

$$\begin{aligned}
\psi^{(1)}(x,z) = &-\frac{1}{2}\left(\alpha_0 \sinh(kz)\, e^{-kz} + \alpha_1 \cosh(kz)\, e^{-kz} + \frac{1}{8k}\left(z - \frac{1}{4k}\right) e^{-4kz}\right.\\
&+ \cos(2kx)\left[\alpha_0\left(\frac{1}{4} - \frac{1}{4}e^{-2kz} - \frac{1}{2}\sinh(kz)\, e^{-kz} - \frac{k}{2}z\right)\right.\\
&+\alpha_1\left(\frac{1}{4}e^{-2kz} - \frac{1}{4} - \frac{k}{2}z - \frac{1}{2}\cosh(kz)\, e^{-kz}\right)\\
&+\frac{1}{32k}ze^{-4kz} - \frac{1}{16k}\left(z - \frac{1}{4k}\right)e^{-4kz}\\
&\left.\left.+z\left(\frac{1}{4}(\alpha_1 - \alpha_0) + \frac{1}{4}\alpha_0 e^{-2k} - \frac{1}{4}\alpha_1 e^{-2k} + \frac{k}{2}(\alpha_0 + \alpha_1) - \frac{1}{32k}e^{-4k}\right)\right]\right. .
\end{aligned} \tag{7.31}$$

The penultimate term (the coefficient of z) is the geostrophic contribution. Combining (7.20) and (7.31) gives

$$\begin{aligned}
\psi(x,z) = &-\frac{1}{\mathrm{Ha}^2}\left[\frac{1}{2}\left(e^{-2kz} - 1\right) - kze^{-2kz}\right]\\
&-\frac{1}{2}\left(\alpha_0 \sinh(kz)\, e^{-kz} + \alpha_1 \cosh(kz)\, e^{-kz} + \frac{1}{8k}\left(z - \frac{1}{4k}\right) e^{-4kz}\right.\\
&+ \cos(2kx)\left[\alpha_0\left(\frac{1}{4} - \frac{1}{4}e^{-2kz} - \frac{1}{2}\sinh(kz)\, e^{-kz} - \frac{k}{2}z\right)\right.\\
&+\alpha_1\left(\frac{1}{4}e^{-2kz} - \frac{1}{4} - \frac{k}{2}z - \frac{1}{2}\cosh(kz)\, e^{-kz}\right)\\
&+z\left(\frac{1}{4}(\alpha_1 - \alpha_0) + \frac{1}{4}\alpha_0 e^{-2k} - \frac{1}{4}\alpha_1 e^{-2k} + \frac{k}{2}(\alpha_0 + \alpha_1) - \frac{1}{32k}e^{-4k}\right)\\
&\left.\left.+\frac{1}{32k}ze^{-4kz} - \frac{1}{16k}\left(z - \frac{1}{4k}\right)e^{-4kz}\right]\right. + \mathcal{O}\left(\mathrm{Ha}^2\right),
\end{aligned} \tag{7.32}$$

which is plotted in figure 7.2. This completes the solution up to $\mathcal{O}(1)$ in $\psi(x,z)$ and $\mathcal{O}\left(\mathrm{Ha}^2\right)$ in $V_0'(x)$.

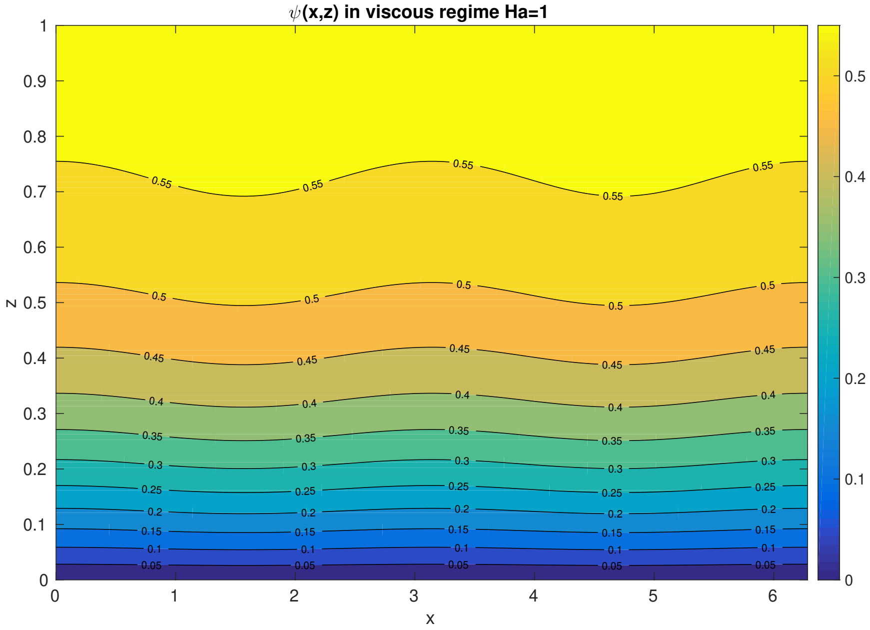

Figure 7.2: Contour plot of $\psi\left(x, z\right)$, given by (7.32), for $\mathrm{Ha}=1$ and $k=1$.

7.2.2 Numerical verification

In figure 7.3 the analytical solution to (7.20) is plotted along with the numerical solution. The numerical solution is provided from evaluating (5.37) at $\mathrm{Ha}=0.1$ in order to attain the small Ha limit. There is a good agreement between the two solutions for $\mathrm{Ha} \ll 1$ and $\mathrm{Rm} \rightarrow 0$.

In figure 7.4, we compare the analytical result (7.32) with the numerical solution by evaluating both (5.37) and (5.39). To obtain a comparison with the next order solution we set $\mathrm{Ha}=1$ in the numerical code. This is to ensure that the $\mathcal{O}\left(1\right)$ term is being considered. There is good agreement between the code and the asymptotic solution when $\mathrm{Ha}=1$.

The numerical solutions were resolved with a relatively low number of modes owing to the fact that the structure of $V_0'\left(x\right)$ is smooth and continuous. All solutions presented are for $k=1$.

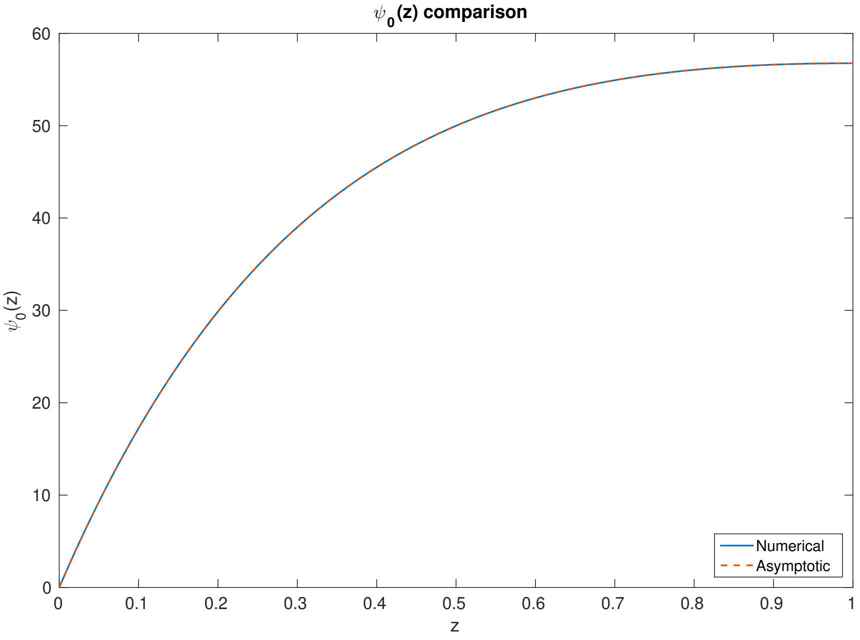

Figure 7.3: Comparison of (7.20) and (5.37) at $\mathrm{Ha} = 0.1$, $\mathrm{Rm} \to 0$ and $k = 1$.

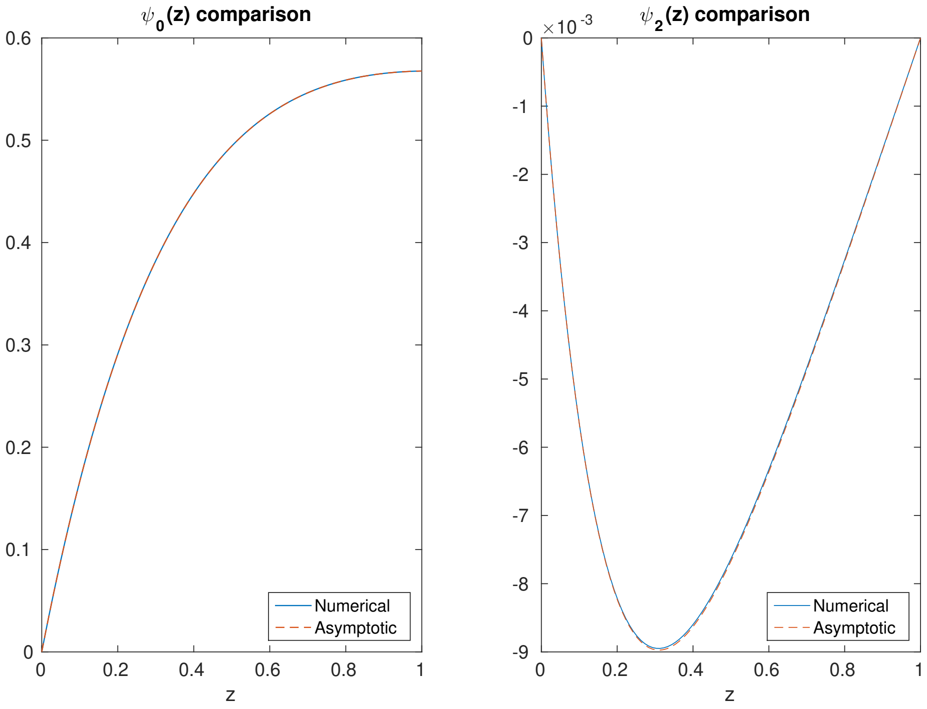

Figure 7.4: Comparison of (7.32) and both (5.37) and (5.39) at $\mathrm{Ha} = 1$, $\mathrm{Rm} \to 0$ and $k = 1$.

7.3 Large Ha analysis

In the inviscid regime (Ha formally infinite) we note that the geostrophic flow has solution (4.38), with singularities at $x = 0, \pi, 2\pi$, whilst in the small Ha regime the geostrophic flow is continuous across x. We anticipate that the transition from an inviscid to a weakly viscous fluid will be accommodated by the appearance of boundary layers in $V_0'(x)$ for Ha large but finite. Thus we introduce a stretched coordinate s, which will accommodate the transition to the boundary layer near $x = 0$,

$$s = \frac{x}{\varepsilon}, \tag{7.33}$$

where $\varepsilon \ll 1$ and where its dependence on Ha will emerge in the subsequent analysis. Throughout the whole domain, $A(x, z)$ and $J_y(x, z)$ have the exterior solution (7.11) and (7.12). However, $v(x, z)$ will change structure from inside to outside the boundary. Outside the boundary layer, $v(x, z)$ has the exterior solution (4.20)

$$v(x, z) = -\frac{1}{4k} e^{-2kz} \cos(2kx) + \frac{1}{2} z e^{-kz} + V_0(x), \tag{7.34}$$

where $V_0'(x)$ is given by (4.38). Inside the boundary layer

$$v(x, z) = -\frac{1}{4k} e^{-2kz} \cos(2kx) + \frac{1}{2} z e^{-kz} + V_1(s), \tag{7.35}$$

where $V_1(s)$ is the geostrophic flow inside the boundary layer. The inner and outer solutions are coupled by the matching principle, which states that

$$\lim_{x\to 0} V_0'(x) = \lim_{s\to\infty} \frac{\mathrm{d}}{\mathrm{d}x} V_1(s) = \lim_{s\to\infty} \frac{1}{\varepsilon} \frac{\mathrm{d}V_1}{\mathrm{d}s}. \tag{7.36}$$

Now

$$\frac{\mathrm{d}V_0}{\mathrm{d}x} = \tilde{V}_0 k \frac{\cos(kx)}{\sin(kx)} \to \frac{\tilde{V}_0}{x} \tag{7.37}$$

as $x \to 0$. Thus

$$\frac{\mathrm{d}V_0}{\mathrm{d}x} \to \frac{\tilde{V}_0}{x} = \frac{\tilde{V}_0}{s\varepsilon}. \tag{7.38}$$

Hence

$$\frac{\mathrm{d}V_1}{\mathrm{d}s} \to \frac{\tilde{V}_0}{s} \tag{7.39}$$

as $s \to \infty$. We note that by construction $V_1(s)$ is $\mathcal{O}(1)$ in the boundary layer.

Now consider equation (7.4) as Rm $\to$ 0,

$$\frac{\partial^2 H}{\partial x^2} + \frac{\partial^2 H}{\partial z^2} = \frac{\partial\left(v, A\right)}{\partial\left(x, z\right)}. \tag{7.40}$$

This holds in both the exterior and interior regions. Outside the boundary layer, we may express $H\left(x, z\right)$ as (7.22); as a result, (7.40) becomes

$$\frac{\partial^2 H^a}{\partial x^2} + \frac{\partial^2 H^a}{\partial z^2} + \frac{\partial^2 H^g}{\partial x^2} + \frac{\partial^2 H^g}{\partial z^2} = \frac{\partial v^a}{\partial x}\frac{\partial A}{\partial z} - \frac{\partial v^a}{\partial z}\frac{\partial A}{\partial x} + \frac{\mathrm{d}V_0}{\mathrm{d}x}\frac{\partial A}{\partial z}, \tag{7.41}$$

where v^a is the ageostrophic contribution of (7.34). $H^a\left(x, z\right)$ satisfies

$$\begin{aligned} \frac{\partial^2 H^a}{\partial x^2} + \frac{\partial^2 H^a}{\partial z^2} =& \frac{\partial v^a}{\partial x}\frac{\partial A}{\partial z} - \frac{\partial v^a}{\partial z}\frac{\partial A}{\partial x} \\ =& k e^{-3kz}\left(z - \frac{1}{k}\right)\cos\left(kx\right), \end{aligned} \tag{7.42}$$

with the solution to $H^a\left(x, z\right)$ given by (7.23b). The geostrophic part of $H\left(x, z\right)$ satisfies

$$\frac{\partial^2 H^g}{\partial x^2} + \frac{\partial^2 H^g}{\partial z^2} = -\tilde{V}_0 k \cos\left(kx\right) e^{-kz}, \tag{7.43}$$

with solution given by (4.41). Inside the boundary layer, we must take account of the boundary layer structure of the geostrophic flow. Thus equation (7.40) becomes

$$\frac{\partial^2 H}{\partial x^2} + \frac{\partial^2 H}{\partial z^2} = \frac{\partial v^a}{\partial x}\frac{\partial A}{\partial z} - \frac{\partial v^a}{\partial z}\frac{\partial A}{\partial x} + \frac{1}{\varepsilon}\frac{\mathrm{d}V_1}{\mathrm{d}s}\frac{\partial A}{\partial z}. \tag{7.44}$$

Inside the boundary layer we express the meridional field as

$$H\left(x, z\right) = H^a\left(x, z\right) + H^g\left(x, z\right) + \varepsilon^2 h\left(s, z\right), \tag{7.45}$$

where the expansion (7.45) is motivated by the numerical solutions. We note that since $h\left(s, z\right)$ is a function of s, we have

$$\left(\frac{\partial^2}{\partial x^2} + \frac{\partial^2}{\partial z^2}\right)\left(\varepsilon^2 h\left(s, z\right)\right) = \frac{\partial^2 h}{\partial s^2} + \mathcal{O}\left(\varepsilon^2\right). \tag{7.46}$$

Substituting (7.45) into (7.44) and using (7.43) gives

$$\frac{\partial^2 h}{\partial s^2} = \frac{1}{\varepsilon}\frac{\mathrm{d}V_1}{\mathrm{d}s}\frac{\partial A}{\partial z} + \tilde{V}_0 k \cos\left(kx\right) e^{-kz}. \tag{7.47}$$

Inside the boundary layer near $x = 0$ we note that

$$\cos\left(kx\right) = 1 - \frac{1}{2}k^2 x^2 + \ldots = 1 - \frac{\varepsilon^2}{2}k^2 s^2 + \ldots, \tag{7.48}$$

$$\frac{\partial A}{\partial z} = -\sin\left(kx\right) e^{-kz} = -k\varepsilon s e^{-kz} + \mathcal{O}\left(\varepsilon^3\right). \tag{7.49}$$

Hence

$$\frac{\partial^2 h}{\partial s^2} = \tilde{V}_0 k e^{-kz} - k e^{-kz} s \frac{\mathrm{d}V_1}{\mathrm{d}s} + \mathcal{O}\left(\varepsilon^2\right). \tag{7.50}$$

The obvious separable solution of (7.50) is

$$h\left(s,z\right) = k e^{-kz} h_1\left(s\right), \tag{7.51}$$

giving

$$\frac{\mathrm{d}^2 h_1}{\mathrm{d}s^2} = \tilde{V}_0 - s\frac{\mathrm{d}V_1}{\mathrm{d}s}. \tag{7.52}$$

The solution (7.51) however does not satisfy the boundary conditions $h\left(s,z\right) = 0$ on $z = 0$ and $z = 1$. Whilst (7.51) is valid away from the boundaries, additional boundary layer correction terms to $h\left(s,z\right)$ are needed in order to complete the solution. As shown in the next section, these boundary layer corrections play a significant rôle in determining the leading order form of $V_1'\left(s\right)$.

7.4 Solution to $V_1'\left(s\right)$ including the z-boundary layer correction terms

As discussed above, we need to reconsider the equation for $H\left(x,z\right)$ inside the boundary layer by the inclusion of z-boundary correction terms. This is done by expressing $H\left(x,z\right)$ as

$$H\left(x,z\right) = H^a\left(x,z\right) + H^g\left(x,z\right) + \varepsilon^2 h\left(s,z\right) + \varepsilon^2 \check{h}(s,\check{\zeta}) + \varepsilon^2 \hat{h}(s,\hat{\zeta}), \tag{7.53}$$

where we have introduced the z-boundary layer stretched coordinates $\hat{\zeta} = \left(1-z\right)/\varepsilon$ and $\check{\zeta} = z/\varepsilon$, and where $\hat{h}$ and $\check{h}$ are the new terms that accommodate the upper and lower z-boundary layers respectively. In figure 7.5 we sketch the x-z-boundary layers and we note the structure of $H\left(x,z\right)$ in the following regions:

$$H\left(x,z\right) = H^a\left(x,z\right) + H^g\left(x,z\right) \text{ in region 1,}$$

$$H\left(x,z\right) = H^a\left(x,z\right) + H^g\left(x,z\right) + \varepsilon^2 h\left(s,z\right) \text{ in region 2,}$$

$$H\left(x,z\right) = H^a\left(x,z\right) + H^g\left(x,z\right) + \varepsilon^2\left(h(s,\hat{\zeta}) + \hat{h}(s,\hat{\zeta})\right) \text{ in region 3,}$$

$$H\left(x,z\right) = H^a\left(x,z\right) + H^g\left(x,z\right) + \varepsilon^2\left(h(s,\hat{\zeta}) + \check{h}(s,\check{\zeta})\right) \text{ in region 4.}$$

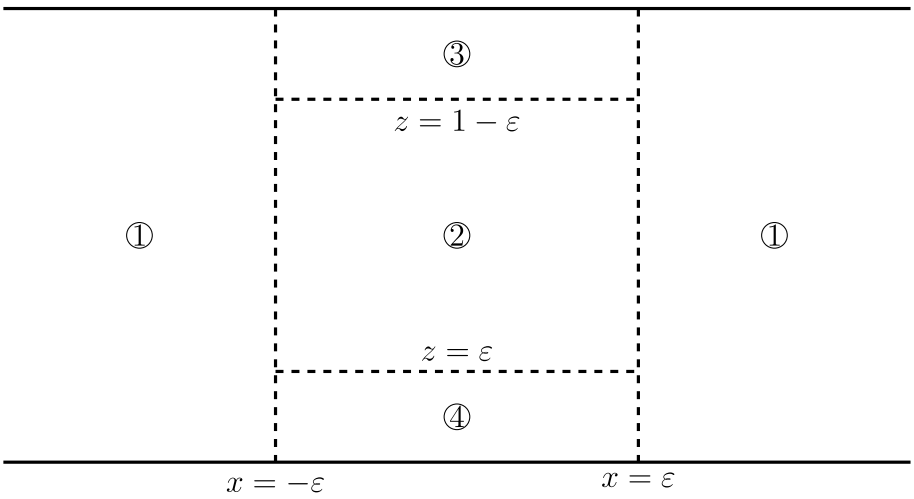

Figure 7.5: Sketch of the x- and z-boundary layers.

We note that $\check{h}$ and $\hat{h}$ tend to zero as $s \to \pm\infty$, i.e. this z-boundary layer is contained only within the x-boundary layer. The z-boundary correction terms are substituted into (7.44), leading to Laplace's equation,

$$\left(\frac{\partial^2}{\partial s^2} + \frac{\partial^2}{\partial \check{\zeta}^2}\right) \check{h}\left(s, \check{\zeta}\right) = 0, \tag{7.54}$$

$$\left(\frac{\partial^2}{\partial s^2} + \frac{\partial^2}{\partial \hat{\zeta}^2}\right) \hat{h}\left(s, \hat{\zeta}\right) = 0, \tag{7.55}$$

together with the boundary conditions,

$$\check{h}\left(s, 0\right) + h_1\left(s\right) k = 0, \text{ on } z = \check{\zeta} = 0, \tag{7.56}$$

$$\hat{h}\left(s, 0\right) + h_1\left(s\right) k e^{-k} = 0, \text{ on } z = 1, \hat{\zeta} = 0. \tag{7.57}$$

Equations (7.54) and (7.55), with the boundary conditions (7.56) and (7.57), constitute a Dirichlet problem for both $\check{h}$ and $\hat{h}$. Fortunately, we do not need to solve these boundary value problems in order to obtain the solution for $V_1'\left(s\right)$.

Substitution of (7.53) into (7.10) gives

$$\begin{aligned}\frac{\partial \psi}{\partial z} =& \frac{\partial\left(H^a, A\right)}{\partial\left(x, z\right)} + \frac{\partial\left(H^g, A\right)}{\partial\left(x, z\right)} + \frac{\partial}{\partial x}\left(\varepsilon^2 k e^{-kz} h_1\left(s\right)\right)\frac{\partial A}{\partial z} - \frac{\partial}{\partial z}\left(\varepsilon^2 k e^{-kz} h_1\left(s\right)\right)\frac{\partial A}{\partial x} \\ &+ \frac{\partial}{\partial x}\left(\varepsilon^2 \check{h}(s, \check{\zeta})\right)\frac{\partial A}{\partial z} - \frac{\partial}{\partial z}\left(\varepsilon^2 \check{h}(s, \check{\zeta})\right)\frac{\partial A}{\partial x} + \frac{\partial}{\partial x}\left(\varepsilon^2 \hat{h}(s, \hat{\zeta})\right)\frac{\partial A}{\partial z} \\ &- \frac{\partial}{\partial z}\left(\varepsilon^2 \hat{h}(s, \hat{\zeta})\right)\frac{\partial A}{\partial x} - \frac{1}{\varepsilon^2 \mathrm{Ha}^2}\frac{\mathrm{d}^2 V_1}{\mathrm{d}s^2}.\end{aligned} \tag{7.58}$$

By construction, the leading order solution at $\mathcal{O}(1)$ satisfies Taylor's constraint,

$$\int_0^1 \frac{\partial(H^a, A)}{\partial(x,z)} + \frac{\partial(H^g, A)}{\partial(x,z)} \mathrm{d}z = \text{const.} \tag{7.59}$$

We therefore now need to consider the $\mathcal{O}(\varepsilon^2)$ terms inside the boundary layer. In order for the $\varepsilon^{-2}\mathrm{Ha}^{-2}$ term to be $\mathcal{O}(\varepsilon^2)$, equation (7.58) would suggest an ordering for ε in terms of Ha as

$$\varepsilon \sim \mathcal{O}\left(\mathrm{Ha}^{-\frac{1}{2}}\right). \tag{7.60}$$

Inside the boundary layer we consider expansions about $x = 0$ (or $s = 0$) for the trigonometric functions. Evaluating the x and z boundary layer terms gives

$$\int_0^1 \frac{\partial}{\partial x}\left(\varepsilon^2 k e^{-kz} h_1(s)\right)\frac{\partial A}{\partial z}\mathrm{d}z = -\int_0^1 \varepsilon^2 k^2 e^{-2kz} s \frac{\mathrm{d}h_1}{\mathrm{d}s}\mathrm{d}z, \tag{7.61}$$

$$\int_0^1 \frac{\partial}{\partial z}\left(\varepsilon^2 k e^{-kz} h_1(s)\right)\frac{\partial A}{\partial x}\mathrm{d}z = \int_0^1 \varepsilon^2 k^2 e^{-2kz} h_1(s)\,\mathrm{d}z, \tag{7.62}$$

$$\int_0^1 \frac{\partial}{\partial x}\left(\varepsilon^2 \check{h}(s,\check{\zeta})\right)\frac{\partial A}{\partial z}\mathrm{d}z = -\int_0^1 \varepsilon^2 \frac{\partial \check{h}}{\partial s} k e^{-kz} s\mathrm{d}z. \tag{7.63}$$

To leading order, near $z = 0$, $e^{-kz} \approx 1$; hence (7.63), which is in the bottom z-boundary layer, is

$$-\varepsilon^2 k \int_0^1 \frac{\partial \check{h}}{\partial s} e^{-kz} s\mathrm{d}z = -\varepsilon^3 k s \int_0^\infty \frac{\partial \check{h}}{\partial s}\mathrm{d}\check{\zeta}. \tag{7.64}$$

Since this integral is $\mathcal{O}(\varepsilon^3)$, and hence smaller than all other terms, it is ignored. The next correction term is

$$\begin{aligned} -\int_0^1 \frac{\partial}{\partial z}\left(\varepsilon^2 \check{h}(s,\check{\zeta})\right)\frac{\partial A}{\partial x}\mathrm{d}z &= -\varepsilon^2 \int_0^\infty \frac{\partial}{\partial \check{\zeta}}\left(\check{h}(s,\check{\zeta})\right) e^{-kz}\mathrm{d}\check{\zeta} \\ &= -\varepsilon^2 \int_0^\infty \frac{\partial}{\partial \check{\zeta}}\check{h}(s,\check{\zeta})\mathrm{d}\check{\zeta} \\ &= \varepsilon^2 \check{h}(s,0), \end{aligned} \tag{7.65}$$

since $\check{h}(s,\check{\zeta}) = 0$ as $\check{\zeta} \to \infty$. As $\check{h}(s,\check{\zeta})$ is the correction term for the bottom boundary condition, it must satisfy (7.56). Therefore

$$\check{h}(s,0) = -k h_1(s), \tag{7.66}$$

allowing us to express (7.65) in terms of the function $h_1(s)$,

$$-\int_0^1 \frac{\partial}{\partial z}\left(\varepsilon^2 \check{h}(s,\check{\zeta})\right)\frac{\partial A}{\partial x}\mathrm{d}z = -\varepsilon^2 k h_1(s). \tag{7.67}$$

There is also another $\mathcal{O}\left(\varepsilon^3\right)$ term in (7.58); near $z=1$, $e^{-kz} \approx e^{-k}$ and expanding $\sin\left(kx\right)$ near $x=0$ gives

$$\int_0^1 \frac{\partial}{\partial x}\left(\varepsilon^2 \hat{h}(s,\hat{\zeta})\right)\frac{\partial A}{\partial z}\mathrm{d}z = -ke^{-k}\varepsilon^3 s\int_0^\infty \frac{\partial \hat{h}}{\partial s}\mathrm{d}\hat{\zeta}, \tag{7.68}$$

which is smaller in comparison to the $\mathcal{O}\left(\varepsilon^2\right)$ terms. Finally,

$$-\int_0^1 \frac{\partial}{\partial z}\left(\varepsilon^2 \hat{h}(s,\hat{\zeta})\right)\frac{\partial A}{\partial x}\mathrm{d}z = \int_0^\infty \frac{\partial}{\partial \hat{\zeta}}\left(\varepsilon^2 \hat{h}\right)e^{-kz}\mathrm{d}\hat{\zeta}. \tag{7.69}$$

Near $z=1$, $e^{-kz}\approx e^{-k}$ and therefore this upper z-boundary correction term becomes

$$\varepsilon^2\int_0^\infty \frac{\partial \hat{h}}{\partial \hat{\zeta}}ke^{-k}\mathrm{d}\hat{\zeta} = -\varepsilon^2\hat{h}\left(s,1\right)e^{-k}. \tag{7.70}$$

We take advantage of the boundary condition (7.57), which allows us to express the upper correction term $\hat{h}(s,\hat{\zeta})$ in terms of $h_1\left(s\right)$. From (7.57) we write

$$\hat{h}\left(s,0\right) = -h\left(s,1\right) = -ke^{-k}h_1\left(s\right). \tag{7.71}$$

Expression (7.70) becomes,

$$-\int_0^1 \frac{\partial}{\partial z}\left(\varepsilon^2 \hat{h}(s,\hat{\zeta})\right)\frac{\partial A}{\partial x}\mathrm{d}z = \varepsilon^2 ke^{-2k}h_1\left(s\right). \tag{7.72}$$

The diffusion term, $\mathrm{Ha}^{-2}\nabla^2 v$, inside the boundary layer is simply

$$-\frac{1}{\varepsilon^2}\frac{1}{\mathrm{Ha}^2}\frac{\mathrm{d}^2V_1}{\mathrm{d}s^2}\int_0^1 \mathrm{d}z = -\frac{1}{\varepsilon^2}\frac{1}{\mathrm{Ha}^2}\frac{\mathrm{d}^2V_1}{\mathrm{d}s^2}. \tag{7.73}$$

Combining (7.61), (7.62), (7.67), (7.72) and (7.73), the z-boundary layer terms in equation (7.58) are

$$\begin{aligned} -\int_0^1 k^2e^{-2kz}s\frac{\mathrm{d}h_1}{\mathrm{d}s}\mathrm{d}z + &\int_0^1 k^2e^{-2kz}h_1\mathrm{d}z - kh_1\left(s\right) \\ &+ ke^{-2k}h_1\left(s\right) - \frac{1}{\varepsilon^4}\frac{1}{\mathrm{Ha}^2}\frac{\mathrm{d}^2V_1}{\mathrm{d}s^2} = 0. \end{aligned} \tag{7.74}$$

We choose ε to scale as

$$\varepsilon = \mathrm{Ha}^{-\frac{1}{2}}k^{-\frac{1}{2}}\left(\int_0^1 e^{-2kz}\mathrm{d}z\right)^{-\frac{1}{4}} \tag{7.75}$$

where the choice of multiplicative constant is simply for algebraic convenience. All terms in (7.74) are now $\mathcal{O}\left(\varepsilon^2\right)$, and with (7.75), we have

$$\frac{\mathrm{d}^2V_1}{\mathrm{d}s^2} = -s\frac{\mathrm{d}h_1}{\mathrm{d}s} - h_1. \tag{7.76}$$

Equation (7.76) can be expressed as

$$\frac{\mathrm{d}^2 V_1}{\mathrm{d}s^2} = -\frac{\mathrm{d}}{\mathrm{d}s}\left(sh_1\right), \tag{7.77}$$

which, on integration, gives

$$h_1\left(s\right) = -\frac{V_1'\left(s\right)}{s}. \tag{7.78}$$

The constant of integration in (7.78) must be zero since $V_1'\left(s\right) \to 0$ and $h_1\left(s\right) \to 0$ as $s \to 0$. Given equation (7.78), we can rewrite (7.52) as

$$\frac{\mathrm{d}^2}{\mathrm{d}s^2}\left(\frac{V_1'}{s}\right) - sV_1' + \tilde{V}_0 = 0. \tag{7.79}$$

Using the substitution $\frac{1}{2}s^2 = t$, and $V_1' = t^{\alpha} y\left(t\right)$, where α is to be determined, gives

$$\begin{aligned} t^{\alpha+\frac{1}{2}}\frac{\mathrm{d}^2 y}{\mathrm{d}t^2} + \alpha t^{\alpha-\frac{1}{2}}\frac{\mathrm{d}y}{\mathrm{d}t} + \left(\alpha - \frac{1}{2}\right)t^{\alpha-\frac{1}{2}}\frac{\mathrm{d}y}{\mathrm{d}t}& \\ + \left(\alpha - \frac{1}{2}\right)\left(\alpha - 1\right)t^{\alpha-\frac{3}{2}}y + \frac{\tilde{V}_0}{\sqrt{2}} - t^{\alpha+\frac{1}{2}}y = 0.& \end{aligned} \tag{7.80}$$

We now choose $\alpha = \frac{3}{4}$ in order to simplify (7.80), which becomes

$$t^2\frac{\mathrm{d}^2 y}{\mathrm{d}t^2} + t\frac{\mathrm{d}y}{\mathrm{d}t} - \left(\frac{1}{16} + t^2\right)y = -\frac{\tilde{V}_0}{\sqrt{2}}t^{\frac{3}{4}}. \tag{7.81}$$

We now let $w = Ay$, where A is a constant to be determined, and substitute into (7.81) to obtain

$$t^2\frac{\mathrm{d}^2 y}{\mathrm{d}t^2} + t\frac{\mathrm{d}y}{\mathrm{d}t} - \left(\frac{1}{16} + t^2\right)y = -\frac{\tilde{V}_0}{A\sqrt{2}}t^{\frac{3}{4}}. \tag{7.82}$$

Choosing A as

$$A = -\frac{\tilde{V}_0}{2^{\frac{7}{4}}}\sqrt{\pi}\Gamma\left(\frac{1}{4}\right), \tag{7.83}$$

results in equation (7.82) becoming the modified Struve equation of order $-1/4$. The modified Struve equation takes the form,

$$t^2\frac{\mathrm{d}^2 w}{\mathrm{d}t^2} + t\frac{\mathrm{d}w}{\mathrm{d}t} - \left(\nu^2 + t^2\right)w = \frac{4\left(\frac{t}{2}\right)^{1+\nu}}{\sqrt{\pi}\Gamma\left(\nu\right)} \tag{7.84}$$

with solution,

$$w\left(t\right) = c_1 I_{\nu}\left(t\right) + c_2 K_{\nu}\left(t\right) + \mathbf{L}_{\nu}\left(t\right), \tag{7.85}$$

where $I_{\nu}\left(t\right)$ and $K_{\nu}\left(t\right)$ are the modified Bessel functions of the first and second kind respectively, and $\mathbf{L}_{\nu}\left(t\right)$ is the modified Struve function (see Abramowitz & Stegun

(1964)). Hence, given $\alpha = -1/4$ and $V_1'(s) = t^{\alpha} y(t)$, the general solution to $V_1'(s)$ is

$$V_1'(s) = -\frac{\tilde{V}_0}{4}\sqrt{\frac{\pi}{2}}\Gamma\left(\frac{1}{4}\right)s^{\frac{3}{2}}\left[c_1 I_{-\frac{1}{4}}\left(\frac{1}{2}s^2\right) + c_2 K_{-\frac{1}{4}}\left(\frac{1}{2}s^2\right) + \mathbf{L}_{-\frac{1}{4}}\left(\frac{1}{2}s^2\right)\right]. \tag{7.86}$$

To determine the exact form of $V_1'(s)$, we must ensure that the solution inside the boundary layer matches onto the exterior solution, as derived in the matching principle (7.39). The second boundary condition we apply is that the function $V_1'(s)$ is an odd function, which ensures that the boundary layer solution has the same property of the exterior solution, which is also an odd function. Applying both these conditions will fully determine (7.86). We first note that

$$K_{-\frac{1}{4}}\left(\frac{1}{2}s^2\right) = K_{\frac{1}{4}}\left(\frac{1}{2}s^2\right) \sim s^{\frac{1}{2}} \tag{7.87}$$

is an even function of s, which means that we must have $c_2 = 0$ in order for (7.86) to be an odd function of s. As $s \to \infty$, we note, from (12.2.6) in Abramowitz & Stegun (1964),

$$s^{\frac{3}{2}}\mathbf{L}_{-\frac{1}{4}}\left(\frac{1}{2}s^2\right) - s^{\frac{3}{2}} I_{\frac{1}{4}}\left(\frac{1}{2}s^2\right) \sim \frac{-2^{\frac{10}{4}}}{\sqrt{\pi}\Gamma\left(\frac{1}{4}\right)}\frac{1}{s} + \mathcal{O}\left(\frac{1}{s^5}\right). \tag{7.88}$$

Since

$$K_{\frac{1}{4}}\left(\frac{1}{2}s^2\right) = \frac{\pi}{\sqrt{2}}\left(I_{-\frac{1}{4}}\left(\frac{1}{2}s^2\right) - I_{\frac{1}{4}}\left(\frac{1}{2}s^2\right)\right) \to 0 \tag{7.89}$$

as $s \to \infty$, then

$$I_{\frac{1}{4}}\left(\frac{1}{2}s^2\right) = I_{-\frac{1}{4}}\left(\frac{1}{2}s^2\right) \tag{7.90}$$

as $s \to \infty$. Hence (7.86) will have the correct behaviour at $s \to \infty$ on setting $c_1 = -1$, such that (7.88) holds, giving

$$V_1'(s) = -\frac{\tilde{V}_0}{4}\sqrt{\frac{\pi}{2}}\Gamma\left(\frac{1}{4}\right)s^{\frac{3}{2}}\left[\mathbf{L}_{-\frac{1}{4}}\left(\frac{1}{2}s^2\right) - I_{-\frac{1}{4}}\left(\frac{1}{2}s^2\right)\right]. \tag{7.91}$$

This is the solution in terms of the inner stretched coordinate s. The solution $V_1'(x)$ is then recovered from (7.36) and (7.75), namely

$$V_1'(x) = -\frac{\tilde{V}_0}{4}\sqrt{\frac{\pi}{2}}\Gamma\left(\frac{1}{4}\right)\mathrm{Ha}^{\frac{5}{2}}c^{\frac{5}{2}}x^{\frac{3}{2}}\left[\mathbf{L}_{-\frac{1}{4}}\left(\frac{1}{2}\mathrm{Ha}c^2x^2\right) - I_{-\frac{1}{4}}\left(\frac{1}{2}\mathrm{Ha}c^2x^2\right)\right], \tag{7.92}$$

where

$$c = k^{\frac{1}{2}}\left(\int_0^1 e^{-2kz}\mathrm{d}z\right)^{\frac{1}{4}}. \tag{7.93}$$

The solution (7.92) can then be used to find the composite solution, which gives us the solution throughout the whole domain in x; this is found by adding the inner and outer solutions and subtracting the overlapping solution. Adding (7.92) and (4.38) and removing the overlap yields the following composite solution,

$$\begin{aligned} V_1'(x) = &-\frac{\tilde{V}_0}{4}\sqrt{\frac{\pi}{2}}\Gamma\left(\frac{1}{4}\right)\mathrm{Ha}^{\frac{5}{2}}c^{\frac{5}{2}}x^{\frac{3}{2}}\left[\mathbf{L}_{-\frac{1}{4}}\left(\frac{1}{2}\mathrm{Ha}c^2x^2\right) - I_{-\frac{1}{4}}\left(\frac{1}{2}\mathrm{Ha}c^2x^2\right)\right] \\ &+ \tilde{V}_0 k\cot\left(kx\right) - \frac{\tilde{V}_0}{x}. \end{aligned} \tag{7.94}$$

7.5 The $\mathcal{O}\left(\varepsilon^3\right)$ z-boundary correction terms

Equation (7.94) is the solution to $V_1'(s)$ when considering the $\mathcal{O}\left(\varepsilon^2\right)$ terms in the boundary layer; it does not include the $\mathcal{O}\left(\varepsilon^3\right)$ terms that are attributed to the z-boundary layer. It would therefore be of interest to see whether an analytical solution to the $\mathcal{O}\left(\varepsilon^3\right)$ terms, (7.64) and (7.68), can be found and hence subsequently the next order contribution for $V_1'(s)$. On both boundaries we have to solve Laplace's equation with Dirichlet boundary conditions. From (7.54) and (7.56) the solution to $\check{h}\left(s,\check{\zeta}\right)$ becomes a half-space Dirichlet problem (Ockendon, 2003). The solution to $\check{h}\left(s,\check{\zeta}\right)$ is then defined as

$$\check{h}\left(s,\check{\zeta}\right) = -\frac{\check{\zeta}}{\pi}\int_{-\infty}^{\infty}\frac{kh_1\left(s'\right)}{\left(s-s'\right)^2+\check{\zeta}^2}\mathrm{d}s'. \tag{7.95}$$

Taking the partial derivative with respect to s gives

$$\frac{\partial\check{h}}{\partial s} = -\frac{\check{\zeta}}{\pi}\int_{-\infty}^{\infty}\frac{2kh_1\left(s'\right)\left(s'-s\right)}{\left(\left(s-s'\right)^2+\check{\zeta}^2\right)^2}\mathrm{d}s'. \tag{7.96}$$

Expression (7.96) is integrated with respect to the stretched coordinate $\check{\zeta}$ over the domain $0 \leq \check{\zeta} < \infty$, giving

$$\int_0^{\infty}\frac{\partial\check{h}}{\partial s}\mathrm{d}\check{\zeta} = -\frac{2}{\pi}\int_{s=-\infty}^{\infty}kh_1\left(s'\right)\left(s'-s\right)\int_{\check{\zeta}=0}^{\infty}\frac{\check{\zeta}}{\left(\left(s-s'\right)^2+\check{\zeta}^2\right)^2}\mathrm{d}\check{\zeta}\mathrm{d}s'. \tag{7.97}$$

Let $\check{\zeta} = (s - s')\tan\theta$; if $s > s'$ then

$$\int_{\check{\zeta}=0}^{\infty} \frac{\check{\zeta}}{\left((s-s')^2 + \check{\zeta}^2\right)^2}\mathrm{d}\check{\zeta} = \int_0^{\frac{\pi}{2}} \frac{\sin(2\theta)}{2(s-s')^2}\mathrm{d}\theta$$

$$= \frac{1}{2(s-s')^2} \tag{7.98}$$

whilst if we let $\check{\zeta} = (s' - s)\tan\theta$ with $s < s'$, we again recover the result (7.98). Hence substitution of (7.98) into (7.97) leads to a simplified expression in terms of s and s', namely

$$\int_0^{\infty} \frac{\partial \check{h}}{\partial s}\mathrm{d}\check{\zeta} = \frac{k}{\pi}\int_{s'=-\infty}^{\infty} \frac{h_1(s')}{(s-s')}\mathrm{d}s'. \tag{7.99}$$

As a consequence of (7.99), equation (7.64) can be expressed as

$$-\varepsilon^3 ks\int_0^{\infty} \frac{\partial \check{h}}{\partial s}\mathrm{d}\check{\zeta} = -\frac{\varepsilon^3 k^3 s}{\pi}\int_{s'=-\infty}^{\infty} \frac{h_1(s')}{(s-s')}\mathrm{d}s'. \tag{7.100}$$

Equation (7.100) is the lower $\mathcal{O}(\varepsilon^3)$ term i.e. it is the contribution from the z-boundary layer at $z = 0$ at $\mathcal{O}(\varepsilon^3)$. Likewise, from (7.55) and (7.57) the solution to $\hat{h}(s, \hat{\zeta})$ is also a half-space Dirichlet problem. The solution to $\hat{h}(s, \hat{\zeta})$ is defined as

$$\hat{h}(s, \hat{\zeta}) = -\frac{\hat{\zeta}}{\pi}\int_{-\infty}^{\infty} \frac{ke^{-k}h_1(s')}{(s-s')^2 + \hat{\zeta}^2}\mathrm{d}s'. \tag{7.101}$$

Taking the partial derivative with respect to s gives

$$\frac{\partial \hat{h}}{\partial s} = -\frac{\hat{\zeta}}{\pi}\int_{-\infty}^{\infty} \frac{2ke^{-k}h_1(s')(s'-s)}{((s-s')^2 + \hat{\zeta}^2)^2}\mathrm{d}s'. \tag{7.102}$$

Expression (7.102) is integrated with respect to the stretched coordinate $\hat{\zeta}$ over the domain $0 \leq \hat{\zeta} < \infty$, giving

$$\int_0^{\infty} \frac{\partial \hat{h}}{\partial s}\mathrm{d}\hat{\zeta} = -\frac{2}{\pi}e^{-k}\int_{s=-\infty}^{\infty} kh_1(s')(s'-s)\int_{\hat{\zeta}=0}^{\infty} \frac{\hat{\zeta}}{((s-s')^2 + \hat{\zeta}^2)^2}\mathrm{d}\hat{\zeta}\mathrm{d}s'. \tag{7.103}$$

Let $\hat{\zeta} = (s - s')\tan\theta$; if $s > s'$ then

$$\int_{\hat{\zeta}=0}^{\infty} \frac{\hat{\zeta}}{\left((s-s')^2 + \hat{\zeta}^2\right)^2}\mathrm{d}\hat{\zeta} = \int_0^{\frac{\pi}{2}} \frac{\sin(2\theta)}{2(s-s')^2}\mathrm{d}\theta$$

$$= \frac{1}{2(s-s')^2} \tag{7.104}$$

whilst if we let $\hat{\zeta} = (s' - s)\tan\theta$ with $s < s'$, the same result applies. Substitution of (7.104) into equation (7.103) gives

$$\int_0^\infty \frac{\partial \hat{h}}{\partial s}\mathrm{d}\hat{\zeta} = \frac{ke^{-k}}{\pi}\int_{s'=-\infty}^{\infty} \frac{h_1(s')}{(s-s')}\mathrm{d}s'. \tag{7.105}$$

The upper $\mathcal{O}(\varepsilon^3)$ term, given by (7.68), which represents the contribution from the z-boundary layer near $z = 1$ at $\mathcal{O}(\varepsilon^3)$, can be expressed as

$$-k\varepsilon^3\int_0^1 \frac{\partial}{\partial x}\left(\hat{h}(s,\hat{\zeta})\right)e^{-kz}s\mathrm{d}z = -\frac{\varepsilon^3k^2e^{-2k}s}{\pi}\int_{s'=-\infty}^{\infty}\frac{h_1(s')}{s-s'}\mathrm{d}s'. \tag{7.106}$$

Substituting (7.100) and (7.106) into equation (7.58) gives, at $\mathcal{O}(\varepsilon^2)$,

$$\begin{aligned}&-\int_0^1 k^2e^{-2kz}s\frac{\mathrm{d}h_1}{\mathrm{d}s}\mathrm{d}z + \int_0^1 k^2e^{-2kz}h_1\mathrm{d}z - kh_1(s) + ke^{-2k}h_1(s)\\ &-\frac{\varepsilon k^2 s}{\pi}\int_{-\infty}^{\infty}\frac{h_1(s')}{(s-s')}\mathrm{d}s' - \frac{\varepsilon k^2e^{-2k}s}{\pi}\int_{-\infty}^{\infty}\frac{h_1(s')}{s-s'}\mathrm{d}s' - \frac{1}{\varepsilon^4}\frac{1}{\mathrm{Ha}^2}\frac{\mathrm{d}^2V_1}{\mathrm{d}s^2} = 0.\end{aligned} \tag{7.107}$$

Using the scaling (7.75), equation (7.107) becomes

$$\frac{\mathrm{d}^2V_1}{\mathrm{d}s^2} = -s\frac{\mathrm{d}h_1}{\mathrm{d}s} - h_1 - \frac{2\varepsilon k}{\pi}\left(\frac{1+e^{-2k}}{1-e^{-2k}}\right)s\int_{-\infty}^{\infty}\frac{h_1(s')}{s-s'}\mathrm{d}s'. \tag{7.108}$$

Equation (7.108), along with (7.52), determines the solution to $V_1'(s)$ up to $\mathcal{O}(\varepsilon^3)$ and the solution to $h_1(s,z)$ up to $\mathcal{O}(\varepsilon^2)$ in the boundary layer.

7.6 Comparisons with the numerical results

The numerical simulations are used for comparison between the analytical solution (7.92) and the numerically evaluated $V_0'(x)$ found using the techniques described in §5. We have also performed numerical simulations to provide evidence of the z-boundary layers which would validate the analysis in §7.4 and §7.5.

In figure 7.6, the solution to $V_1'(s)$, given by (7.91), and the numerical solution to $V_0'(x)$ are plotted for increasing values of Ha. The domain of x in figure 7.6 is chosen such that the numerical solution is focused in the boundary layer and hence a comparison can be made with the boundary layer solution (7.91). As Ha is increased, the numerical solution tends slowly towards the asymptotic solution and the difference between the two solutions becomes smaller. The numerical maximum is smaller than the asymptotic maxima for all the values of Ha displayed; however this difference becomes smaller with Ha as the $\mathcal{O}(\varepsilon^3)$ terms become negligible. The numerical solution is well resolved with $M = 40$ modes in all solutions.

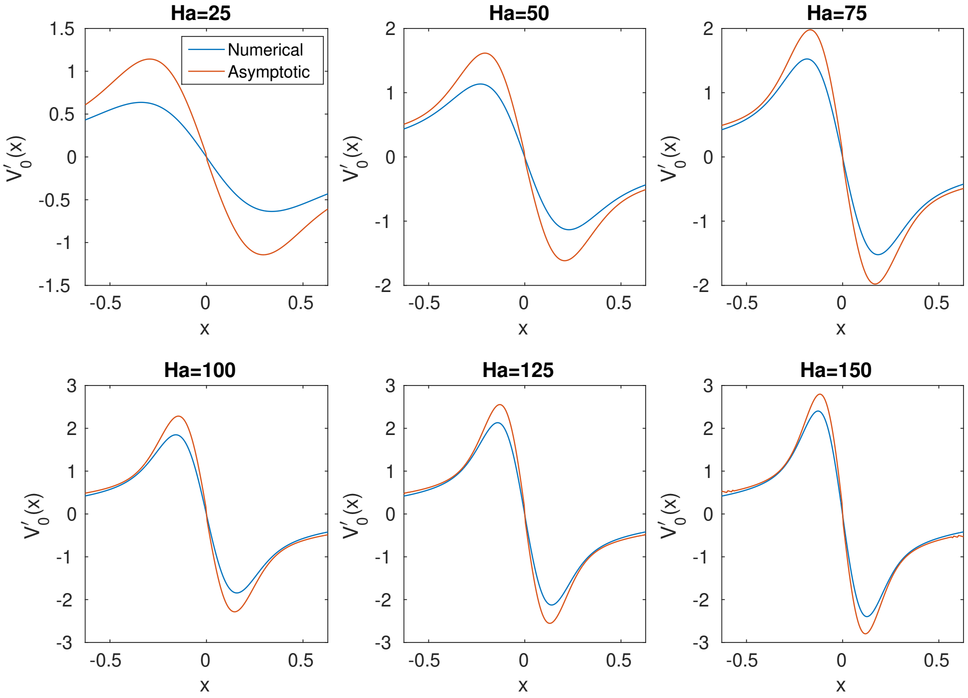

Figure 7.6: Comparisons of (7.91) and the numerical solution at varying Ha.

This difference in maxima can be improved if the expression (7.108) were evaluated. This would result in a significantly improved solution for smaller Ha, but figure 7.7 shows that the agreement of (7.91) is within 90% of the numerical maxima. We feel that the additional numerical treatment for (7.108) would result in only marginal gains at large Ha.

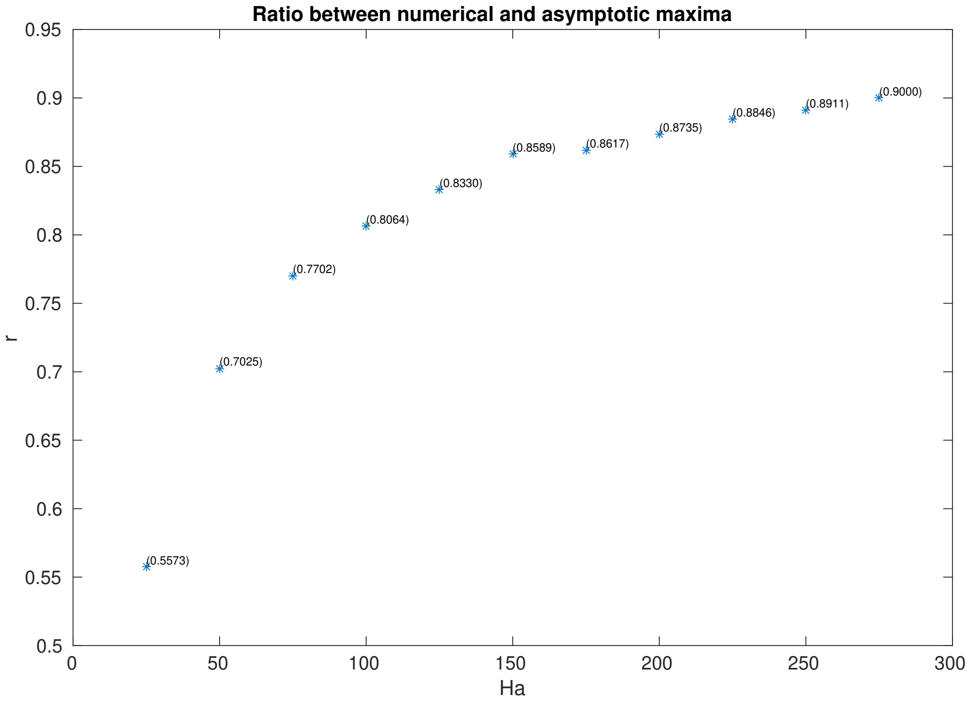

Figure 7.7: Ratio of the maxima of (7.91) and the numerical maxima.

The z-boundary layer structure can be revealed in the numerics by evaluating the following expression:

$$H_{num}\left(x,z\right)-H^{a}\left(x,z\right)-H^{g}\left(x,z\right)-\varepsilon^{2}h_{1}\left(s\right)e^{-kz}, \tag{7.109}$$

where $H_{num}\left(x,z\right)$ is the numerical solution to $H\left(x,z\right)$ at a given Ha. Expression (7.109) would also validate our assumption for the form of $H\left(x,z\right)$ given by (7.53). In figures 7.8 and 7.9 the contours of (7.109) are plotted for Ha $=100$ and Ha $=200$. We can see that there is z-structure at $z=0$ and $z=1$ that is confined near $x=\pi$. This confirms the theory that the z-boundary layer structure exists only within the x-boundary layer. The thickness of this boundary layer decreases with Ha in both the x and z direction. The thickness is expected to decrease in both directions as Ha increases since both boundary layers have a dependence on Ha.

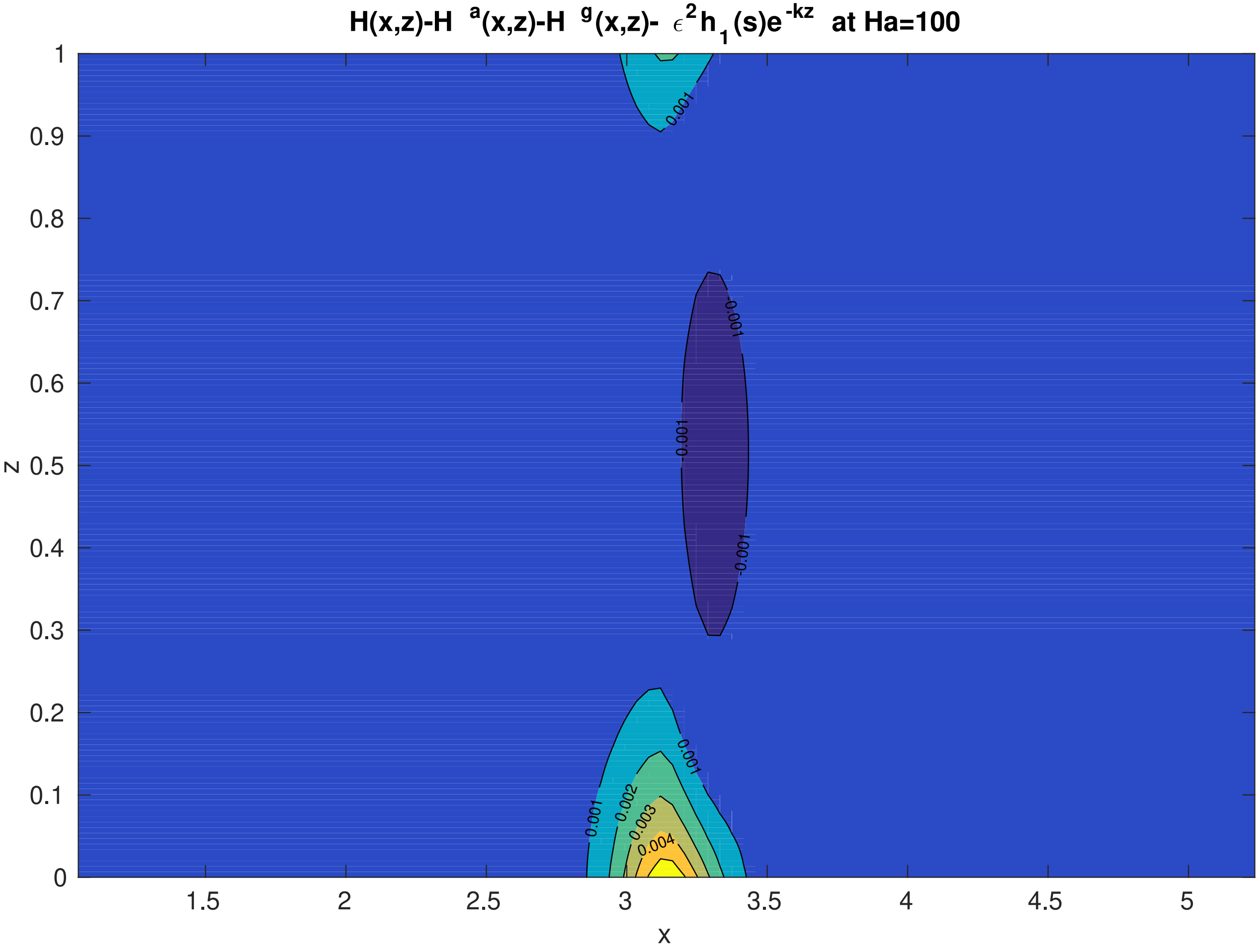

Figure 7.8: Contour plots of expression (7.109) at $\mathrm{Ha} = 100$ and $k = 1$.

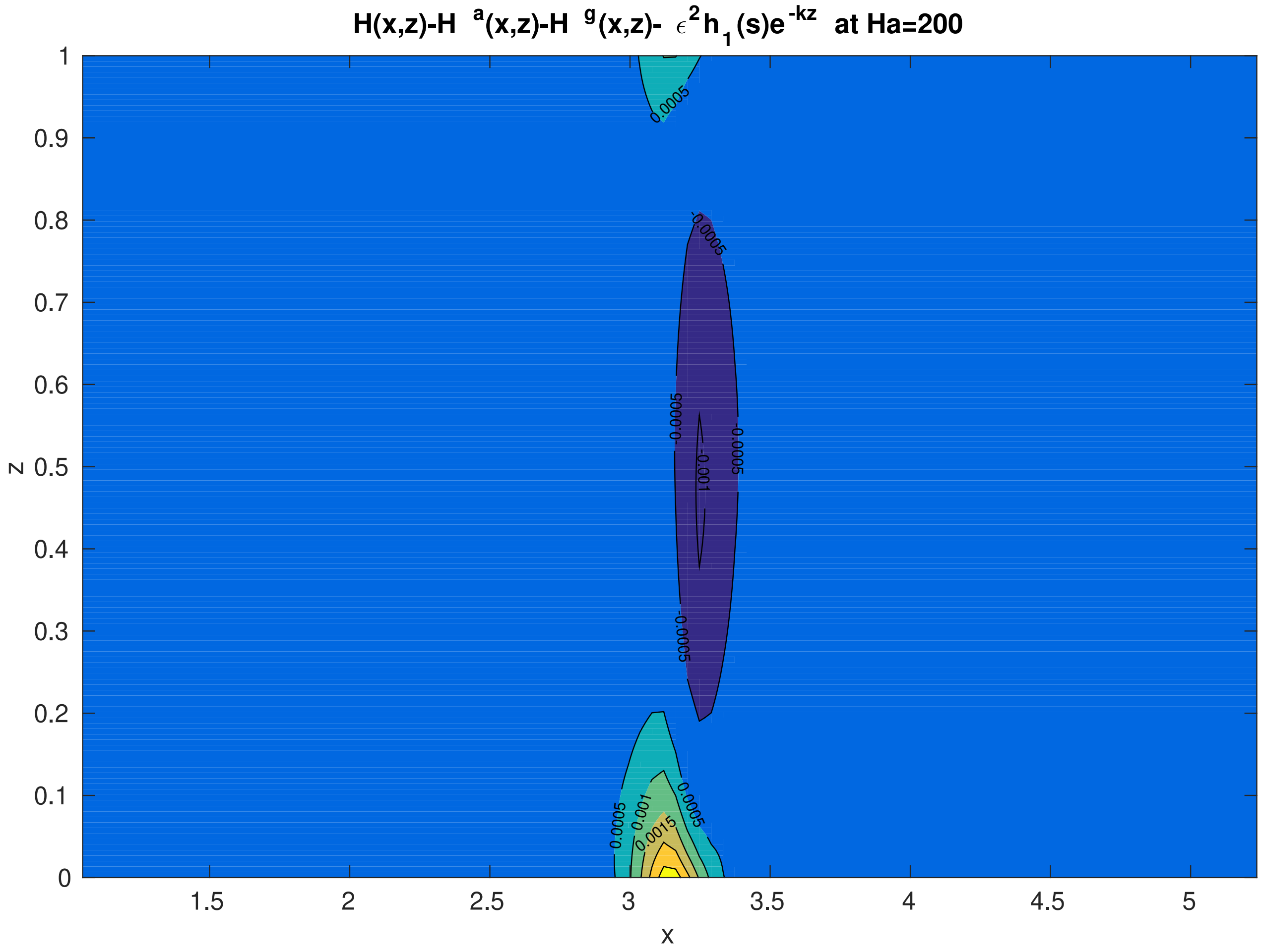

Figure 7.9: Contour plots of expression (7.109) at Ha = 200 and $k = 1$.

Chapter 8

The influence of a horizontal field

As shown in Chapter 4, $V_0'(x)$ has a singularity at $x = 0, \pi$ in the inviscid, small Rm limit. This can be attributed to the absence of magnetic field at $x = 0, \pi$, which, consequently, leads to infinite field line stretching at these points. In order to overcome this problem we have extended our model to include the effects of a background horizontal field that is confined within the stratified layer. A horizontal field in a Cartesian geometry represents an azimuthal magnetic field in a spherical geometry.

We now present numerical solutions for finite values of $\mathrm{B_s}$ by solving equations (5.1)-(5.5). Here we have compared a few cases owing to the time it would take to fully explore $(\mathrm{Rm}, \mathrm{Ha}, \mathrm{B_s})$ parameter space. This chapter extends the work presented in Chapter 6.

8.1 $\mathrm{B_s}$ in the extreme parameter value regime of Rm and Ha

We begin by looking at the effects of the horizontal field in various extreme parameter regimes, i.e. inviscid small Rm, inviscid large Rm and dominant viscosity at small Rm, in order to see how the structure of $V_0'(x)$ changes in these regimes. The choice of investigating these particular parameter regimes is because they are understood in the case of $\mathrm{B_s} = 0$, either by theoretical or numerical results, and so will help us understand how the inclusion of the horizontal field changes the model.

8.1.1 The inviscid, small Rm regime

The asymptotic theory of Chapter 4 predicts a singularity in the geostrophic flow for the inviscid small Rm regime due to the vanishing of the imposed magnetic field lines at $x = 0, \pi$. The inclusion of an azimuthal horizontal field in the layer should lead to the field being non-zero throughout, providing $\mathrm{B_s}$ is sufficiently large to overcome the singularity.

There are three regimes to consider at small Rm for an inviscid fluid with an imposed horizontal field. The boundary layer length scale found in the $\mathrm{B_s} = 0$ scenario scales approximately as $\varepsilon \sim \mathrm{Ha}^{-\frac{1}{2}}$ where ε is a small parameter; we therefore consider three cases, governed by the magnitude of $\mathrm{B_s}$: $0 < \mathrm{B_s} \leq \varepsilon$, $\varepsilon \leq \mathrm{B_s} < 1$ and $\mathrm{B_s} \geq 1$. The first case is of little interest as this is smaller than an $\mathcal{O}(\varepsilon)$ contribution to our solutions and so we expect to see the results shown in §7. The third case would be when the $\mathrm{Ha}^{-2}\nabla^2 v$ term is small and so any contributions from $\mathrm{B_s}$ are much more significant. The second case is the most interesting as this is the regime in which the singularity begins to disappear as $\mathrm{B_s}$ is increased; at the same time its contribution in the boundary layer is of the same order as all other terms.

For $\varepsilon \leq \mathrm{B_s} < 1$, the numerical solutions in figure 8.1 show that the singularity still exists in $V_0'(x)$ but its location is shifted in x. The singularity still occurs owing to the horizontal field not being large enough to eradicate the zero-field lines everywhere. In figure 8.1 and figure 8.2, the solutions for $\mathrm{B_s} = 0.1, 0.2, 0.5$ are calculated for $\mathrm{Ha} = 100$ and $\mathrm{Rm} \to 0$. This choice of Ha is in the correct regime as $\varepsilon \approx 0.1 < \mathrm{B_s}$. It is also numerically convenient to calculate solutions with weak viscosity at small Rm so that we are not susceptible to numerical viscosity in the inviscid small Rm regime.

In figure 8.1 the geostrophic flow and the contours of $v_x(x, z)$ are plotted. $V_0'(x)$ has an asymmetric structure, which is a feature of the horizontal field regime that can be explained by the coupling between all the harmonics when $\mathrm{B_s}$ is introduced, and can be seen in the energy spectra of $V_0'(x)$. We discuss this feature in §8.1.2. This asymmetry is also seen in the contours of $H(x, z)$ and the stream function shown in figure 8.2. The possibility of an analytical theory for the asymmetric solution to $V_0'(x)$ is considered in §8.3.1, where the boundary layer equations are reconsidered in the $\varepsilon \ll \mathrm{B_s} < 1$ regime.

Figure 8.3 shows that the singularity in $V_0'(x)$ has been removed at moderate values of $\mathrm{B_s}$. As the azimuthal field becomes the dominant contribution in the layer the meridional flow becomes purely geostrophic. This is due to the magnitude of $V_0'(x)$ increasing with $\mathrm{B_s}$ such that $V_0'(x)$ dominates the ageostrophic meridional flow $v^a(x, z)$. The asymmetry is no longer a feature of $V_0'(x)$ at larger values of $\mathrm{B_s}$ but asymmetry is still present in the system as can be seen in the contours of $H(x, z)$ plotted in figure 8.4. We note that in both figure 8.2 and figure 8.4 the stream function is asymmetric about $x = \pi$.

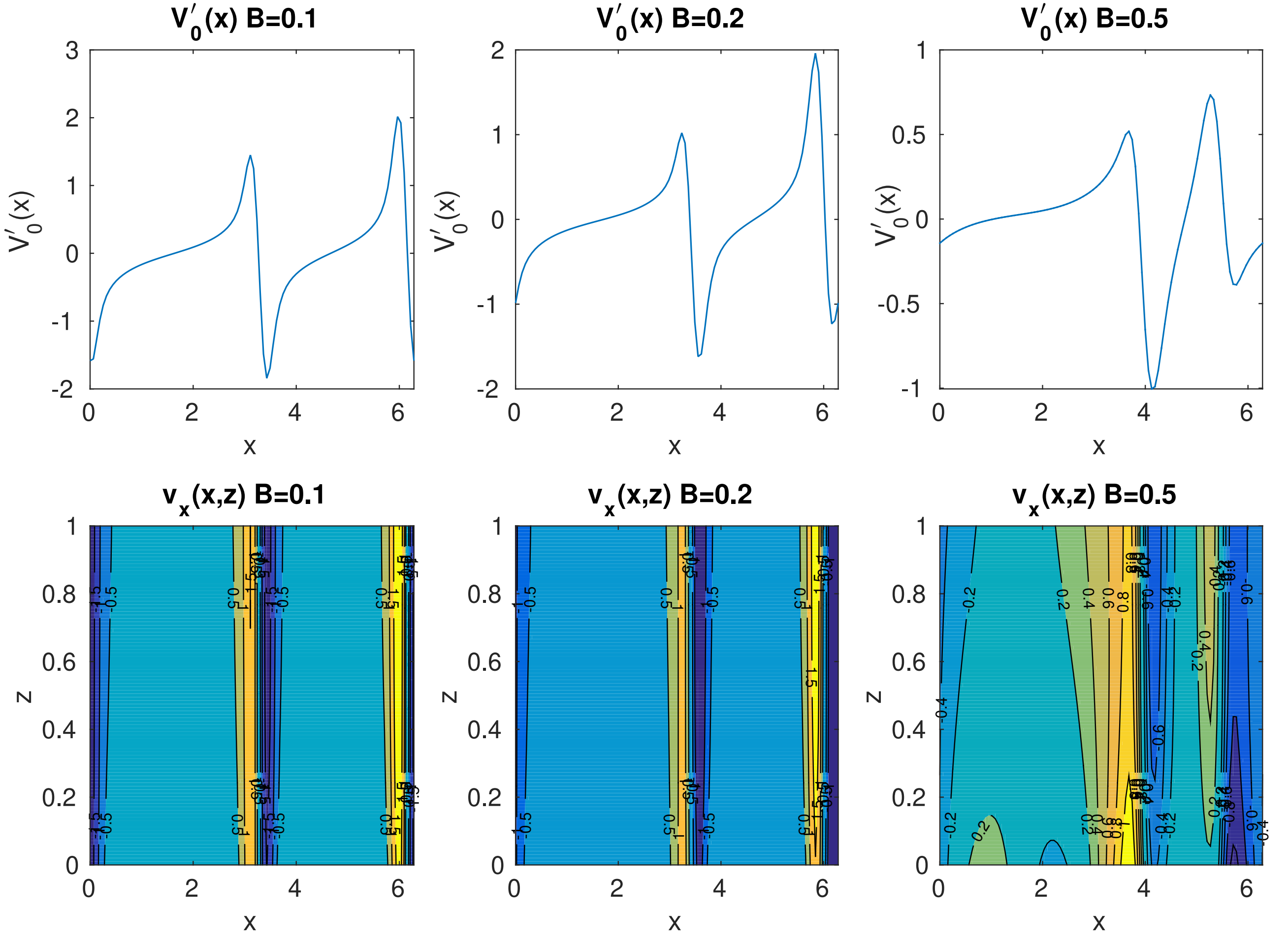

Figure 8.1: The geostrophic flow, $V_0'(x)$, and the contours of $v_x(x,z)$ for $\mathrm{Rm} \rightarrow 0$ and $\mathrm{Ha} = 100$. The horizontal field increases in strength from left to right: $\mathrm{B_s} = 0.1, 0.2, 0.5$.

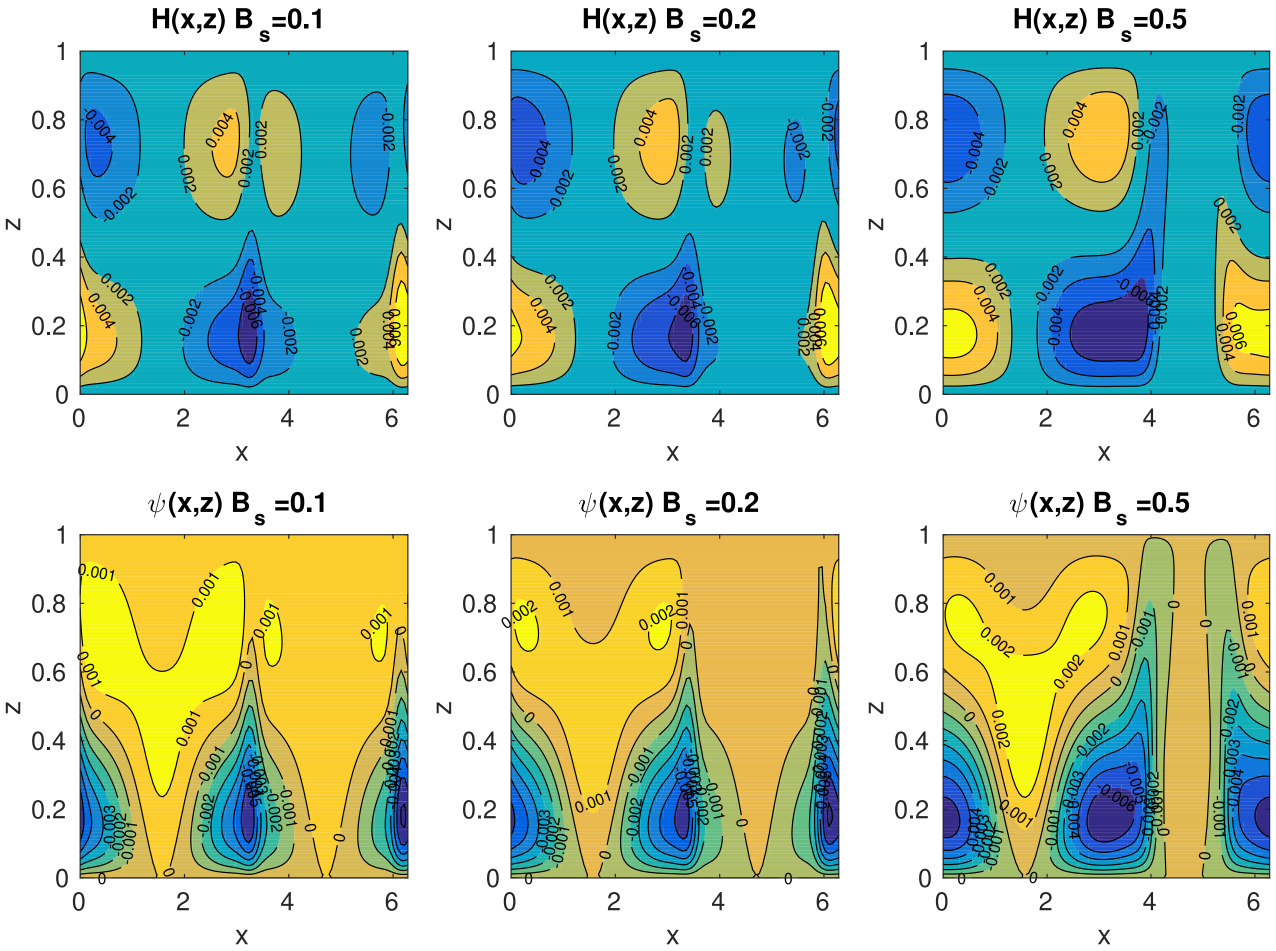

Figure 8.2: Contours of $H(x,z)$ and $\psi(x,z)$ for $\mathrm{Rm} \to 0$ and $\mathrm{Ha} = 100$. The horizontal field increases in strength from left to right: $\mathrm{B_s} = 0.1, 0.2, 0.5$.

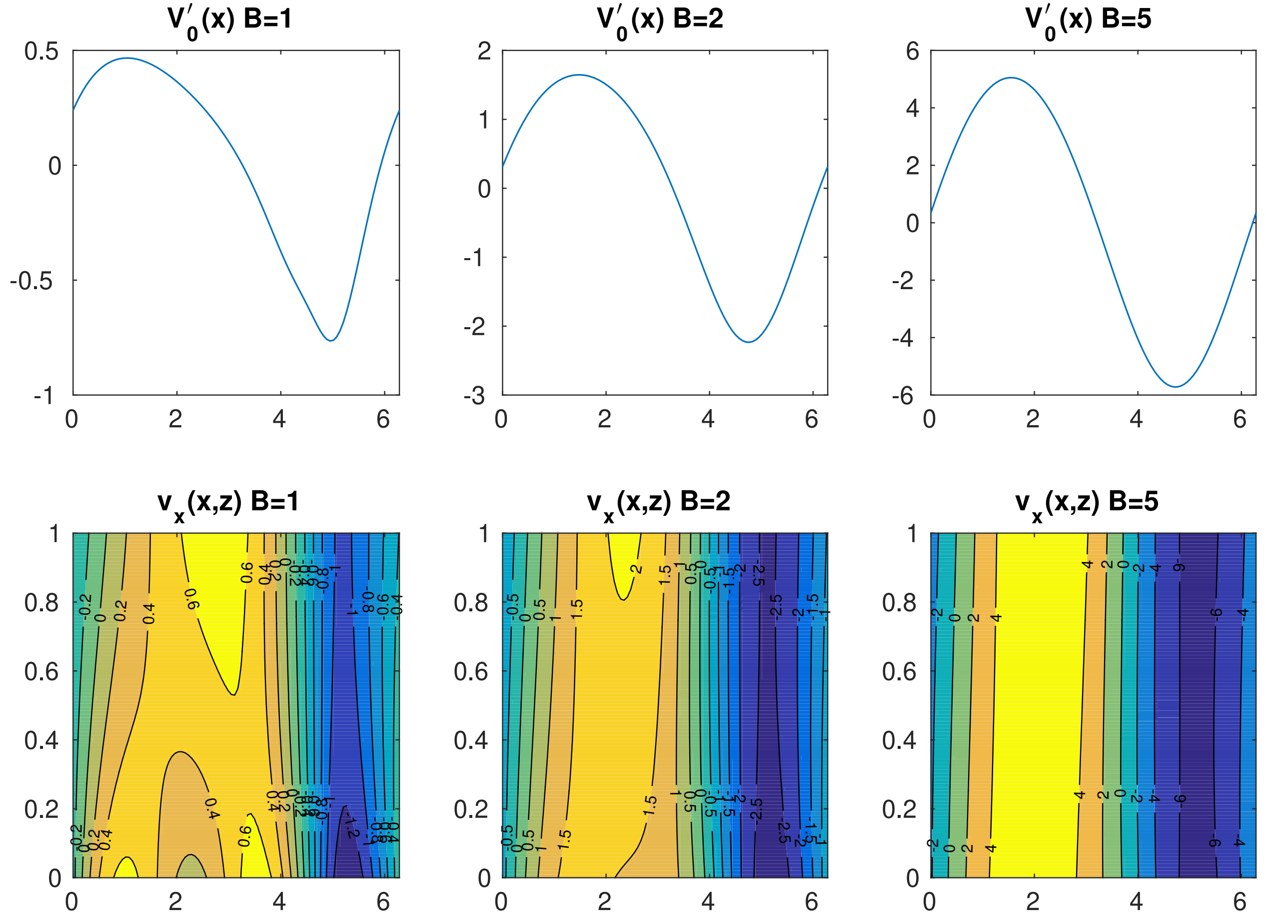

Figure 8.3: The geostrophic flow and contours of $v_x\left(x,z\right)$ for $\mathrm{Rm} \rightarrow 0$ and $\mathrm{Ha} = 100$. The horizontal field increases in strength from left to right: $\mathrm{B_s} = 1, 2, 5$.

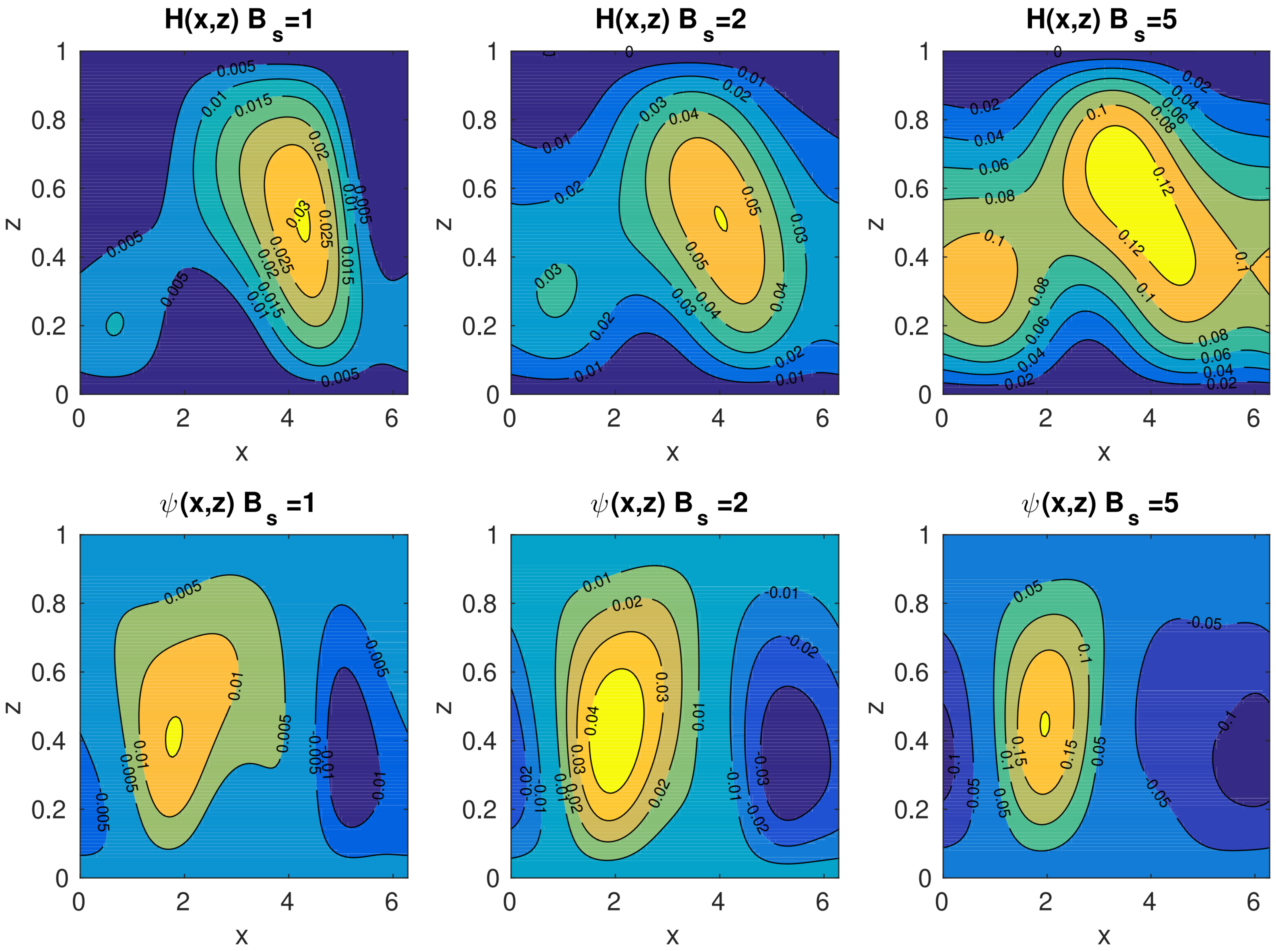

Figure 8.4: Contours of $H\left(x,z\right)$ and $\psi\left(x,z\right)$ for $\mathrm{Rm}\to 0$ and $\mathrm{Ha}=100$. The horizontal field increases in strength from left to right: $\mathrm{B_s}=1,2,5$.

8.1.2 The inviscid large Rm regime

In §5.2.3 (and additionally in §6.2) the energy spectra of the geostrophic flow was calculated for the case in which $\mathrm{B_s} = 0$. It was commented that in the case of $\mathrm{B_s} = 0$ that there was only coupling between the even harmonics in $V_0'(x)$ and that this was a property of the $\mathrm{B_s} = 0$ regime. In figure 8.5, the energy spectra of the geostrophic quantities are plotted for $\mathrm{Rm} = 100$, $\mathrm{Ha}^{-1} \to 0$ and $\mathrm{B_s} = 1$ and, as a result of introducing the horizontal field, all harmonics are now coupled.

The reason for this coupling can be seen in equation (5.30) — the coefficients of $V_0'(x)$ contribute only at the $n-1$ and $n+1$ levels when $\mathrm{B_s} = 0$. For $\mathrm{B_s} \neq 0$, the $\mathrm{B_s}V_0'(x)$ term in (5.23) introduces a contribution at the n-level, resulting in a coupling between odd and even modes for $V_0'(x)$.

The consequence of coupling between all harmonics in the geostrophic flow is that the symmetry observed throughout Chapter 6 will be broken and the resulting solutions to $V_0'(x)$ will have much more varied structure, as will be described and presented in figures 8.6 to 8.8. The energy spectra of all four quantities in figure 8.5 imply that the solution is well resolved.

In figures 8.6–8.8 the contours of $v_x(x,z)$, $H(x,z)$ and $\psi(x,z)$ are plotted together with $V_0'(x)$ for $\mathrm{Rm} = 100$, $\mathrm{Ha}^{-1} \to 0$ and $\mathrm{B_s} = 0.5, 1, 2$. In figure 8.7 we comment on the fact that although the singularity is removed from the geostrophic flow in the inviscid large Rm solution (see §6.1), there are some steep gradients in the geostrophic flow. This can also be seen in the contour plot of $v_x(x,z)$ in figure 8.7. It is not clear what is causing these steep gradients at this particular point in the parameter regime but the resulting structure observed is of interest, however, an analytical theory for this is not possible at large Rm. The contours of $v_x(x,z)$ and $H(x,z)$ show asymmetry throughout figures 8.6–8.8.

The z-boundary layers in the stream function that can be seen at large Rm (see figure 6.5) no longer exist in the horizontal field case. The amplitude of the stream function between the $\mathrm{B_s} = 0$ and $\mathrm{B_s} = 0.5$ solution at $\mathrm{Rm} = 100, \mathrm{Ha}^{-1} \to 0$ has increased by a factor of 10. The effect of increasing Rm results in the compression

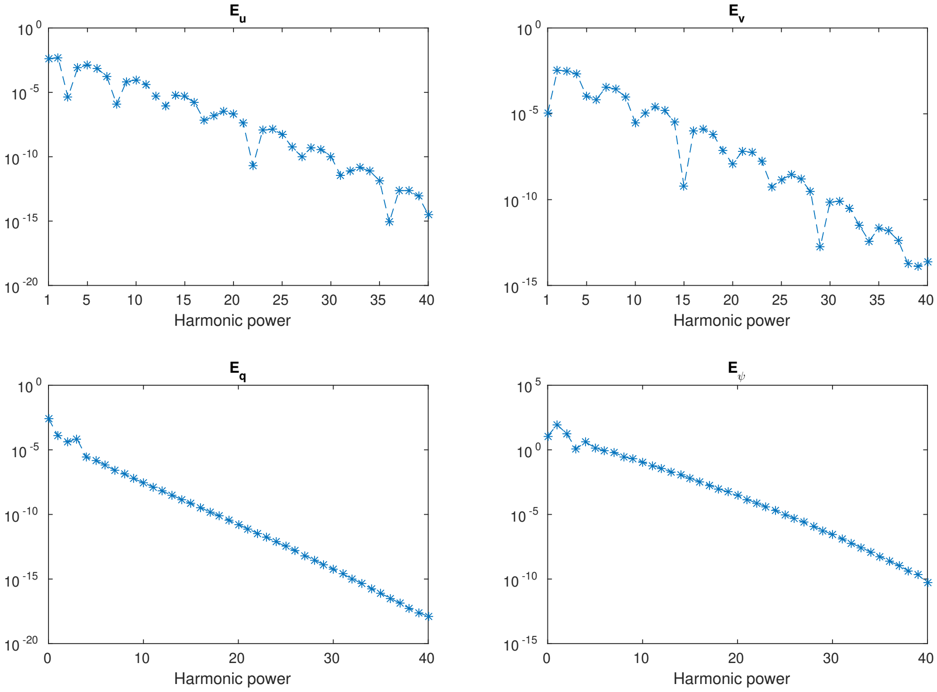

Figure 8.5: Energy spectra of geostrophic quantities at $\mathrm{Rm} = 100$, $\mathrm{Ha} = 100$, $\mathrm{B_s} = 1$ for $k = 1$.

of the z-structure into the lower half of the domain for $\psi(x, z)$ in the $\mathrm{B_s} = 0$ regime, whilst the inclusion of the horizontal field alleviates this compression effect; the z-structure of $\psi(x, z)$ extends beyond the lower half of the domain in figure 8.8 when $\mathrm{B_s} = 2$.

The inclusion of the horizontally imposed field has a strong effect on the amplitude of $v_x(x, z)$, $H(x, z)$ and $\psi(x, z)$ in this regime (cf. figures 8.6 through to figure 8.8 where the amplitude of $v_x(x, z)$ is now of order 1). We expect this trend to continue as $\mathrm{B_s}$ becomes large however this would then change the dynamics of the problem entirely — we would be considering a system in which the horizontal field dominates.

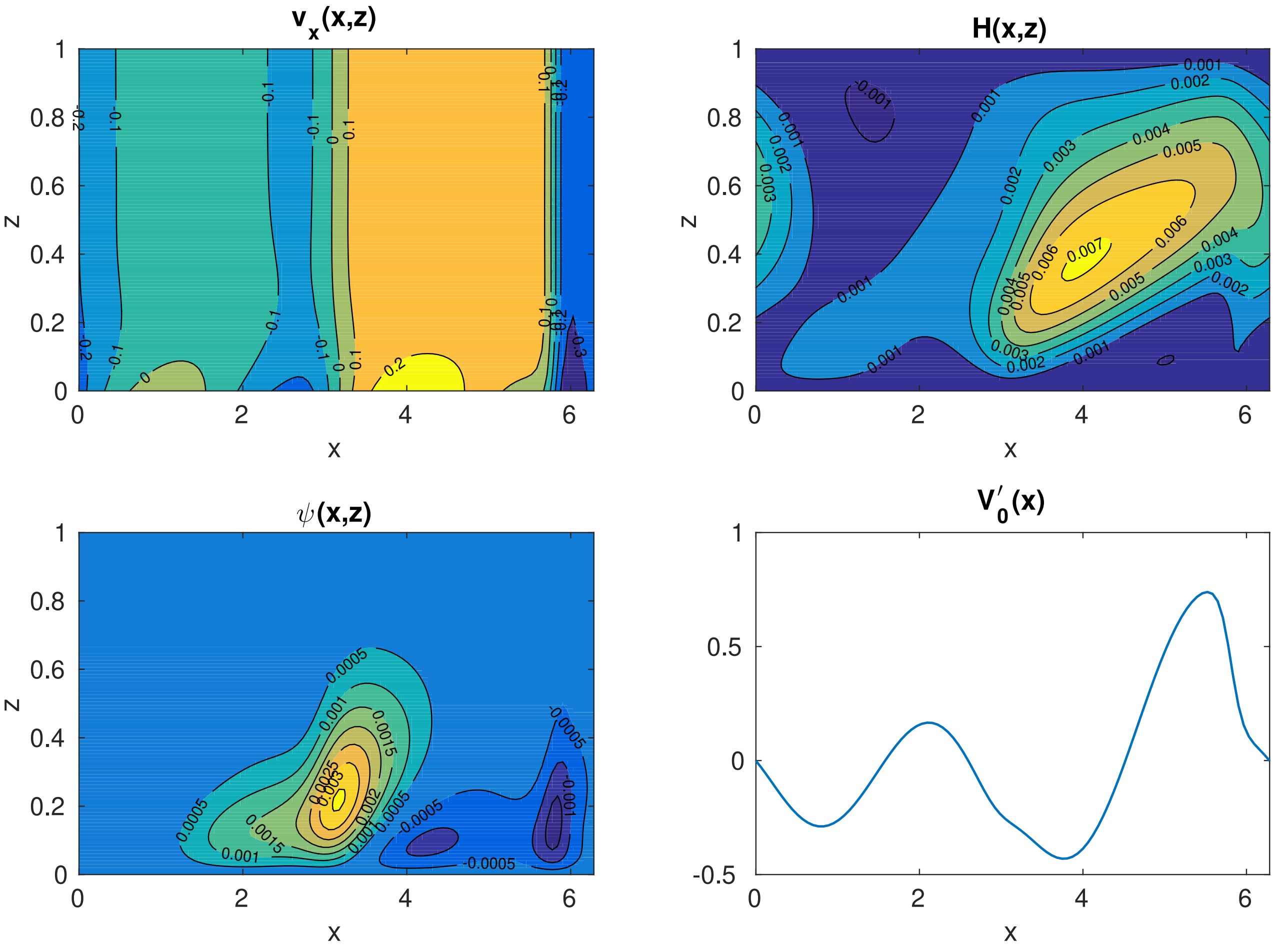

Figure 8.6: The geostrophic flow and the contours of $v_x\left(x,z\right)$, $H\left(x,z\right)$ and $\psi\left(x,z\right)$ for $\mathrm{Ha}^{-1}\rightarrow 0$, $\mathrm{Rm}=100$ and $\mathrm{B_s}=0.5$.

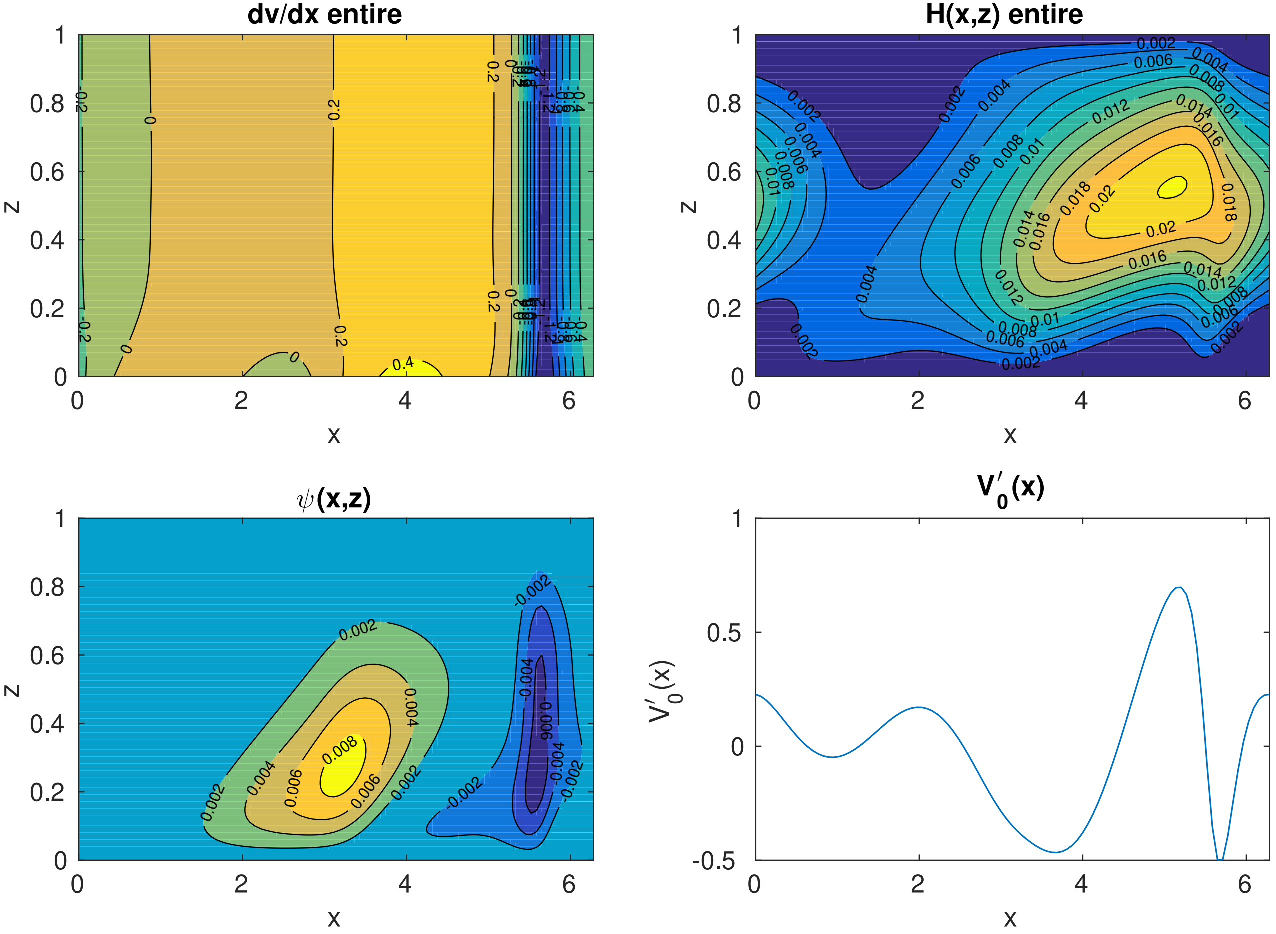

Figure 8.7: The geostrophic flow and the contours of $v_x\,(x,z)$, $H\,(x,z)$ and $\psi\,(x,z)$ for $\mathrm{Ha}^{-1} \to 0$, $\mathrm{Rm} = 100$ and $\mathrm{B_s} = 1$.

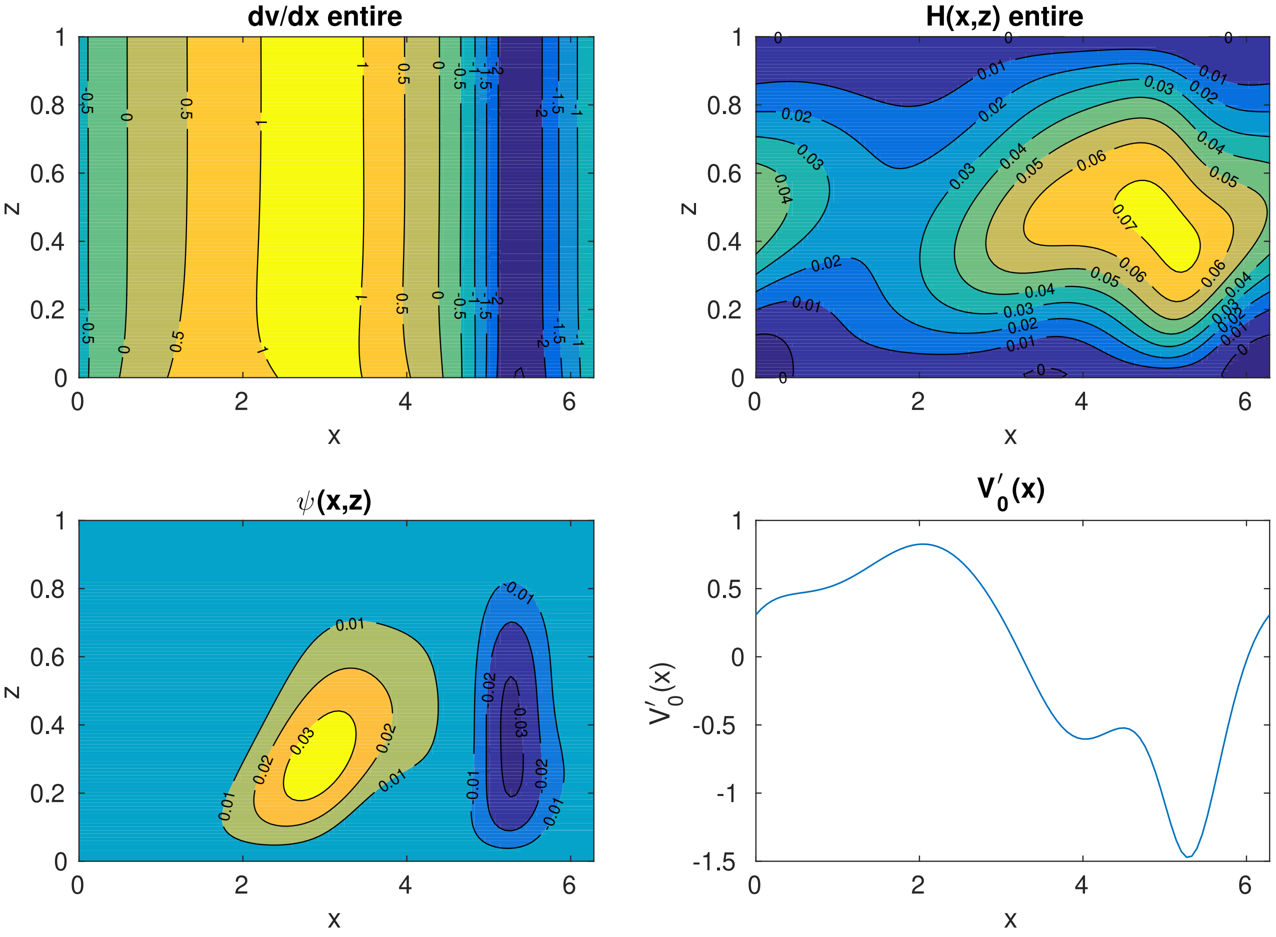

Figure 8.8: The geostrophic flow and the contours of $v_x\,(x,z)$, $H\,(x,z)$ and $\psi\,(x,z)$ for $\mathrm{Ha}^{-1} \to 0$, $\mathrm{Rm} = 100$ and $\mathrm{B_s} = 2$.

8.1.3 Inviscid small $\mathrm{B_s}$ analysis

The form of $V_0'(x)$ shown in figure 8.1 suggests that there is the possibility to expand on the analysis of §7.3 by including the horizontal field term into the boundary layer equations. Below we consider the initial steps to the analysis; however, due to time constraints and the complexity of the governing equations, we have yet to extend beyond what is provided below.

The numerical solutions for small $\mathrm{B_s}$ and large Ha can be used to determine the size of the terms in the system of equations. In figures 8.9–8.11, the terms in equation (5.5) are plotted to highlight which terms are significant in the limit of $\mathrm{Rm} \to 0$, $\mathrm{Ha} \to \infty$ and $\varepsilon \ll \mathrm{B_s} < 1$ and also to highlight their significance in the boundary layer. We can see from figure 8.9 that both the Ha^{-2} term and the $\mathrm{B_s}$ term in (5.5) are of the same magnitude and that both must therefore be included in the analysis.

We consider a viscous fluid as $\mathrm{Rm} \to 0$ and $\varepsilon \ll \mathrm{B_s} < 1$ with an exterior and interior solution for the boundary layer. The solutions to $A(x,z)$ and $v(x,z)$ remain the same between the interior and exterior; however the geostrophic flow will differ between the two. The interior solution for $v(x,z)$ is expressed as

$$v(x,z) = v^a(x,z) + V_b(s), \tag{8.1}$$

where $V_b(s)$ is the geostrophic component that is dependent on the horizontal field inside the boundary layer. The exterior solution to the meridional field is expressed as

$$H(x,z) = H^a(x,z) + H^g(x,z), \tag{8.2}$$

where the solutions to $H^a(x,z)$ and $H^g(x,z)$ are determined from the small Rm inviscid solution (4.26) and (4.41); i.e. they satisfy,

$$\frac{\partial^2 H^a}{\partial x^2} + \frac{\partial^2 H^a}{\partial z^2} = \frac{\partial(v^a, A)}{\partial(x,z)}, \tag{8.3}$$

$$\frac{\partial^2 H^g}{\partial x^2} + \frac{\partial^2 H^g}{\partial z^2} = \tilde{V}_0 k \cot(kx) \frac{\partial A}{\partial z} = -\tilde{V}_0 k^2 e^{-kz} \cos(kx). \tag{8.4}$$

Inside the boundary layer, $\mathrm{B_s}$ is now significant and of the same order as all other terms, so we must include an additional contribution to $H(x,z)$, namely

$$H(x,z) = H^{a}(x,z) + H^{g}(x,z) + \varepsilon^{2} h_{b}(x,z), \tag{8.5}$$

where $H(x,z)$ obeys the equation (cf. equation (7.40)),

$$\frac{\partial^2 H}{\partial x^2} + \frac{\partial^2 H}{\partial z^2} = \frac{\partial(v,A)}{\partial(x,z)} - \mathrm{B_s}\frac{\partial v}{\partial x}. \tag{8.6}$$

Inside the boundary layer we now have a new contribution in equation (8.6) with the additional $\mathrm{B_s}\partial_x v$ term. This additional term means that the boundary layer contribution $h_b(x,z)$ is the solution to the equation

$$\varepsilon^2\left(\frac{\partial^2 h_b}{\partial x^2} + \frac{\partial^2 h_b}{\partial z^2}\right) = -\frac{\mathrm{B_s}}{\varepsilon}\frac{\mathrm{d}V_b}{\mathrm{d}s} + \frac{1}{\varepsilon}\frac{\mathrm{d}V_b}{\mathrm{d}s}\frac{\partial A}{\partial z} + \tilde{V}_0 k^2 e^{-kz}\cos(kx). \tag{8.7}$$

Since derivatives in x scale as $\partial_x \sim \varepsilon^{-1}\partial_s$, equation (8.7) reduces (at leading order) to,

$$\frac{\partial^2 h_b}{\partial s^2} = -\frac{\mathrm{B_s}}{\varepsilon}\frac{\mathrm{d}V_b}{\mathrm{d}s} - \frac{1}{\varepsilon}\frac{\mathrm{d}V_b}{\mathrm{d}s}e^{-kz}\sin(kx) + \tilde{V}_0 k e^{-kz}\cos(kx). \tag{8.8}$$

We may expand about $x = 0$ to express $\sin(kx)$ and $\cos(kx)$ in terms of s and ε,

$$\sin(kx) \approx s\varepsilon k + \mathcal{O}\left(\varepsilon^3\right), \tag{8.9}$$

$$\cos(kx) \approx 1 + \mathcal{O}\left(\varepsilon^2\right). \tag{8.10}$$

Hence (8.8) becomes

$$\frac{\partial^2 h_b}{\partial s^2} = -\frac{\mathrm{B_s}}{\varepsilon}\frac{\mathrm{d}V_b}{\mathrm{d}s} - ke^{-kz}s\frac{\mathrm{d}V_b}{\mathrm{d}s} + \tilde{V}_0 k e^{-kz}. \tag{8.11}$$

In comparison with equation (7.50) there is an additional $\mathrm{B_s}$ term for $h_b(s,z)$. We thus decompose $h_b(s,z)$ into two parts, as

$$h_b(s,z) = ke^{-kz}\hat{h}_1(s) + \hat{h}_2(s), \tag{8.12}$$

where

$$\frac{\mathrm{d}^2\hat{h}_1}{\mathrm{d}s^2} = \tilde{V}_0 - s\frac{\mathrm{d}V_b}{\mathrm{d}s}, \tag{8.13}$$

$$\frac{\mathrm{d}^2\hat{h}_2}{\mathrm{d}s^2} = -\frac{\mathrm{B_s}}{\varepsilon}\frac{\mathrm{d}V_b}{\mathrm{d}s}. \tag{8.14}$$

The stream function inside the boundary layer satisfies the equation,

$$\frac{\partial\psi}{\partial z} = \frac{\partial(H,A)}{\partial(x,z)} - \mathrm{B_s}\frac{\partial H}{\partial x} - \frac{1}{\mathrm{Ha}^2}\nabla^2 v, \tag{8.15}$$

and substitution of (8.5) into (8.15) gives

$$\begin{aligned}\frac{\partial \psi}{\partial z} =& \frac{\partial \left(H^a, A\right)}{\partial \left(x, z\right)} + \frac{\partial \left(H^g, A\right)}{\partial \left(x, z\right)} - \varepsilon \frac{\partial h_b}{\partial s} e^{-kz} \sin\left(kx\right) \\ & - \varepsilon^2 \frac{\partial h_b}{\partial z} e^{-kz} \cos\left(kx\right) - \mathrm{B_s} \varepsilon \frac{\partial h_b}{\partial s} - \mathrm{B_s} \frac{\partial H^a}{\partial x} - \mathrm{B_s} \frac{\partial H^g}{\partial x} - \frac{1}{\varepsilon^2 \mathrm{Ha}^2} \frac{\mathrm{d}^2 V_b}{\mathrm{d}s^2}. \end{aligned} \tag{8.16}$$

The leading order solution of (8.16) at $\mathcal{O}\left(1\right)$ yields Taylor's constraint, namely

$$\int_0^1 \frac{\partial \left(H^a, A\right)}{\partial \left(x, z\right)} + \frac{\partial \left(H^g, A\right)}{\partial \left(x, z\right)} \mathrm{d}z = \text{constant}. \tag{8.17}$$

On expanding the remaining terms in (8.16) using (8.12), integrating over the domain then gives

$$\begin{aligned} 0 =& -\varepsilon^2 k^2 s \frac{\mathrm{d}\hat{h}_1}{\mathrm{d}s} \int_0^1 e^{-2kz} \mathrm{d}z - \varepsilon^2 k \frac{\mathrm{d}\hat{h}_2}{\mathrm{d}s} \int_0^1 e^{-kz} \mathrm{d}z \\ & + \varepsilon^2 k^2 \hat{h}_1\left(s\right) \int_0^1 e^{-2kz} \mathrm{d}z - \mathrm{B_s} \varepsilon k \frac{\mathrm{d}\hat{h}_1}{\mathrm{d}s} \int_0^1 e^{-kz} \mathrm{d}z - \mathrm{B_s} \varepsilon \frac{\mathrm{d}\hat{h}_2}{\mathrm{d}s} \\ & + \mathrm{B_s} k \varepsilon s \int_0^1 h_g\left(z\right) + h_a\left(z\right) \mathrm{d}z - \frac{1}{\varepsilon^2 \mathrm{Ha}^2} \frac{\mathrm{d}^2 V_b}{\mathrm{d}s^2}. \end{aligned} \tag{8.18}$$

It is clear from both (8.18) and (8.14) that in order for all terms in equation (8.18) to be $\mathcal{O}\left(\varepsilon^2\right)$, we must choose the magnitude of $\mathrm{B_s}$ to be $\mathrm{B_s} \sim \mathcal{O}\left(\varepsilon\right)$. The Hartmann number scaling in this problem is therefore the same as in §7, i.e. $\mathrm{Ha} \sim \varepsilon^{-2}$. We note that $h_a\left(z\right)$ and $h_g\left(z\right)$ are the solutions to (4.24) and (4.40) and take the form

$$h_g\left(z\right) = \frac{\widetilde{\mathrm{V}}_0}{2} \left[z e^{-kz} - \frac{\sinh\left(kz\right) e^{-k}}{\sinh\left(k\right)} \right], \tag{8.19}$$

$$h_a\left(z\right) = \alpha_0 \sinh\left(kz\right) + \alpha_1 \cosh\left(kz\right) + \frac{1}{8k} \left(z - \frac{1}{4k} \right) e^{-3kz}. \tag{8.20}$$

An exact choice of ε (cf. the choice (7.75) made in §7.4) would reduce equation (8.18) into our final boundary layer ODE. The reduced ODE form of (8.18) along with equations (8.13) and (8.14) would be solved together to give $V_b'\left(s\right)$. The difficulty remains in determining the choice of ε such that (8.18) reduces to an ODE; although (8.18) is a coupled ODE in s we have yet to find a way to reduce this into a simple form. The z-boundary layer correction terms may again need to be included in our analysis and further consideration will be needed for future work.

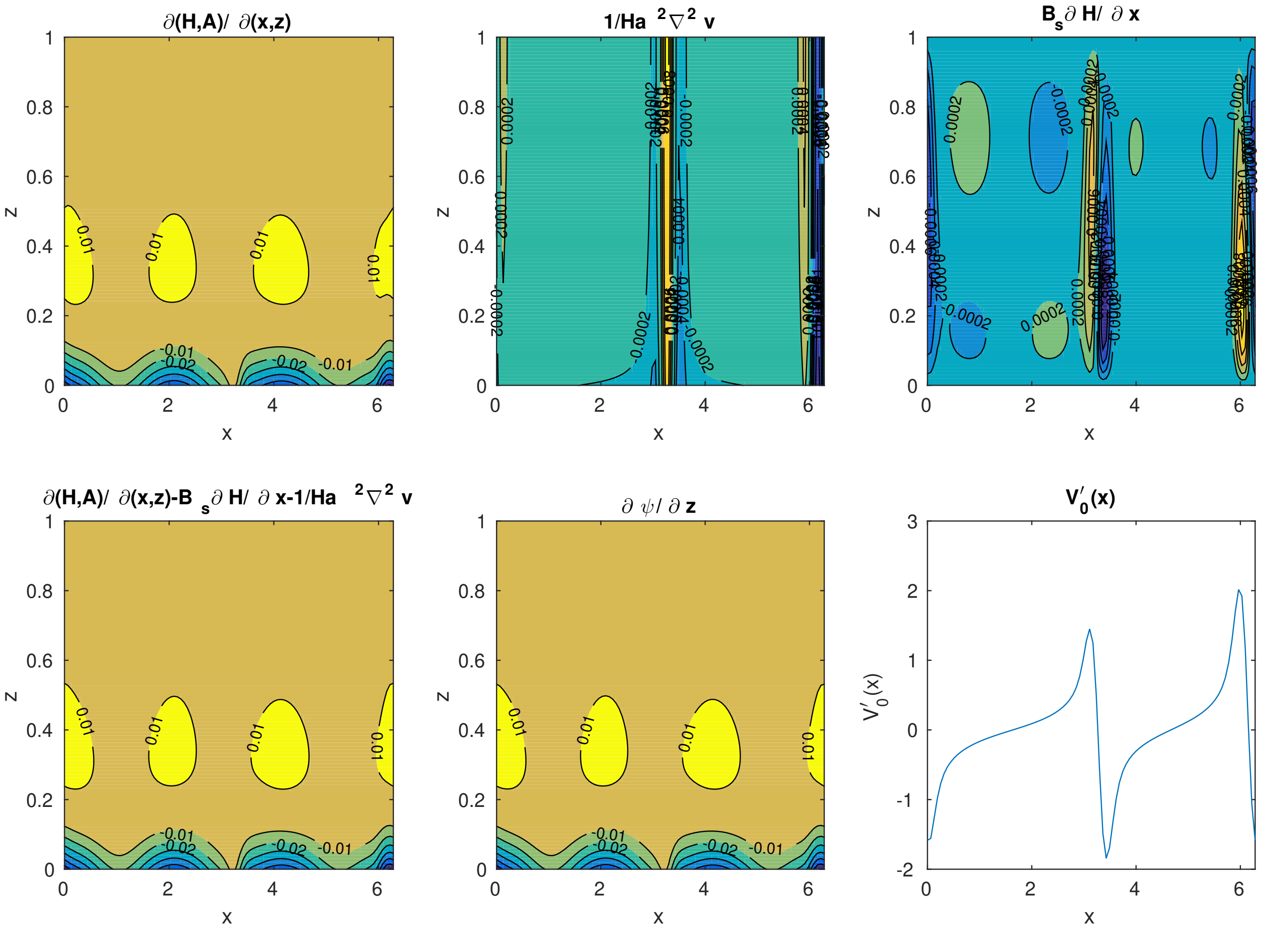

Figure 8.9: Comparison of terms in (5.5) at Ha = 100, Rm → 0 and $\mathrm{B_s} = 0.1$. The top row compares individual terms and the bottom row compares the right and left hand sides of (5.5) respectively and the geostrophic flow.

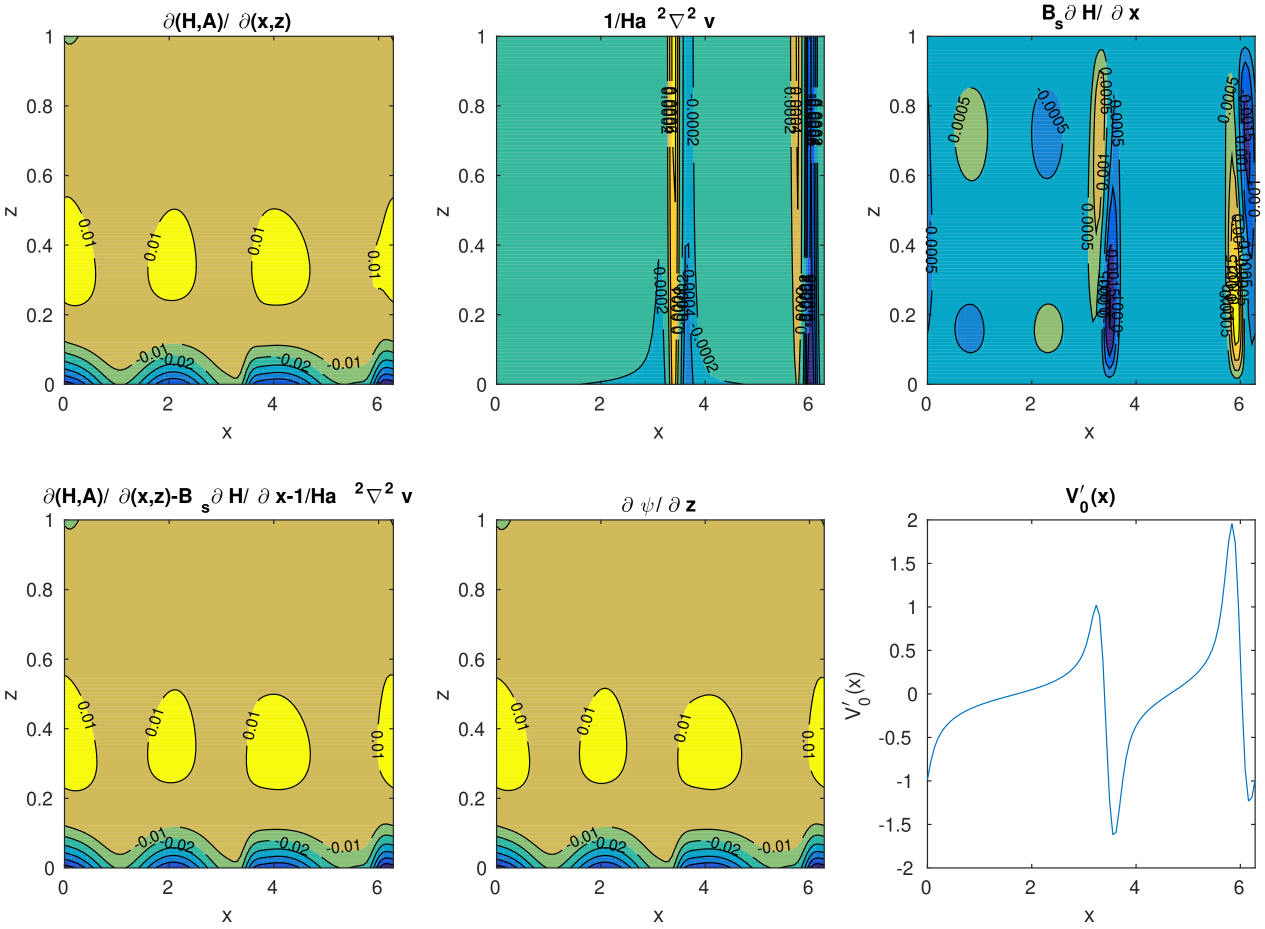

Figure 8.10: Comparison of terms in (5.5) at Ha = 100, Rm → 0 and $B_s = 0.2$. The top row compares individual terms and the bottom row compares the right and left hand sides of (5.5) respectively and the geostrophic flow.

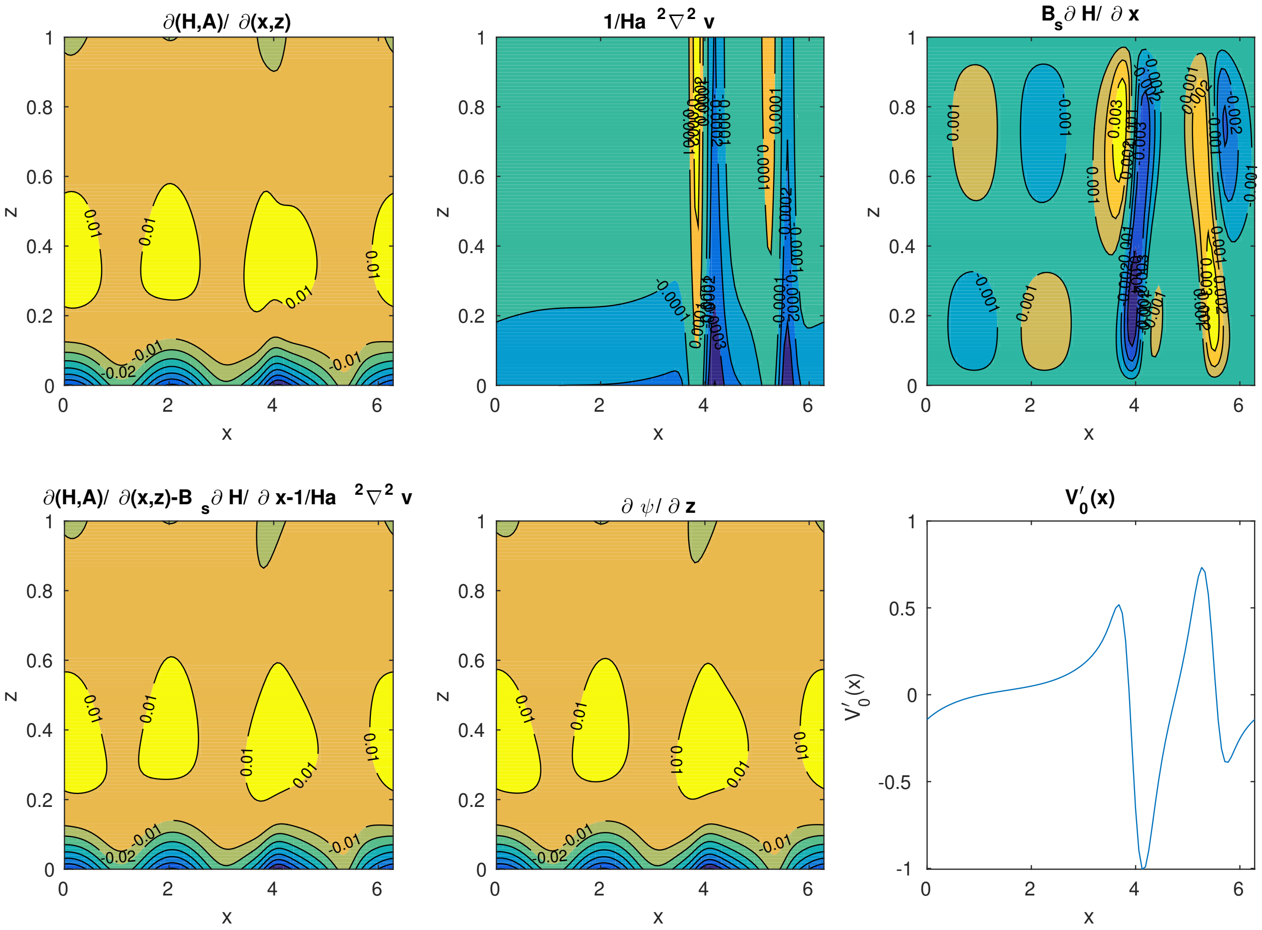

Figure 8.11: Comparison of terms in (5.5) at Ha = 100, Rm → 0 and $B_s = 0.5$. The top row compares individual terms and the bottom row compares the right and left hand sides of (5.5) respectively and the geostrophic flow.

Chapter 9

Conclusions and future work

9.1 Summary and conclusions

Since the first measurements of Saturn's magnetic field and atmospheric composition there has been a lot of active research across many disciplines to explain its spin-axisymmetry and lack of helium in the upper atmosphere. Many different pieces of evidence point towards the formation of a stably stratified layer deep within the interior that may explain the axisymmetric structure and, at the same time, explain the lack of helium in the upper atmosphere. This evidence was discussed in §1.2 and there is still some debate regarding the size and depth of the stable layer. Many models confirm that a stable layer is required in order to have an axisymmetric magnetic field (Christensen & Wicht, 2008). The physical mechanisms that could be driving the shear in the Stevenson model are also considered; convection within the upper atmosphere redistributes heat and generates a pole-equator temperature gradient above the stratified layer.

The original motivation for this work was to expand on the Stevenson model for the stratified layer by including a depth dependent conductivity profile in the kinematic regime and by investigating the consequences of Taylor's constraint in the dynamic regime. The presence of a stable layer under the influence of a shear is important for the attenuation of the non-axisymmetric magnetic field. Although higher order effects such as variable conductivity have a small effect on the attenuation of the poloidal field in the linear regime these higher order effects may become important in the nonlinear case. In Chapter 2 we expanded on the kinematic model and found that the poloidal field is somewhat independent of the choice of conductivity profile, whilst the toroidal field is strongly linked to both the conductivity profile and the shear profile in the layer.

In the dynamic regime we found that a new flow arises due to the Lorentz forces induced by the magnetic field. In our two-dimensional model, where the field and flow are independent of the y-direction (corresponding to the meridional direction in a spherical geometry), we showed that the y-component of the flow could be divided into an ageostrophic z-dependent part and a geostrophic z-independent part. The ageostrophic component could be determined directly from the y-component of the vorticity equation (magnetic wind equation), but the geostrophic component has to be determined using a modified form of Taylor's constraint. We have applied Taylor's constraint to determine the geostrophic part of the meridional flow, and completed the solution by finding the stream function in the x-z plane. We note the similarity between the axisymmetric solution found in Soward & Jones (1983), discussed in Chapter 3, and our non-axisymmetric model. The difference between them is that in our model the geostrophic flow is in the meridional direction, which is contrary to the azimuthal direction typically found in standard Taylor constraint problems.

Although we did not consider solutions to Taylor's constraint for Elsasser number of order unity there has been progress in the regime of $\Lambda \ll 1$. In Chapter 4 the analytical solution found in the small Rm limit allowed for verification of the numerical solution to the system of equations at the corresponding parameter values. The geostrophic flow was found to be discontinuous in the small Rm, inviscid limit; the reason for this was that the magnetic field vanishes at $x = n\pi$ (where n is an integer) for all z in the $\mathrm{Rm} \to 0$ limit, and as a consequence, infinite magnetic stretching was required to generate the meridional field. We also showed that the solution has additional symmetries in the cases when $\mathrm{B_s} = 0$ (no imposed horizontal field) and $\mathrm{Rm} \to 0$. The solutions to the generated meridional field $H\left(x, z\right)$ and the stream function were also found.

In Chapter 5 we tested two different numerical codes; one was adapted to deal with the singular behaviour in the limit of an inviscid fluid as Rm → 0, whilst the other dealt with the general set of equations for moderate Rm-Ha-$\mathrm{B_s}$. Although the theory does not have an explicit boundary condition to evaluate the ageostrophic part of $v\left(x,z\right)$, we discuss the need for such a boundary condition in the numerical code and how different choices do not affect the overall solution. This was done by comparing two different boundary conditions for the ageostrophic component of $v\left(x,z\right)$. The symmetries observed in the theory in Chapter 4 were also confirmed in the numerics and further symmetries were noted in the absence of the horizontal field.

In Chapter 2, the solution to the potential field, $A\left(x,z\right)$, within the layer was calculated for moderate Rm and expressed in terms of the Hankel function. The difficulty in progressing with this solution to evaluate $J_y\left(x,z\right)$, $v\left(x,z\right)$ etc. meant that an analytical theory for moderate Rm was deemed intractable. As a consequence, we developed numerical solutions for moderate Rm in Chapter 6 and found, to our surprise, that the singular behaviour in the geostrophic flow vanishes as Rm becomes large. The reason for this was due to the shear flow bending the field lines, resulting in at least some non-zero field over the domain in z at the original singularity points $x = n\pi$. The non-axisymmetric magnetic field, as predicted by Stevenson, is indeed attenuated towards the top of the stable layer. This axisymmetrizing effect is shown in both the kinematic and dynamical models, with Rm the key parameter to this effect. However, the non-axisymmetric geostrophic meridional flow generated from the non-axisymmetric field is not attenuated at the top of the stable layer, a result that would not have been expected from the kinematic theory.

Chapter 6 also explored solutions for a viscous fluid and it was found that viscosity removes the singularity as Rm → 0. As solutions for Rm → 0 are relatively simple to evaluate for the inviscid fluid, the inclusion of viscosity meant that there were possible grounds to extend the analysis of Chapter 4 and develop an asymptotic theory for the viscous case. The flow speeds calculated in our model are within the correct order of magnitude when compared with estimates for the internal velocities of Saturn; this shows that our model can produce credible solutions that are reasonable to compare with the dynamics of Saturn. The expansion of the Stevenson model to include the nonlinear effects showed that the main mechanism behind the field attention still holds compared to the kinematic regime for similar values of Rm. Whilst the flow speeds in Chapter 6 would suggest that Rm ~ 400 inside Saturn's stable layer.

The viscous asymptotic theory was developed in Chapter 7 and solutions to the system of equations were found in the case of small Hartmann number Ha, i.e. when viscosity is dominant in the system. In the small Ha limit the leading order solution to the geostrophic flow is zero but the next order solution gives a well-behaved solution for $V_0'(x)$. The explanation for the transition from the well-behaved viscous solution to the singular inviscid solution can be seen in the numerical results of Chapter 6 where a boundary layer structure near $x = n\pi$ is seen in the geostrophic flow. A boundary layer solution for the geostrophic flow was derived in Chapter 7 by considering an inner and outer solution for $V_0'(x)$. The theory suggested that there were also additional z-boundary layers within the x-boundary layer; this was supported by the numerical results. Despite these complications, the leading order asymptotic problem could be solved analytically in terms of modified Struve and Bessel functions, whose properties are documented. This enabled us to establish numerical agreement between our asymptotic boundary layer analysis and the full numerical code. While the leading order asymptotic problem was amenable to exact solution, the higher order $\mathcal{O}(\varepsilon^3)$ terms could not be solved analytically.

Chapter 8 considered the numerical solutions in the presence of a horizontal field of strength $\mathrm{B_s}$. A uniform field in the x-direction corresponds to an axisymmetric toroidal field in Saturn. We know that Saturn has a strong axisymmetric meridional field and that if a dynamo is producing a meridional field then it is likely also to produce an axisymmetric toroidal field component. However, the main motivation for inclusion of the horizontal field was to see if it removed the singular behaviour as Rm $\to 0$. We found this to be the case providing $\mathrm{B_s}$ was sufficiently large; there were two significant cases to consider for the magnitude of $\mathrm{B_s}$ for small ε: $\varepsilon \leq \mathrm{B_s} < 1$

and $\mathrm{B_s} \geq 1$. In the case of $\mathrm{B_s} \geq 1$, the inclusion of the horizontal field resulted in the removal of the singular behaviour in $V_0'(x)$, which was expected. The horizontal field also removed the boundary layer formation in the stream function for large Rm. Progressively larger $\mathrm{B_s}$ resulted in the magnitude of the geostrophic flow being large and, consequently, the meridional flow becoming almost entirely geostrophic. In the case $\varepsilon \leq \mathrm{B_s} \ll 1$, we found that the singularity in $V_0'(x)$ is not removed as we first expected but is instead shifted in x; there is also an asymmetric structure to the geostrophic flow. This salient feature of asymmetry arises when introducing the horizontal field and is prevalent also in both the stream function and meridional field.

The reason for this asymmetry was explained in Chapter 5 in terms of the coupling of the harmonics in the governing equations. The energy spectra of the geostrophic quantities further validated the asymmetric behaviour when compared with the energy spectra of the $\mathrm{B_s} = 0$ solution. We considered the initial steps to an analytical theory to explain this asymmetry in the geostrophic flow for the case $\varepsilon \leq \mathrm{B_s} \ll 1$ by reconsidering the boundary layer equations from Chapter 7. Some initial progress has been made in formulating the required equations; however, the task of determining the exact form for small ε has proven difficult and we leave the equations as they are for future work.

9.2 Future work

There are plenty of opportunities for future work with this model both from a numerical and an analytical perspective. The next logical step in our model would be to tackle the moderate Elsasser number equations; this problem would most likely have some interesting dynamics. The numerical method developed in Chapter 5 could be extended to the moderate Elsasser number case. However, whereas in the small Λ case, equations (3.26)–(3.30) could be solved sequentially, when Λ is $\mathcal{O}(1)$ all the equations have to be solved simultaneously. This would slow down the code, but since the problem is two-dimensional it would be feasible on a large computer.

A more physical extension to our model would be to include a more realistic conductivity profile within the stable layer. This was sampled in our kinematic model of the plane layer, but was not considered in our main dynamical model. However, such models have been considered in spherical geometry (Dietrich & Jones, 2018), and it would be of interest to compare the solutions of a localised Cartesian model with a global spherical solution and to compare with the flow speed estimates provided from the numerics in Chapter 6. These flow speed estimates suggest that the model is working reasonably well at estimating the flow speeds within the stable layer, so this would also be an interesting point to compare with depth-dependent conductivity profiles.

Beyond the domain of Cartesian geometry, a solution in spherical geometry would give deeper insight into the dynamics of the problem; effects such as curvature and viscosity may have a significant role in the structure of the geostrophic flow. These considerations would be reasonable to pursue in the quest to extend further our knowledge of the dynamics of Saturn and its axisymmetric magnetic field.

Bibliography

Abdel-Aziz, M. & Jones, C. (1988). $\alpha\omega$-dynamos and Taylor's constraint. *Geophysical & Astrophysical Fluid Dynamics*, **44**, 117–139.

Abramowitz, M. & Stegun, I.A. (1964). *Handbook of mathematical functions: with formulas, graphs, and mathematical tables*, vol. 55. Courier Corporation.

Aubert, J. (2005). Steady zonal flows in spherical shell dynamos. *Journal of Fluid Mechanics*, **542**, 53–67.

Ben-Jaffel, L. & Abbes, I. (2015). Helium abundance in giant planets and the local interstellar medium. In *Journal of Physics: Conference Series*, vol. 577, 012003, IOP Publishing.

Burke, B. & Franklin, K. (1955). Observations of a variable radio source associated with the planet Jupiter. *Journal of Geophysical Research*, **60**, 213–217.

Childress, S. (1969). A class of solutions of the magnetohydrodynamic dynamo problem. *The Application of Modern Physics to the Earth and Planetary Interiors*, 629–648.

Christensen, U.R. & Wicht, J. (2008). Models of magnetic field generation in partly stable planetary cores: Applications to Mercury and Saturn. *Icarus*, **196**, 16–34.

Connerney, J. (1993). Magnetic fields of the outer planets. *Journal of Geophysical Research: Planets*, **98**, 18659–18679.

Cowling, T.G. (1933). The magnetic field of sunspots. *Monthly Notices of the Royal Astronomical Society*, **94**, 39–48.

Dietrich, W. & Jones, C. (2018). Anelastic spherical dynamos with radially variable electrical conductivity. *Icarus*, **305**, 15–32.

Duarte, L.D., Gastine, T. & Wicht, J. (2013). Anelastic dynamo models with variable electrical conductivity: An application to gas giants. *Physics of the Earth and Planetary Interiors*, **222**, 22–34.

Fortney, J.J. & Hubbard, W.B. (2003). Phase separation in giant planets: inhomogeneous evolution of Saturn. *Icarus*, **164**, 228–243.

French, M., Becker, A., Lorenzen, W., Nettelmann, N., Bethkenhagen, M., Wicht, J. & Redmer, R. (2012). Ab initio simulations for material properties along the Jupiter adiabat. *The Astrophysical Journal Supplement Series*, **202**, 5.

Fuller, J. (2014). Saturn ring seismology: Evidence for stable stratification in the deep interior of Saturn. *Icarus*, **242**, 283–296.

Fuller, J., Lai, D. & Storch, N.I. (2014). Non-radial oscillations in rotating giant planets with solid cores: Application to Saturn and its rings. *Icarus*, **231**, 34–50.

Guillot, T. (1999). Interiors of giant planets inside and outside the solar system. *Science*, **286**, 72–77.

Hale, G.E. (1908). On the probable existence of a magnetic field in sun-spots. *The Astrophysical Journal*, **28**, 315.

Hanel, R., Conrath, B., Kunde, V., Pearl, J. & Pirraglia, J. (1983). Albedo, internal heat flux, and energy balance of Saturn. *Icarus*, **53**, 262–285.

Hedman, M. & Nicholson, P. (2013). Kronoseismology: using density waves in Saturn's C ring to probe the planet's interior. *The Astronomical Journal*, **146**, 12.

Hollerbach, R. (1996). On the theory of the geodynamo. *Physics of the Earth and Planetary interiors*, **98**, 163–185.

Hubbard, W. (1980). Intrinsic luminosities of the Jovian planets. *Reviews of Geophysics*, **18**, 1–9.

Hubbard, W., Guillot, T., Marley, M., Burrows, A., Lunine, J. & Saumon, D. (1999). Comparative evolution of Jupiter and Saturn. *Planetary and Space Science*, **47**, 1175–1182.

Jeffreys, H. (1923). The constitution of the four outer planets. *Monthly Notices of the Royal Astronomical Society*, **83**, 350–350.

Jonathan, A., Heimpel, M., Allen, L., King, E. & Wicht, J. (2008). Convective heat transfer and the pattern of thermal emission on the gas giants. *Geophysical Journal International*, **173**, 793–801.

Jones, C. (2003). Dynamos in planets. *Stellar Astrophysical Fluid Dynamics*, **1**, 159–176.

Jones, C.A. (2008). Course 2 dynamo theory. In *Les Houches*, vol. 88, 45–135, Elsevier.

Jones, C.A. (2011). Planetary magnetic fields and fluid dynamos. *Annual Review of Fluid Mechanics*, **43**, 583–614.

Larmor, J. (1919). How could a rotating body such as the Sun become a magnet?, br. *British Assosciation for the Advancement of Science*, 159–160.

Liu, J., Goldreich, P.M. & Stevenson, D.J. (2008). Constraints on deep-seated zonal winds inside Jupiter and Saturn. *Icarus*, **196**, 653–664.

Low, F.J. (1966). Observations of Venus, Jupiter, and Saturn at lambda20 mu. *The Astronomical Journal*, **71**, 391.

Malkus, W. & Proctor, M. (1975). The macrodynamics of α-effect dynamos in rotating fluids. *Journal of Fluid Mechanics*, **67**, 417–443.

Marley, M.S. & Porco, C.C. (1993). Planetary acoustic mode seismology: Saturn's rings. *Icarus*, **106**, 508–524.

Moffatt, H.K. (1978). Field generation in electrically conducting fluids. *Cambridge, England, Cambridge University Press, 1978. 353 p*, **2**, 1–353.

Ockendon, J.R. (2003). *Applied partial differential equations*. Oxford University Press.

Pollack, J.B., Grossman, A.S., Moore, R. & Graboske, H.C. (1977). A calculation of Saturn's gravitational contraction history. *Icarus*, **30**, 111–128.

Ridley, V.A. & Holme, R. (2016). Modeling the Jovian magnetic field and its secular variation using all available magnetic field observations. *Journal of Geophysical Research: Planets*, **121**, 309–337.

Rosen, P.A., Tyler, G.L. & Marouf, E.A. (1991a). Resonance structures in Saturn's rings probed by radio occultation: I. Methods and examples. *Icarus*, **93**, 3–24.

Rosen, P.A., Tyler, G.L., Marouf, E.A. & Lissauer, J.J. (1991b). Resonance structures in Saturn's rings probed by radio occultation: II. Results and interpretation. *Icarus*, **93**, 25–44.

Salpeter, E. (1973). On convection and gravitational layering in Jupiter and in stars of low mass. *The Astrophysical Journal*, **181**, L83.

Shu, F.H. (1984). Waves in planetary rings. In *IAU Colloq. 75: Planetary Rings*, 513–561.

Smoluchowski, R. (1967). Internal structure and energy emission of Jupiter. *Nature*, **215**, 691.

Soward, A. & Jones, C. (1983). α^2-dynamos and Taylor's constraint. *Geophysical & Astrophysical Fluid Dynamics*, **27**, 87–122.

Stanley, S. (2010). A dynamo model for axisymmetrizing Saturn's magnetic field. *Geophysical Research Letters*, **37**, L05201.

Stevenson, D. (1980). Saturn's luminosity and magnetism. *Science*, **208**, 746–748.

STEVENSON, D. (1982a). Interiors of the giant planets. *Annual Review of Earth and Planetary Sciences*, **10**, 257–295.

STEVENSON, D. (1982b). Reducing the non-axisymmetry of a planetary dynamo and an application to Saturn. *Geophysical & Astrophysical Fluid Dynamics*, **21**, 113–127.

STEVENSON, D. & SALPETER, E. (1977). The dynamics and helium distribution in hydrogen-helium fluid planets. *The Astrophysical Journal Supplement Series*, **35**, 239–261.

STEVENSON, D.J. (2003). Planetary magnetic fields. *Earth and Planetary Science Letters*, **208**, 1–11.

STIXRUDE, L. & JEANLOZ, R. (2008). Fluid helium at conditions of giant planetary interiors. *Proceedings of the National Academy of Sciences*, **105**, 11071–11075.

TAYLOR, J. (1963). The magneto-hydrodynamics of a rotating fluid and the Earth's dynamo problem. *Proceedings of the Royal Society of London A: Mathematical, Physical and Engineering Sciences*, **274**, 274–283.

ZELDOVICH, Y.B. (1957). The magnetic field in the two-dimensional motion of a conducting turbulent fluid. *Sov. Phys. JETP*, **4**, 460–462.

ZHANG, K.K. & BUSSE, F. (1988). Finite amplitude convection and magnetic field generation in a rotating spherical shell. *Geophysical & Astrophysical Fluid Dynamics*, **44**, 33–53.

ZHANG, K.K. & BUSSE, F. (1989). Convection driven magnetohydrodynamic dynamos in rotating spherical shells. *Geophysical & Astrophysical Fluid Dynamics*, **49**, 97–116.